The Applications of Microcavity Lasers in Multimodality Imaging

by

Xuzhou Li

A dissertation submitted in partial fulfillment
of the requirements for the degree of
Doctor of Philosophy
(Mechanical Engineering)
in the University of Michigan
2021

Doctoral Committee:

Professor Xudong Fan, Co-Chair
Professor Xueding Wang, Co-Chair
Professor Katsuo Kurabayashi
Associate Professor Xiaogan Liang

Xuzhou Li

xuzhou@umich.edu

ORCID iD: 0000-0002-5357-8864

Dedication

To my parents, Mingxing Li and Jingxiong Niu, without your support and accompany, I cannot overcome the challenges during the adventure of my Ph.D. A warm family is always the best school. Many good habits I got in childhood are still in effect to facilitate my daily study and work. In the past 27 years, you sacrificed your personal lives and hobbies to ensure I had the best growth environment and education. Thank you for bringing me to this world and keeping devoting everything you have to my growth and success. Even though we are now separated at the two ends of the earth, we will finally reunion soon.

To my wife, Jiaqi Zhang, meeting you at the library of the University of Michigan is the most romantic thing that happened in my life. I believed I found my destiny at the very moment I saw you. During the pandemic, we built the family and supported each other through the most isolated time. Thank you for coming into my life and let's start new adventures together.

To my friends, it is my great pleasure to meet you all during the past 5 years. I truly enjoyed the trips, the parties, sports events, and dinners we had together. If anyone asks me what you miss most about Ann Arbor, I will say the people there. Thank you, my dear friends, for making my Ph.D. life colorful and enjoyable.

Acknowledgments

First of all, I would like to express my sincerest gratitude to my research advisors and committee co-chairs Professor Xueding Wang and Professor Xudong Fan for their guidance and support through my Ph.D. study. They have been my role models with wisdom, persistence, and positive work attitudes to face any challenges in the journey towards Ph.D. Their training and encouragement will be a life-long treasure of mine.

I am also super grateful to Professor Katsuo Kurabayashi and Professor Xiaogan Liang for serving on my dissertation committee and providing insightful comments and suggestions for my proposal and final dissertation defense. Their guidance and suggestions have helped me not only in completing my Ph.D. researches but also in my future career.

Finally, I would like to thank my colleagues in Optic Imaging Lab and Fanlab (Especially, Dr.Wei Zhang, Dr.Yu Qin, Ms. Yanxiu Li, Dr. Yu-cheng Chen, Dr. Xiaotian Tan, Dr. Qiushu Chen, Dr. Xiaoqin Wu, Dr.Hongbo Zhu, Dr. Menglian Zhou, Mr. Maxwell Li, Mr.Mingyang Wang, Ms. Linyu Ni). It is such a pleasure to work with them. Without their support, I can't finish my Ph.D. study in this time frame.

I would also like to acknowledge the University of Michigan (Department of Mechanical Engineering, Department of Biomedical Engineering and Rackham Graduate School), National Science Foundation, and National Institute of Health for providing financial support during my graduate studies.

Table of Contents

List of Figures

List of Equations

Abstract

Multimodality imaging technologies have attracted wide attention in both biological researches and clinical practice. However, the low image signal-to-noise ratio (SNR) and the limited capability to label multiple targets are the major challenges to use multimodality imaging in many *in vivo* biomedical applications. Due to the homogeneity of current optical imaging contrast agents (such as gold and polymer nanoparticles, and fluorophores), only the overall distribution of the targets can be observed. Precise tracking of the trajectory of each individual target is not possible. Microcavity lasers are emerging technologies that have broad applications in biomedical fields. Owing to the high emission intensity, rich spectral information, and narrow linewidth, microcavity lasers may provide a route to achieve deep tissue imaging with a high SNR and track implanted cells with unique identifiers.

In this dissertation, I introduce the development of three applications of microcavity lasers in multimodality imaging: ultrasound modulated droplet lasers, *in vivo* single immune cell tracking, and longitudinal *in vivo* stem cell tracking for cell therapy. In contrast to fluorescence-based imaging and labeling, our microcavity laser emission-based technologies have demonstrated distinct advantages with significantly improved SNR, sensitivity, multimodality contrast, and unique spectral information for labeling different cells.

For ultrasound modulated droplet lasers, this technology leverages both deep penetration depth and high resolution of ultrasound imaging, and the high SNR, imaging contrast and sensitivity of laser emission. I first demonstrated the ultrasound modulated microdroplet lasers in

which the laser emission intensity from the whispering gallery mode (WGM) of a micro oil droplet laser can be enhanced up to 20-fold when the ultrasound pressure reaches a certain threshold. This enhancement in laser emission intensity is reversible when the ultrasound is turned off. Furthermore, the ultrasound modulation of the laser output in the frequency domain was achieved by controlling the ultrasound modulation frequency. Finally, I investigated a potential *in vivo* application of the ultrasound modulated droplet lasing using phantoms vessels containing human whole blood.

For *in vivo* immune and stem cell tracking, I demonstrated a multimodality imaging technology combining optical coherence tomography (OCT), fluorescence microscopy (FM), and lasing emission labeling to longitudinally track the 3D migration trajectories of individual cells transplanted into the subretinal space *in vivo*. The CdS nanowire lasers, with the distinct lasing spectra generated from the subtle differences in the Fabry-Perot microcavity, were utilized as unique identifiers to label the cells. With strong optical scattering and fluorescence emission, CdS nanowires also served as OCT and FM contrast agents to indicate the spatial locations of the cells. FM could provide the overall 2D cell distribution pattern, whereas the nanowires internalized by cells provide unique lasing emission spectra for differentiating individual cells. Meanwhile, OCT imaging could provide both 3D retinal structure and spatial locations of the cells. By integrating the capabilities of FM, OCT, and lasing emission labeling, longitudinal 3D tracking of individual cells in the subretinal space *in vivo* was achieved.

Our study opens a door to utilize microcavity lasers and multimodality imaging platforms to improve imaging quality and solve real-world clinical problems. In the future, our technologies can also be adopted to support both biological researches and clinical applications such as deep

tissue cell tracking, and understanding of the pharmacodynamics (PD) and pharmacokinetics (PK) of cell-based therapies for a comprehensive evaluation of both safety and efficacy.

Chapter 1 Introduction

1.1 Overview of Microcavity Lasers

Lasers are the foundation of modern optics and sensing. Since invented back in the 1960s, lasers have played an important role in our daily life such as laser manufacture, laser display, and laser surgery, etc. [1-4] Therefore, we may all be familiar with different kinds of laser emitters and laser beams. Typically, there are generally three major components to build a laser (Figure 1.1):

1. Bump. It provides the energy source of the laser emission. Usually, the bump can be electric voltage or another beam of light with a shorter wavelength.
2. Gain medium. It is a kind of high quantum yield material that can transfer the energy from the electric power or short-wavelength light to the excited photon emission. In practice, the gain medium can be semiconductors like CdS or high quantum yield fluorescence molecules.
3. Resonant cavity: It is a structure that meets the resonant condition. The transferred light from the gain medium can accumulate in the resonant cavity. When the emission condition is achieved, the lasing emission is coupled out. Two typical resonant cavities have been demonstrated in Figure 1.1. Fabry-Perot resonant cavity is generally two parallel mirrors with high reflectance. The generated light emission will be reflected back and forth between the two mirrors and finally coupled out. Another type of resonant cavity is the whispering gallery mode cavity (WGM). The generated light will be total internal reflected around the boundary of the circular shape resonant

cavity and the lasing emission can be coupled out when the total internal reflection condition does not hold.

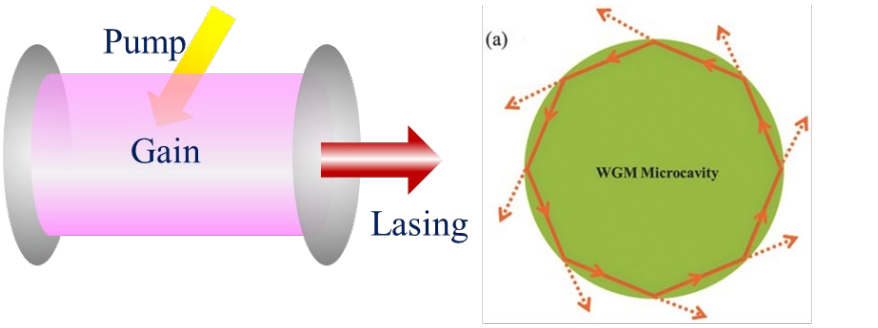

As for micro-cavity lasers, if the resonant cavity is miniature to micro-meter level while maintains a great Q factor and there are still enough bump energy and good gain medium quantum yield, we can still observe lasing emission from the micro-cavity structures. These are so-called microcavity lasers. Owing to the major progress of semiconductor fabrication, semiconductor-based microcavity lasers have been widely applied in many fields [5, 6]. Compared to macroscopic lasers, the advantages of microcavity lasers are:

- Small dimensions: the form factor of micro-cavity lasers is dramatically decreased so that it can be smaller and lighter to fit in some specific application situations like cell labeling and sensing [7, 8].
- Low power consumption: since the gain medium (active region) of the micro-cavity laser is smaller, each micro-cavity laser will consume less power than the normal lasers.

- Low lasing threshold: the microcavity can maintain a great Q-factor and less loss inside of the cavity so typically the lasing threshold of the microcavity lasers is smaller.

The design of microcavity lasers is not aimed to replace conventional lasers. It provides some good options in specific application situations. For example, an important application that conventional laser cannot achieve is to use lasing emission to do sensing and labeling. In the above paragraph, we have described intuitively that light travels back and forth inside the resonant cavity in a microcavity laser. One tiny change in the resonant cavity structure or gain medium inside of it will be amplified significantly in the output lasing emission. Therefore, researchers have utilized microcavity lasers to achieve multiple kinds of sensing tasks. On the other hand, unlike conventional lasers, microcavity lasers may not have only one dominant mode. A microcavity laser can have multiple modes that satisfy the lasing condition. That means there will be multiple emission peaks at various wavelengths in the lasing emission spectra. These peaks in the spectra are purely determined by the micro-resonant cavity structures. Thus, researchers have utilized them as an identifier to label different targets. Those applications will be introduced in the following sections.

1.2 The Application of Microcavity Laser in the Biomedical Field

In recent years, microcavity lasers have drawn wide attention in the biomedical field. Owing to its properties of high light intensity, narrow spectral linewidth, low lasing threshold, and rich spectral information, micro-cavity lasers have been applied to solve multiple types of tasks. Generally, the current applications of microcavity lasers can be divided into 3 categories: biological detection and biomolecule sensing; cell labeling; and imaging and mapping. Here we will introduce some up-to-date researches in those fields.

1.2.1 Biological Detection and Biosensing

Lasing emission-based sensing and detection is majorly based on the changes inside of laser microcavities. The micro-cavities are surrounded by biomaterials or biological samples that will influence the lasing emission components (gain medium or microcavity structure) to provide signal feedbacks. Like it is shown in Figure 1.2, the Fabry-Perot resonant cavity provides a great place for the interaction between the gain medium and the biological solutions. The chemical reaction will influence the quantum yield of the gain medium so that the lasing intensity and threshold will be feedback signals to reflect molecule concentration. Tan et al. have developed an enzyme-linked immunosorbent assay (ELISA) microcavity laser to achieve high dynamic range and high sensitivity biomolecule detection [9]. Wu et al. have exploited the evanescent field of the nanowire lasers to sense the intracellular refractive index change in real time [10].

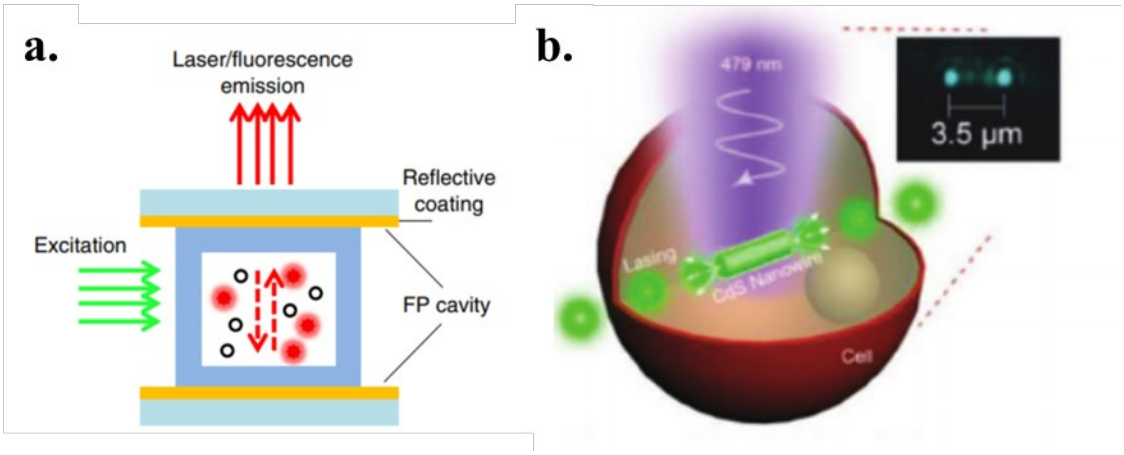

1.2.2 Cell Labeling and Tracking

Given the rich spectral information from the microcavity laser emission spectra, researchers have developed various microcavity lasers for labeling and tracking biomolecules and

cells. Humar et.al utilized dye-doped microbeads and oil microdroplets to generate WGM microcavity lasers inside of both *in vitro* and *situ* cells as a label. The mechanism of unique cell labeling with microcavity lasers was explained in Figure 1.3. For two different cells A and B, they uptake different microcavity lasers with various structures. The lasing emission spectra from A and B show different lasing peak wavelengths. Thus, the two cells can be differentiated via this unique label. Most of the microcavity laser-based labeling is based on this mechanism to identify different cells with the lasing emission spectra from the lasers they are carrying.

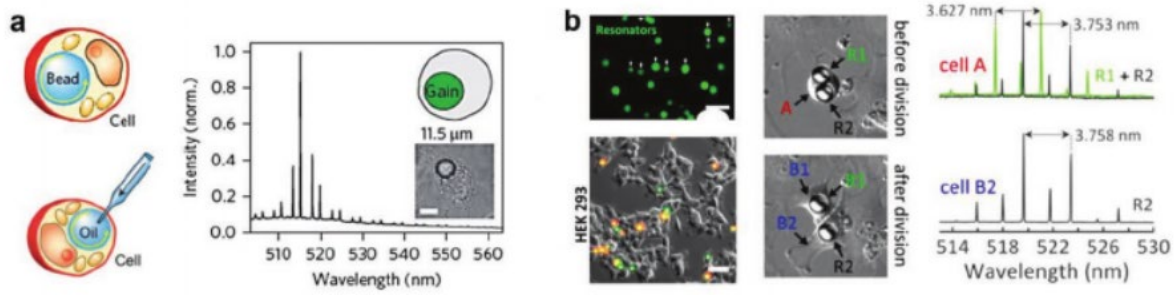

Figure 1.3 Applications of micro-cavity lasers in cell labeling and tracking. [11]Adapted with permission, Copyright 2015, Springer Nature. [12] Adapted with permission, Copyright 2015, American Chemical Society.

1.2.3 Imaging and Mapping

Furthermore, microcavity lasing emission can not only provides sensing and labeling information but could generate 2D spatial information of the biological materials with additional spectral information. The Fan group has developed a scanning imaging platform name lasing emission microscopy (LEM) in which the tissue samples labeled with site-specific fluorophores are sandwiched between two reflection mirrors that build an FP resonant cavity [13]. Like it is shown in Figure 1.4, the tissue sample will be labeled with fluorophores targeted to molecules like DNA. The lasing emission threshold is influenced by the molecule concentration and local tissue morphologies. Therefore, for a normal tissue sample, there will be fewer lasing dots in the scanning

image while the cancer tissues will have more lasing dots which will support early-stage cancer diagnosis [13].

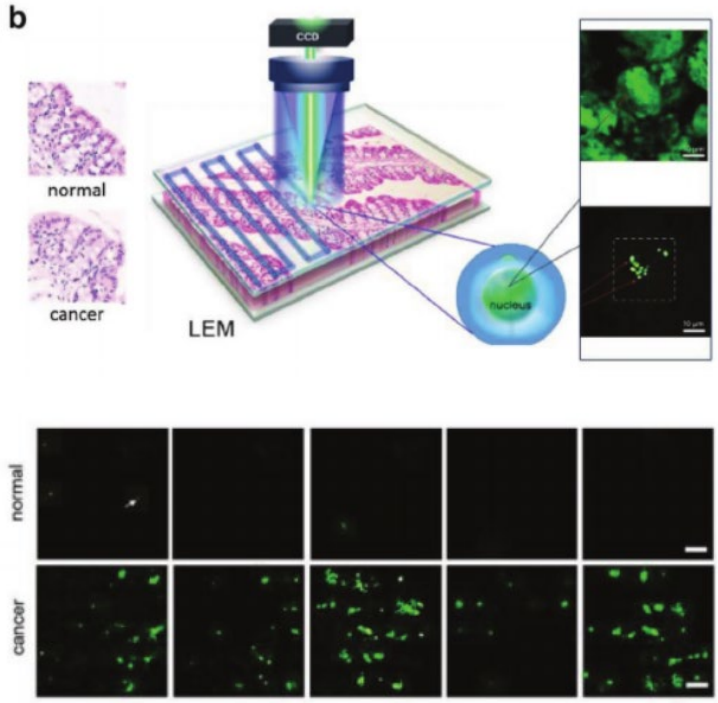

Figure 1.4 Lasing emission applications in imaging and mapping[13]. Adapted with permission, Copyright 2018, Springer Nature.

1.3 Other Types of Optical Labeling Contrast Agents

1.3.1 Fluorescent Labeling

Fluorescence labeling is one of the most popular labeling methods by generating fluorescence emission at another wavelength to improve the imaging contrast for specific targets or regions. The mechanism of fluorescence labeling in optical imaging is to utilize fluorophores molecules combined with some targeting molecules such as antibodies or ligands to indicate the positions of our target molecules, cells, and tissues. During the past decades, fluorescence labeling has been widely applied in biological researches and clinical practices [14-17]. In Figure 1.5, we

briefly summarized the applications of fluorescence labeling in various fields to demonstrate its great success.

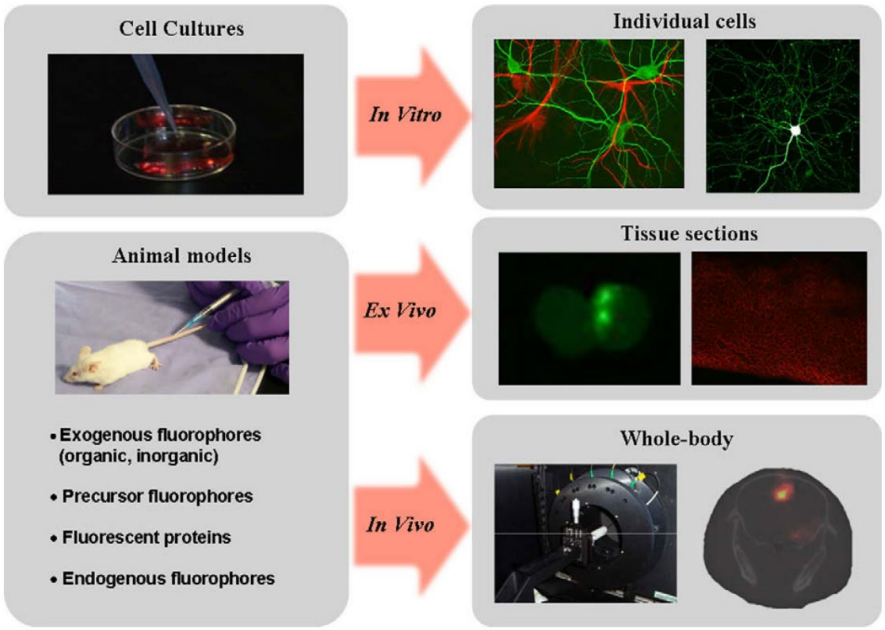

Figure 1.5 The applications of fluorescence labeling [18]. Adapted with permission, Copyright 2010, Elsevier.

Even though fluorescence labeling has been the gold standard of optical contrast agents for many years, it still has many inherent drawbacks that hindered its performance in many situations. First, most of the chemical molecule-based fluorescence labeling methods are suffering from photobleaching. That means, after strong excitation or long excitation time, the emission intensity of fluorophores will decrease significantly, which brings challenges in longitudinal studies and other researches based on the quantification of fluorescence emission intensity. Second, since all the fluorophores are homogenous, if we want to track different targets in the same field of view, it will be impossible to differentiate them. Some researchers have integrated multiple fluorophores in one DNA probe to get color barcoding [19]. But the number of different labels is still limited, and that technology required confocal microscopy to identifier the color-coding that is impractical for *in vivo* applications. Thirdly, considering the scattering and autofluorescence from tissue, the

sign-to-noise ratio of fluorescence labeling *in vivo* is not satisfying. Lastly, without the help of confocal microscopy, fluorescence microscopy could only provide 2D projection images of 3D information. For *in vivo* studies, we have to rely on other modalities or multimodality systems to acquire 3D information. Above drawbacks are the major drivers that guide us to work on using the microcavity lasers with multimodality imaging to further improve the performance and application situations.

1.3.2 Quantum Dots

Recent advances in nanotechnology have paved the way for using quantum dots (QD) as optical contrast agents for *in vivo* imaging. Generally speaking, quantum dots are nanometer-sized semiconductor/metal-oxide particles (e.g., CdSe/CdTe) that could generate fluorescence emission under external excitation. As shown in Figure 1.6, researchers have developed numerous targeted QD probes by combining QD with antibodies and other bio-ligands [20-22]. After being introduced into the tissue or animal bodies, the targeted QD probes can be guided towards the diseased sites and generate additional fluorescence emission for researchers and doctors to locate and quantify the disease regions or the distribution of specific biomolecules and cells.

The major advantages of quantum dots are small size (5-100 nm), relatively strong fluorescence emission, low cost to fabricate, and long-term stability. Thus, a lot of researchers have developed optical imaging contrast agents based on QDs. For example, work published by Nie and their co-workers has demonstrated QDs as contrast agents for cancer detection and imaging [23]. Meanwhile, researchers have developed NIR QD probes that could provide decent imaging depth at deep tissue [24].

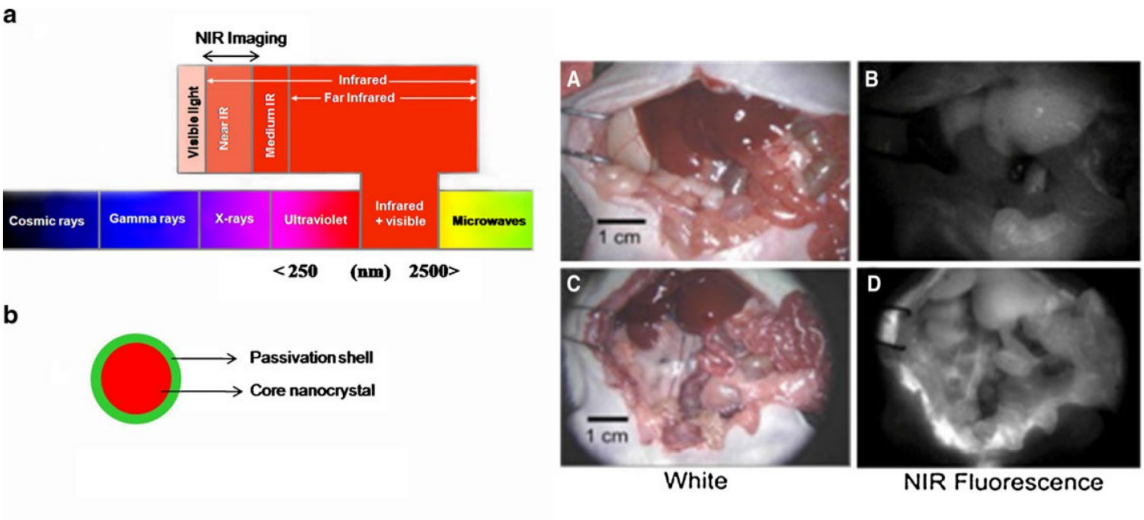

Figure 1.6 Schematic of target QD probes and the optical microscopy image of the fluorescence emission from a single QD [24]. Adapted with permission, Copyright 2017, American Chemical Society.

Like other fluorescence-based imaging contrast agents, QDs labeling has similar drawbacks. First, all the QDs are homogenous in optical properties and emissions. Thus, we cannot utilize them to track multiple targets at the same time unless we introduce other kinds of QDs with different emission colors. But the total number of labels is still limited. Second, considering the omnipresent scattering and autofluorescence of tissues, the signal-to-noise (SNR) ratio is not ideal as well. Besides, another drawback of QDs is the long-term toxicity of heavy metal ions. Lastly, for *in vivo* applications, QD based fluorescence microscopy could only provide 2D information of the target distribution while 3D information is critical for diagnosis and other research purposes. Even though QDs have great potentials in many applications, the aforementioned drawbacks may limit its applications in cell tracking *in vivo*.

1.3.3 Scattering and Absorption-based Contrast Agents

Other types of optical imaging contrast agents include scattering and absorption-based nanoparticles. Optical coherence tomography (OCT) is a scattering-based imaging modality that is broadly applied and investigated. The imaging contrast comes respectively from the scattering

intensity of tissues and particles. Hence, to get additional contrasts in OCT, researchers have developed various types of nanoparticles to improve the signal-to-noise ratio by increasing scattering. Gold nanoparticles are particularly popular due to the strong scattering and absorption properties generated by plasmonic resonance [25-27]. In Figure 1.7, the nanofabricated gold nanocages are shown as distinct contrast agents for OCT.

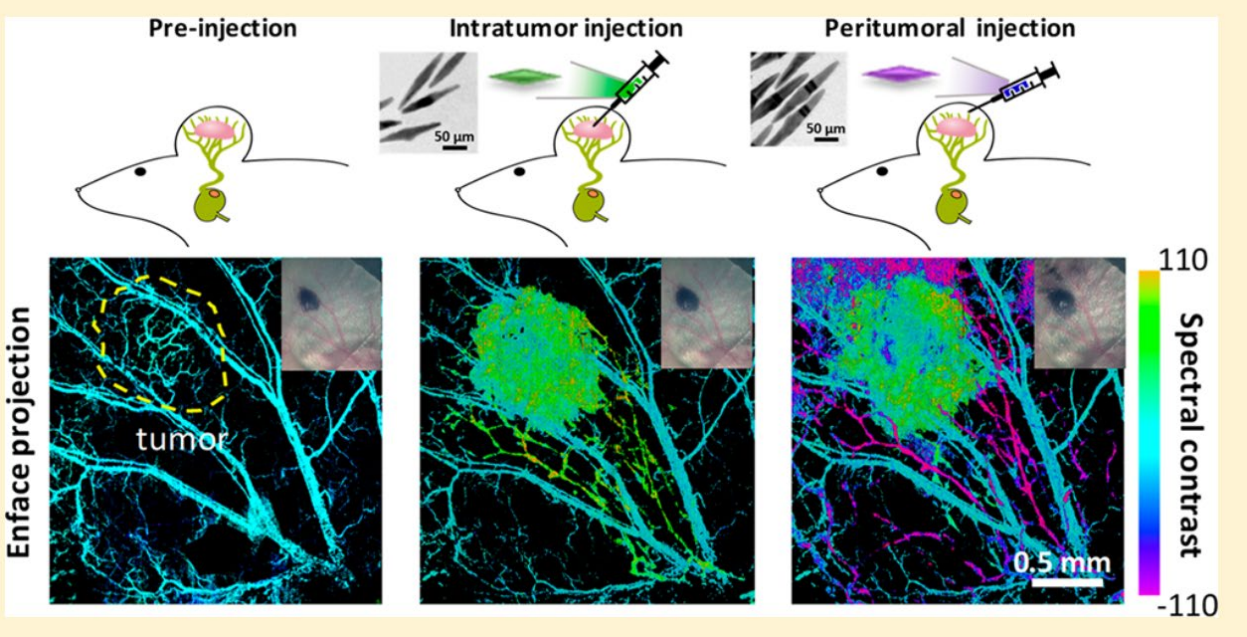

Figure 1.7 Gold nanoparticles as OCT contrast agents. The SEM image of gold nanoparticles and the en-face image of the contrast enhanced tumor OCT images [28]. Adapted with permission, Copyright 2020, American Chemical Society.

Even though the gold nanoparticles are very popular, they also have some limitations: First, they are homogenous contrast agents. All the labeled targets are the same and cannot be differentiated. Second, considering the nanometer-level size, the additional contrast provided is relatively poor comparing with the strong optical scattering in biological tissues.

Here we summarized the properties of optical contrast agents and compared them with our microcavity lasers. Our microcavity laser-based contrast agents have higher contrast, great SNR ratio, long lifetime, multimodal contrast, and the capability to provide unique labels for various

targets. It has a strong potential to be applied in various imaging applications and fields in the future.

	QD	FL	Scattering	Microcavity lasers
Size	~20 nm	~1 nm	~100 nm	~5 um
Contrast	Low	Low	Medium	High
Reliability	Long	Short	Long	Long
Label uniqueness	No	No	No	Yes
3D information	No	No	No	Yes

Table 1 A comparison of types of optical labeling contrast agents.

1.4 Overview of Multimodality Imaging System

In clinical applications, medical imaging aims to collect as much information as possible with the best resolution to support the diagnostic and evaluate the efficacy of treatments. However, there are two main challenges for single modality imaging in clinical practice: first, single modality imaging could only provide information from one perspective. That may not be enough to make a complete diagnostic decision. For example, an X-ray image could only provide detailed structural information of the patients, while functional information such as blood vessels and specific biomarkers distributions are also necessary to determine the severeness of the illness. Second, modalities with the highest sensitivity often have a relatively poor resolution or penetration depth and vice versa. The idea of using multiple modalities in conjunction to conduct imaging for the same target with complementary performance in sensitivity, resolution, and penetration depth has been very popular among researchers and physicians [29-31]. Since the first multimodality system was developed in 1998 that combined PET and CT [32], in the past decades, the multimodality imaging technologies in radiology have been well studied and commercialized. On the other hand,

multimodality imaging with non-radiative modalities has been a hot research topic in the recent years to solve specific clinical tasks that need higher resolution and more function information in a low cost and safe way. In the following sections, we majorly focused on the review of non-radiative multimodality imaging technologies developed based on optical imaging and ultrasound imaging.

1.4.1 Multimodality Imaging Based on Optical Imaging

Optical multimodality imaging technologies are very popular in the biomedical field. Owing to its simplicity of use, real-time imaging, providing multiple detection markers simultaneously, high spatial resolution, and wide image field from subcellular structures to whole bodies [29, 33, 34], optical imaging modalities are widely applied in biological research, fluorescence-guided diagnosis, and endoscopic imaging.

However, due to the scattering, imaging depth is the major challenge for all types of optical imaging modalities. Quantum dots (QD) mentioned in Section 1.3 have been utilized as novel multimodality labels with high quantum yield, broad emission absorption, and long-term stability. For example, researchers have used PLGA polymer to encapsulate QDs and iron oxide nanoparticles to generate dual-modal imaging contrast agents for fluorescence microscopy and MRI [35]. Here, QDs providing fluorescence emission for optical microscopy whereas bundled iron oxide nanoparticles could provide additional MRI contrast. Up-conversion nanoparticles (UCNPs) are another type of dual-modality contrast agent that attracted great attention [36]. Unlike conventional fluorescence nanoparticles, UCNPs could generate higher-energy visible light when excited by a long wavelength of near-infrared light. In addition, by controlling the compositions, multifunctional UCNPs could be fabricated for CT/PET dual-modality contrast.

1.4.2 Multimodality Imaging Based on Ultrasound Imaging

Ultrasound (US) imaging is a widely applied imaging technology based on the reflections of the ultrasound wave between tissues with different acoustic impedance. The advantages of US are deep penetration depth, real-time imaging, low cost, and safety [37]. However, ultrasound imaging techniques are suffering from low resolution and sensitivity. Microbubbles are a typical ultrasound contrast agent considering the large acoustic impedance. Additionally, fluorescence-labeled microbubbles have been developed to achieve dual-modality imaging [38]. Also, nanoscale liquid−liquid emulsions, gas−liquid emulsions, and solid nanoparticles have been reported to contribute to enhancing the contrast of US imaging [39].

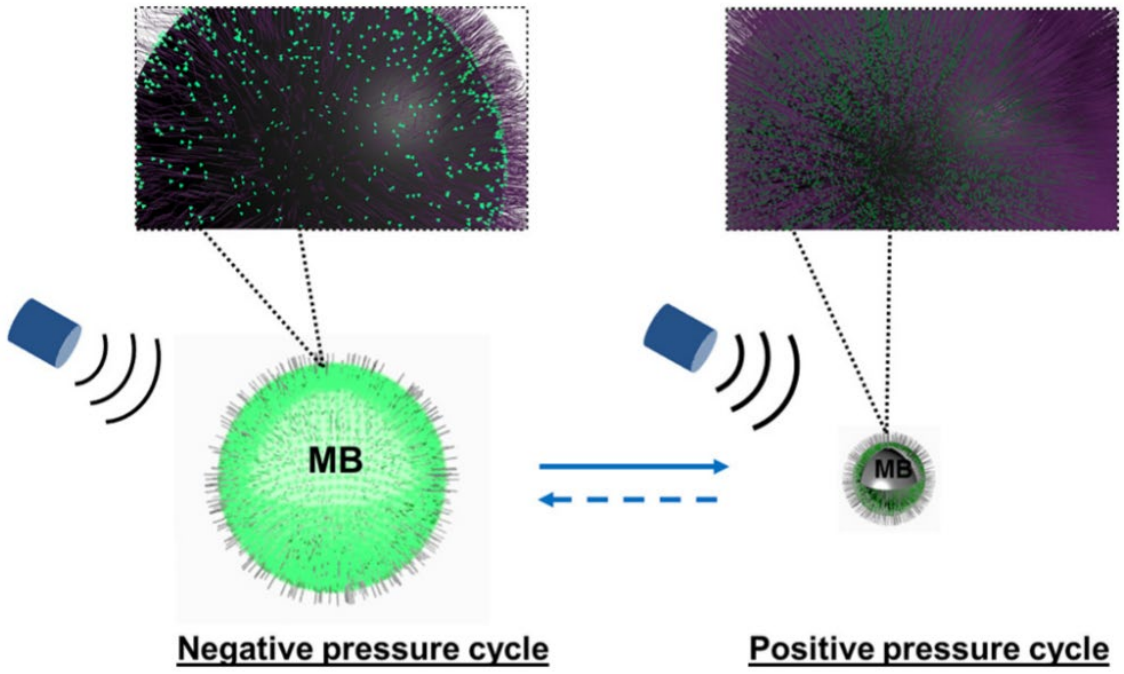

Figure 1.8 Ultrasound modulated fluorescence emission of microbubbles [40]. Adapted with permission, Copyright 2014, SPIE.

1.5 Motivations for Micro-cavity Lasers in Multimodality Imaging

In the above sections, we have discussed about the broad applications of multimodality imaging and different optical labeling contrast agents. Owing to the omnipresent scattering in

tissue, the signal-to-noise ratio of conventional optical labeling technologies such as fluorescence will drop significantly as the imaging depth increase. Moreover, current optical contrast agents are mostly homogenous in optical properties. It could only demonstrate the overall distribution pattern while providing differentiable information for different targets is impossible. These obstacles hinder the applications of multimodality imaging systems in many clinical situations.

The challenges of advanced optical labeling methods and imaging systems described above motivated us to explore and develop various labeling technologies and multimodality imaging platforms, which can be utilized to identify different targets and different preclinical and clinical settings. Thus, this thesis aims to develop microcavity lasers serving as novel multimodality contrast agents that could provide useful biological information, improve image quality and fuse the strengths of different modalities. The unique spectral and lasing emission intensity of the microcavity lasers will be exploited to both improve the signal-to-noise ratio in deep tissue and provide unique labels to differentiate different targets that beat fluorescence counterparts. The significance of this thesis is to develop novel imaging contrast agents and multimodality imaging system that opens a door for future deep tissue imaging, understanding the activities of cells in animal bodies for biological research purposes, as well as evaluation of the pharmacokinetic (PK) and pharmacodynamic (PD) of cell therapy.

1.6 Organization of Thesis

In this thesis, we explored several potential applications of microcavity lasers in the multimodality imaging system to solve various problems in the biomedical field. We first investigated the applications of droplet microcavity lasers integrating with optical microscopy and ultrasound to achieve remote modulation of lasing emission intensity. This technology provided a practical method to tune the emission intensity of the resonant cavity in a non-contact way. By

introducing a lock-in amplifier style frequency modulation, it could open a door for high signal-to-noise ratio contrast agents in deep tissue. Furthermore, we developed an *in vivo* single cell tracking technology with nanowire lasers and an optical multimodality imaging system. This technology could give each individual cell a unique spectral identifier and record the 3D spatial locations of the cells during their migration over time. It provides a novel tool for biological researches and clinical therapies to understand the activities of immune cells and external stem cells registered by the therapies.

For Chapter 2, ultrasound modulated droplet lasers were demonstrated. In Chapter 2, we observed the ultrasound lasing enhancement phenomenon, conducted the theoretical calculation, and exploited the phenomenon to control the lasing intensity in the frequency domain *(published in ACS Photonics,2019 [41]; filed US Patent: 17/421,809)*.

For Chapters 3 and 4, we developed the *in vivo* single cell tracking technology with nanowire lasers and a multimodal optical imaging system. In Chapter 3, we utilized the CdS nanowire lasers to label macrophages. Since the micro-resonant-cavity structures are different for nanowires with randomly distributed lengths, the emission spectral could perform as a unique "identifier" to differentiate labeled cells. Combining with the optical coherence tomography (OCT), fluorescence microscopy (FM), and lasing emission spectrometer multimodality imaging system, the concept of single immune cell tracking technology was proven. (*published in Biomedical Optics Express [42]*). In Chapter 4, we further upgraded the technology with biocompatible coated nanowire lasers and a high-resolution spectrometer to significantly improve the number of tracked cells. Stem cells utilized to restore the damaged retina structures were tracked in the subretinal space longitudinally. This novel technology could potentially support the

safety evaluation of stem cell therapies (*under review in BME Frontier; filing US Patent: PCT/US2021/015475*).

To conclude, Chapter 5 covers a brief summary of the whole thesis and future outlooks to further improve the technologies and push them towards real-world clinical applications.

Chapter 2 Ultrasound Modulated Droplet Lasers

2.1 Motivation for Ultrasound Droplet Laser Modulation

Fluorescence imaging is one of the most commonly used technologies in biomedical applications. When applied to biological tissues beyond the surface, the spatial resolution and sensitivity of fluorescence imaging are degraded, which is due mainly to the overwhelming optical scattering in the tissues and also affected by the background autofluorescence [14, 15, 43, 44]. On the other hand, ultrasound imaging (US), owing to the much lower scattering of ultrasound waves in biological tissues, can keep its spatial resolution in deep tissues much better than fluorescence imaging. Therefore, high-frequency ultrasound is not only employed for imaging [45-47] but also adapted to treatment such as tumor therapies [48-50], drug release [51, 52], and nerve stimulation [53-55]. Recently, ultrasound modulated fluorescence imaging [56, 57] has been explored, aiming to improve fluorescence imaging by leveraging the advantages of ultrasound in spatial resolution and tissue penetration. In this technique, ultrasound wave at a certain frequency is focused in a scattering medium (such as an optically scattering biological tissue), changing the scattering property in the medium thus modulating the photons transmitting through the ultrasound modulated area. When building an image from the medium, only the modulated photons carrying the ultrasound frequency will be used while the non-modulated photons will be filtered out. Although holding the potential to improve the spatial resolution of optical imaging, this method suffers from a low signal-to-noise ratio (SNR) resulting from the limited modulation depth, which is defined as the modulated photons over the total photons detected. In an alternative method of

ultrasound modulated optical imaging, microbubbles labeled with fluorophores and quenchers were used [38, 58]. The volume of a microbubble is changed under the ultrasound pressure wave, leading to the emergence of fluorescence due to the increased distance between the fluorophores and the quenchers. Since this method still relies on the detection of fluorescence, which is weak in intensity and broad in spectrum, its SNR and spatial resolution are still limited.

In contrast to fluorescence-based detection and imaging, microcavity laser emission-based detection and imaging have recently emerged as a novel technology in biomedical research. Compared to fluorescence, laser emission has strong intensity and extremely narrow linewidth, which leads to significantly improved SNR, imaging contrast, and sensitivity in sensing biological changes [59-61]. Previously, laser emission has been used in ultra-sensitive molecule detection[9, 62, 63] and cancer diagnosis [13, 64-66]. Additionally, micron- and submicron-sized lasers have been implanted into cells, biological tissues, and live animals to track cells and detect subtle biological changes [67-70].

In this project, we explored the ultrasound modulated microcavity lasers, which, if feasible, could leverage the deep tissue penetration and the high resolution of ultrasound imaging and the high SNR, imaging contrast, and sensitivity of laser emission. As an important step towards the ultrasound modulated laser emission-based microscopy, we first demonstrated the ultrasound modulated microdroplet lasers (Figure 2.1(a)), in which the laser emission intensity from the whispering gallery mode (WGM) of an oil droplet laser can be enhanced up to 20-fold when the ultrasound pressure reaches a certain threshold. This enhancement in laser emission intensity is reversible when the ultrasound is turned off. The lasing enhancement under different ultrasound frequencies ranging from 500 kHz to 10 MHz was investigated. Furthermore, the ultrasound modulation of the laser output was achieved by controlling the ultrasound pressure, the duty cycle,

and the modulation frequency. Finally, we explored a potential application of the ultrasound modulated droplet lasing in biology and medicine using phantoms vessels containing human whole blood.

2.2 Experimental Setup and Methods

2.2.1 Experimental Setup

In this study, a typical confocal setup was used to excite the oil droplet lasers and collect emission light. (Figure 2.1 (a)). A pulsed diode laser (pulse width: 2 ns, tunable repetition rate from 20 to 799 Hz) at 473 nm was loosely focused through a 20 mm focal length cylindrical lens to excite the oil microdroplets in microwells or capillaries. In the control experiments, a pulsed OPO laser (pulse width: 5 ns, repetition rate: 20 Hz) with 485 nm was applied to excite polystyrene beads doped with FITC. The pump intensity was controlled by a continuously variable neutral density filter. The emission light was collected through the same lens and sent to a spectrometer (Horiba iHR550, spectral resolution ~0.2 nm) for further analysis. For ultrasound modulation, focused ultrasound transducers with 500 kHz, 2.5 MHz, 10 MHz central frequency (500 kHz: H107, Sonic Concepts, Bothell, WA; 2.5 MHz: V307, Olympus Inc.; 10 MHz, V322, Olympus, Inc.) were driven by a function generator (Stanford Research Systems DS345) and a power amplifier (37 dB, custom design) to generate the desired ultrasound signals. An ultrasound coupling cone was placed between the transducer and microwells containing droplets lasers to transmit ultrasound. A commercial calibrated hydrophone (ONDA HNC-1500) was used to measure the applied ultrasound pressure during the experiments at the focus of the ultrasound field.

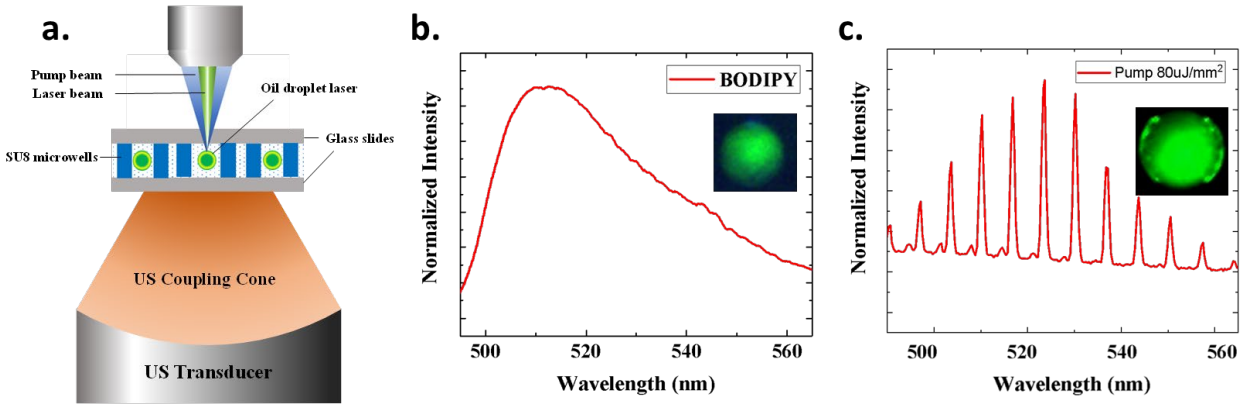

Figure 2.1 Experimental setup and microdroplet lasers. (a) Schematic of the optical and ultrasound (US) setup, in which the oil droplets were trapped inside microwells. The oil droplets doped with BODIPY were excited by a pulsed diode laser (pulse width=2 ns; wavelength=473 nm) whereas a focused ultrasound beam transmitted through the coupling medium. (b) Fluorescence spectrum of a single oil droplet in the microwell below the lasing threshold. Inset is a CCD image of the droplet. Scale bar: 50 μm. (c)Lasing emission spectrum of the same oil droplet laser with pump energy above lasing threshold (80 μJ/mm^2). The multiple lasing peaks have been observed.[41] Adapted with permission. Copyright 2019, American Chemical Society.

2.2.2 Generation of Microdroplets

Throughout the experiments, the microdroplets were prepared with a standard oil-in-water dispersion procedure [71]. The lipophilic fluorescence dye, BODIPY, was dissolved in biocompatible and easy-to-obtain corn oil (refractive index RI=1.46) (Figure 2.1(b)). 15 μL corn oil doped with BODIPY was mixed with 985 μL diluted detergent and the mixture was shaken for 5 minutes until the oil was dispersed uniformly in the solvent. Under the effect of surface tension, microdroplets had a spherical shape of 30-50 μm in diameter. Following this, microdroplets were loaded into microwells (Figure 2.1(a) and the inset of Figure 2.1(b)). In experiments, we diluted the microdroplet solution prepared above 25× in order to easily observe single droplets. BODIPY used in this study was purchased from ThermoFisher (Catalog #D3921). Detergent and dichloromethane were purchased from Sigma-Aldrich. Corn oil was purchased from a local supplier.

2.2.3 Microwells and Capillaries

A 3×3 array of microwells 50 μm in depth and 1 mm in diameter were fabricated in a biocompatible negative photoresist SU-8 on the surface of a 1" × 1" glass slide using standard soft lithography. The mirrors were first cleaned by solvent ultrasonication (sonicated in acetone, ethanol, and de-ionized water sequentially) and oxygen plasma treatment. Then, they were dehydrated at 150 °C for 15 minutes right before a 50 μm thick SU-8 2025 (MicroChem Corp., USA) layer was spin-coated on the top of the mirrors. After soft-baking the SU-8-coated mirrors for 3 minutes at 65 °C and 8 minutes at 95 °C, a contact lithography tool Karl Suss MA 45S was used to UV-expose the mirrors through a mask. The exposed mirrors were subsequently subjected to post-exposure baking at 65 °C for 1 minute and 95 °C for 6 minutes, followed by 8 minutes of development. After rinsing and drying, the microwell array was further hard baked at 150 °C for 10 minutes and treated with oxygen plasma to improve hydrophilicity. Before experimental measurement, the microdroplet solution was dripped into the microwells, which were then covered with a glass slide.

The glass capillary, which was used to simulate a blood vessel, was purchased from Thomas Scientific. It had a diameter of 700 μm and a wall thickness of 100 μm. To start with, the microdroplet solution was diluted 20× and mixed with human whole blood. Then the mixture was injected into the capillary, which was later sealed with UV curable epoxy (NOA 81). Finally, the capillary loaded with the sample was submerged 1 mm into ultrasound coupling gel.

2.3 Theoretical Calculation

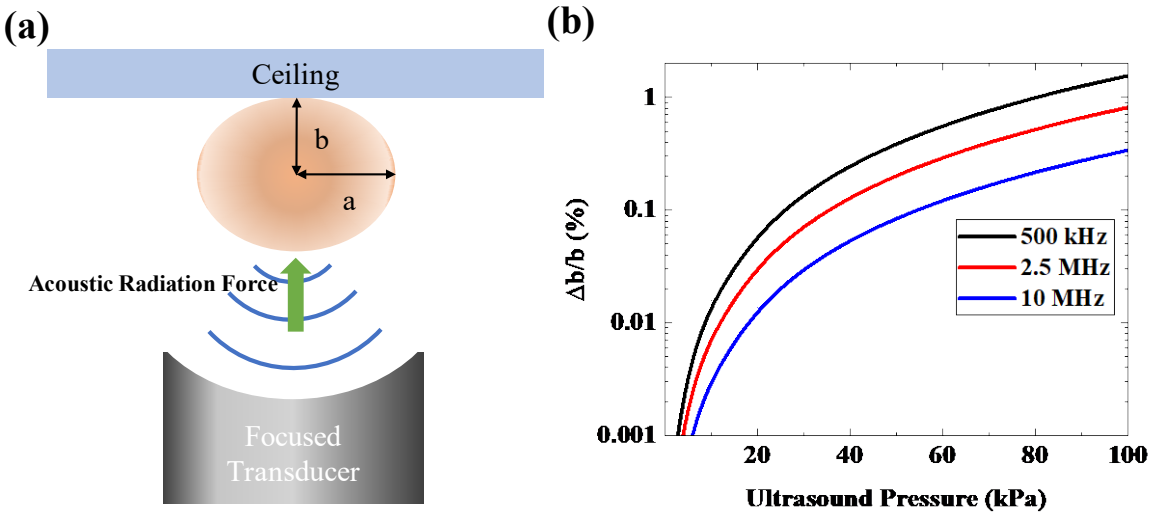

Figure 2.2 The deformation caused by acoustic radiation force. (a) Schematic of the deformation model. (b) Theoretical calculation of the radius deformation ratio of an oil droplet as a function of the ultrasound pressure. [41] Adapted with permission. Copyright 2019, American Chemical Society.

The modulation of microdroplet lasing emission is achieved by introducing the acoustic radiation force of ultrasound to deform the micro resonant cavity to generate an asymmetric resonant cavity effect. Therefore, the lasing emission will be directional rather than isotropic so that we can observe a stronger emission intensity at a certain angle. Here we provide a quantitative estimation of acoustic radiation force in the focused ultrasound field and the corresponding deformation of a droplet-based on its surface tension. We make the following assumptions: (1) The droplet is isotropic and compressible; (2) The radius of the sphere, r (25 μm), is much smaller than the acoustic wavelength, λ_a (3 mm at 500 kHz); (3) The surrounding fluid is non-viscous; (4) The ultrasound field is axial symmetric; (5) $kR \gg 1$, where k is the wavenumber of ultrasound and R is the radius of the sound source. Following the derivation in the literature, the acoustic radiation force on the droplet along the axial can be expressed as [72]:

$$\textit{Equation 1:}\quad F_a = \left(\frac{A_\alpha + 4B_\alpha}{2c}\right)\frac{\partial I}{\partial z}$$

Where:

$$\boldsymbol{A_\alpha = \frac{12\pi r^3}{(1+\delta_0^2)^3\left\{\frac{1}{[9\nu(1-\Omega^2)\delta^2]}-\frac{\nu}{[3(1-\Omega^2)(1+2\nu)]}\right\}}}$$

$$\boldsymbol{B_\alpha = \frac{\frac{4}{3}\pi r^3(\nu-1)}{1+2\nu}}$$

$$\boldsymbol{\delta_0 = \frac{(kr)^3\left(\nu-\frac{1}{\delta^2}\right)}{[3\nu(1-\Omega^2)]}}$$

$$\boldsymbol{\Omega = \frac{w}{w_0} = \frac{w}{\sqrt{3\nu}c\delta/r}}$$

$$\boldsymbol{I = \frac{|p|^2}{2\rho_0 c}}$$

I is the sound intensity. z is the axial direction of the ultrasound field. c is the sound speed in the surrounding solution. c_s is the sound speed in the droplet. w is the angular frequency. w_0 is the angular resonance frequency of droplet, $\delta = \frac{c_s}{c}$ is the ratio of the sound speeds. $k = \frac{w}{c}$ is the wavenumber. ρ_s is the density of the droplet. ρ is the density of the surrounding solution. $\nu = \frac{\rho_s}{\rho_0}$ is the ratio of the densities. p is the ultrasound pressure.

In Equation 1, $(\frac{A_\alpha+4B_\alpha}{2c})$ is determined by the material and size of the droplet. $\frac{\partial I}{\partial z}$ can be estimated experimentally. We can measure the pressure difference of a small step Δz and calculate ΔI so that $\frac{\partial I}{\partial z}$ can be estimated with $\frac{\Delta I}{\Delta z}$. Inserting the numerical value for each parameter (US frequency: 500 kHz): r =25 μm, c =1450 m/s, $\nu = 0.93$, δ = 0.9, $w = 2\pi \times 500000/\mathrm{s}$, we have:

Equation 2: $$F_a = 5.74 \times 10^{-18}\frac{\partial I}{\partial z}$$

Then we analyze the droplet deformation with a surface tension-dominated model (Figure 2.2 (a)) [73]. When the acoustic radiation force, F_a, is balanced by the restoring surface tension force, F_{st}, which can be expressed as:

Equation 3: $$F_{st} = -2\pi a\gamma + \pi a^2\gamma\left(\frac{1}{a}+\frac{a}{b^2}\right)$$

Where a is the equatorial radius, b is the vertical conjugate radius, and γ is the surface tension coefficient. At a small deformation, Equation S8 can be linearized as:

$$F_{st} = 3\pi\gamma\Delta b$$

The force balancing equation can be expressed as:

$$F_a - F_{st} = 0$$

By combining Equations 1-3 while keeping the volume constant, i.e., $\frac{4}{3}\pi r^3 = \frac{4}{3}\pi a^2 b$ and inserting $\gamma = 0.005\mathrm{N/m}$, we get the deformation ratio, $\Delta b/b$, as a function of F_a:

$$\frac{\Delta b}{b} = 4.88 \times 10^{-12} \frac{\partial I}{\partial z}$$

Combining the above equations, we have:

Equation 4: $\frac{\Delta b}{b} = 3.25 \times 10^{-18} p \frac{\partial p}{\partial z}$

Here p and $\frac{\partial p}{\partial z}$ can be experimentally measured (i.e., 500 kHz US, p = 50 kPa, $\frac{\partial p}{\partial z} = 2.4 \times 10^{10}\ Pa/m.$). Finally, the deformation ratio for an oil droplet of 50 μm in diameter immersed in water under the 500 kHz US wave is plotted in Figure 2.2(b). Similarly, the deformation ratio for 2.5 MHz and 10 MHz US waves can also be calculated and plotted in Figure 2.2(b). Based on calculation, 500 kHz US at 30 kPa and 50 kPa can generate a radiation force of 1.65 nN and 4.59 nN, respectively, and the corresponding deformation ratio of 0.14% and 0.39%, respectively.

Through the experimental results, we can also estimate the deformation by examining the whispering gallery mode spectral shift. For a whispering gallery mode, the resonant wavelength, λ, can be expressed as:

$$nl = N\lambda$$

Where n is the refractive index of oil, l is the perimeter of a vertical cross-section orbit, N is the mode constant. The resonant wavelength shift of a droplet laser is proportional to the perimeter change in a whispering gallery mode orbit.

$$\Delta\lambda = \lambda \frac{\Delta l}{l}$$

The perimeter change due to the deformation of vertical cross-section orbit can be calculated as:

$$\Delta l = l - l_0 = 2\pi r - \pi[3(a+b) - \sqrt{(3a+b)(a+3b)}$$

During lasing enhancement with US, we did not observe any resonant peak shift at 50 kPa. Therefore, the peak shift, $\Delta\lambda$, should be below the spectrometer resolution (0.1 nm). Combining Equations above and using $n = 1.46, r = 25\ \mu\text{m}$, and $\lambda = 540\ \text{nm}$, we can estimate the upper limit for the corresponding deformation ratio based on the following two assumptions:

(1) Conservation of volume for the 3-D model: $\frac{4\pi}{3}r^3 = \frac{4\pi}{3}a^2b$,

$$\frac{\Delta b}{b} < 0.1\%$$

(2) Conservation of cross-section area for the 2-D model: $\pi r^2 = \pi a^2 b$,

$$\frac{\Delta b}{b} < 1.5\%$$

The actual deformation ratio should be between these two ideal estimations.

2.4 Results and Discussions

2.4.1 Lasing Enhancement with Ultrasound

Initially, the lasing spectra of the microdroplet laser were studied under a relatively low ultrasound pressure (10 kPa at 500 kHz). During the measurements, the microdroplet lasers were trapped and observed at the same position and with a constant pump energy density of 35 μJ/mm^2. To demonstrate the effect of ultrasound, the lasing spectra of the microdroplet laser were recorded before, during, and after continuous ultrasound exposure (Figure. 2.3(a)). Obviously, neither the lasing intensity nor the spectral peak position changed with the "low" ultrasound pressure, suggesting that small ultrasound disturbance does not affect droplet lasing behavior. In contrast, with a stronger ultrasound pressure (50 kPa at 500 kHz), significant enhancement (~20 times) in lasing intensity was observed when the ultrasound was turned on (Figure 2.3(b)). In particular, strong lasing emission emerges from the rim of the droplet (see the inset of Figure 2.3(b)). Furthermore, the enhancement is reversible. The lasing intensity falls back to the normal level when the ultrasound was turned off. During the ultrasound lasing enhancement, the lasing modes and their spectral positions remained the same (within the spectrometer resolution), indicating that

the ultrasound, at the given pressure, did not cause any significant change in the shape and size of the oil microdroplets (consistent with our calculation in Section 2.2). In Figure. 2.4, we investigated the microdroplet lasing threshold with and without exposure to the ultrasound pressure. It was found that the lasing threshold was reduced from 19 μJ/mm^2 to 11 μJ/mm^2 with a 10× increase in the intensity efficiency (the slope of the laser output) when the microdroplet was exposed to the ultrasound pressure of 50 kPa.

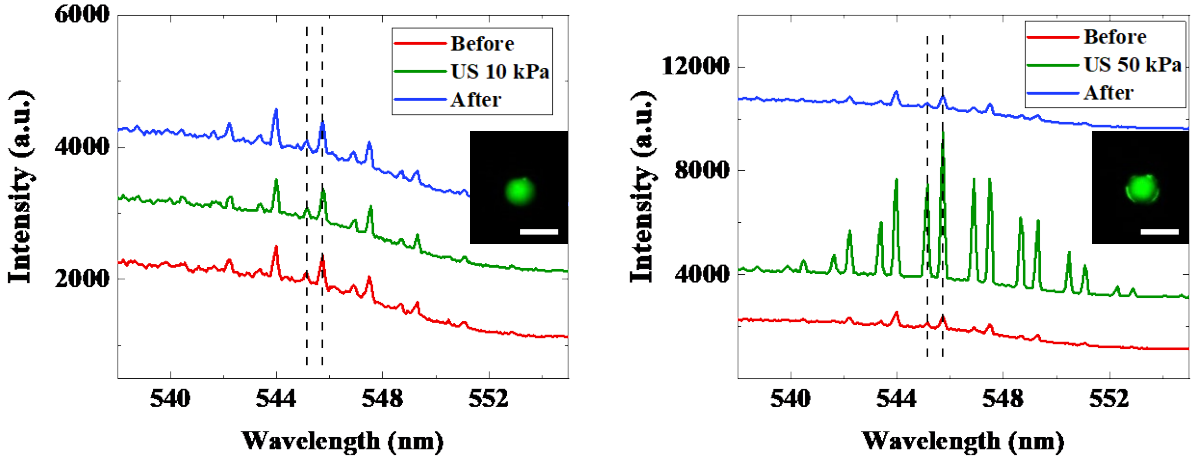

Figure 2.3 Lasing enhancement with exposure to ultrasound. The same 45 μm diameter oil droplet laser was investigated, and the same ultrasound (US) frequency of 500 kHz was applied in (a)-(b). (a) Lasing spectra of the oil droplet laser before, during, and after applying US pressure of 10 kPa. Inset is a CCD image of the droplet laser without US. (b) Lasing spectra of the oil droplet laser before, during, and after applying US pressure of 50 kPa. Inset is a CCD image of the droplet laser with US. All curves in (a) and (b) were obtained under the same pump energy density of 35 μJ/mm^2. Curves in (a) and (b) are vertically shifted for clarity. Dashed lines in (a) and (b) are guides for better observation of the lasing wavelength. Scale bars in (a) and (b): 50 μm. [41] Adapted with permission. Copyright 2019, American Chemical Society.

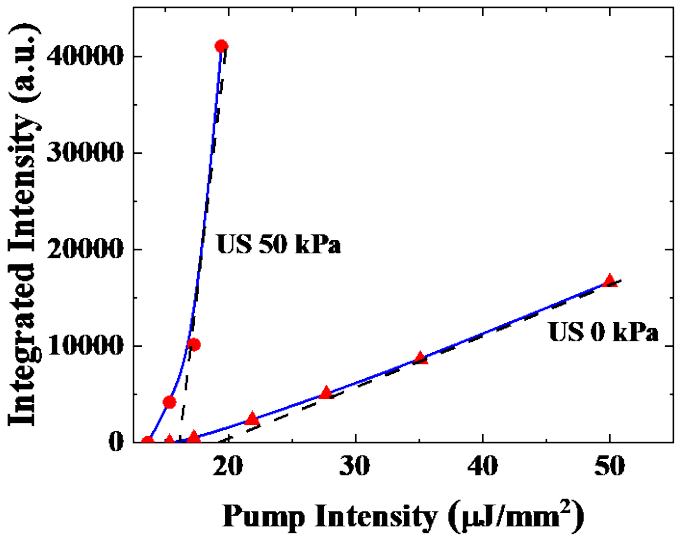

Figure 2.4 Laser output integrated over the spectral range of 540–560 nm as a function of the pump energy density. The measurements with ultrasound (50 kPa) and without ultrasound (0 kPa) exposure are compared. The dashed lines are the linear fit above the respective lasing thresholds under ultrasound pressure of 50 kPa and 0 kPa. With the exposure to 50 kPa ultrasound, the lasing threshold is reduced from 19 μJ/mm^2 to 11 μJ/mm^2.[41] Adapted with permission. Copyright 2019, American Chemical Society.

We further investigated the relationship between the microdroplet lasing intensity and the ultrasound frequencies. As the result shown in Figure 2.5, all the lasing spectra were acquired with the same integration time of 1 s under the fixed pump energy density of 40 μJ/mm^2. Focused ultrasound transducers worked at various frequencies (500 kHz, 2.5 MHz, and 10 MHz, respectively) were utilized to generate the continuous ultrasound that was applied to microdroplet lasers. We noticed a pressure threshold of around 30 kPa for all three ultrasound frequencies. Below the pressure threshold, no enhancement in laser intensity was observed (see also Figure 2.3(a)). While above the pressure threshold, the enhancement became linearly proportional to the ultrasound pressure. In addition, it seems that the US with lower frequency led to higher enhancement, as demonstrated by the steeper slope above the pressure threshold in Figure 2.5(a) compared to those in Figures 2.5(b) and (c).

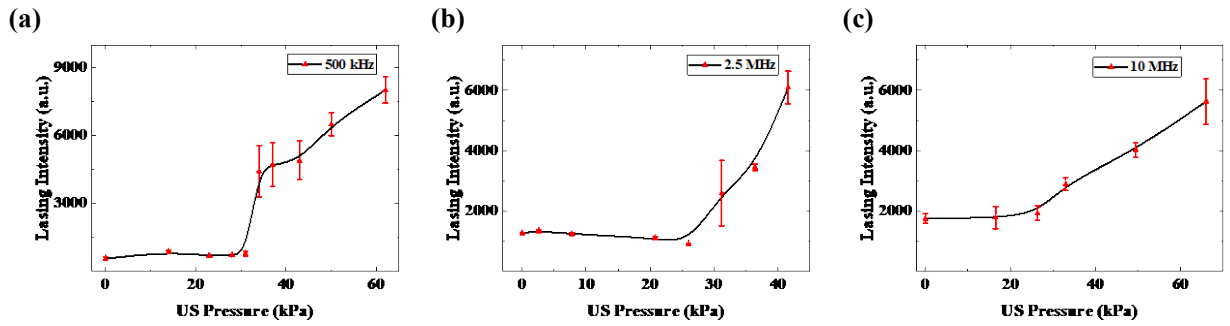

Figure 2.5 Lasing enhancement with different ultrasound frequencies. (a)-(c), Lasing intensity as a function of US pressure for US frequency of 500 kHz, 2.5 MHz, and 10 MHz, respectively. All lasing intensities were extracted from the spectra collected under a pump energy density of 40 μJ/mm^2 and an integration time of 1 s. Error bars were obtained with 5 measurements. Three different 50 μm droplet lasers were investigated respectively in (a)-(c).[41] Adapted with permission. Copyright 2019, American Chemical Society.

The phenomena observed above, including the lasing intensity enhancement and the ultrasound threshold behavior, can be understood in the framework of directional emission from an asymmetric resonator cavity (ARC) [74-78]. In the absence of ultrasound, the droplet maintains a nearly perfect spherical shape and the lasing output is weak and isotropic. In the focused ultrasound field, the droplet is steadily deformed to become ellipsoidal by the second-order acoustic radiation force [72]. The quantitative estimation of the acoustic radiation force and the corresponding deformation of the droplet are included in Section 2.2. With a relatively low acoustic pressure (and hence a low acoustic radiation force), the deformation of the droplet is insignificant, and the weak, isotropic lasing emission is preserved. With the increased acoustic pressure (and hence the increased acoustic radiation force), the smoothly deformed droplet breaks the spherical symmetry of the WGM cavity, and the ray dynamics becomes partially chaotic, leading to high power directional laser emission (or chaos-assisted tunneling). Such enhancement in the laser emission directionality, laser output, and laser output efficiency, as well as reduction in the lasing threshold, were previously observed in oscillatory droplets falling in the air and solid disks fabricated on a chip[74, 79, 80], but have never been studied under the influence of

ultrasound. Usually, due to the relatively large refractive index contrast between those WGM cavities and the surrounding media, a relatively large deformation threshold (e.g., 5%) is needed to have directional emission. However, in our case, the refractive index contrast between the oil and water is only 1.1, and therefore, directional emission can be achieved with a smaller deformation. Based on the ultrasound threshold in Figure 2.4 and the theoretical analysis in Figure 2.2, we estimated that even only 0.1% deformation is sufficient to cause the directional emission. For biomedical applications, a low deformation threshold is desirable since low US intensity is needed to modulate droplet lasers.

To further confirm the mechanism of the enhanced lasing emission described above, we conducted two groups of control experiments. First, we studied the fluorescence intensity from the microdroplet of a similar size (~50 μm in diameter) doped with the same concentration of BODIPY (Figure 2.6). The difference between lasing emission collection and fluorescence emission measurements is the pump energy density. Here we used a lower pump energy density (below the lasing threshold, 5 $\mu J/mm^2$). In this case, only the spontaneous fluorescence emission can be observed. As a result, no difference in fluorescence intensity was observed between the strong ultrasound pressure (50 kPa at 500 kHz) and no US pressure (0 kPa), indicating that US does not affect the fluorescence efficiency of the dye molecules.

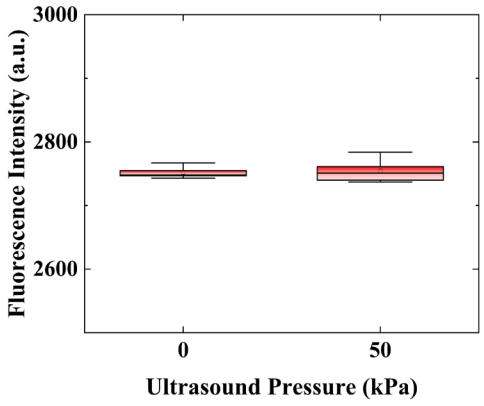

Figure 2.6 Fluorescence intensity of an oil droplet laser doped with BODIPY with and without applying ultrasound pressure. All data were obtained under the same pump energy density of 5 μJ/mm^2 with a repetition rate of 20 Hz. Error bars were obtained with 5 measurements. [41] Adapted with permission. Copyright 2019, American Chemical Society.

Second, in Figure 2.7, we performed the same US enhanced lasing emission on 10 μm diameter polystyrene beads doped with a fluorescence dye, FITC. When the beads were pumped at 485 nm and 30 μJ/mm^2, lasing emission from the beads was clearly observed. However, even in the presence of a strong ultrasound pressure (50 kPa at 500 kHz), the lasing intensity remains virtually unchanged due to the high Young's modulus (3 GPa) of polystyrene and hence the negligible bead deformation.

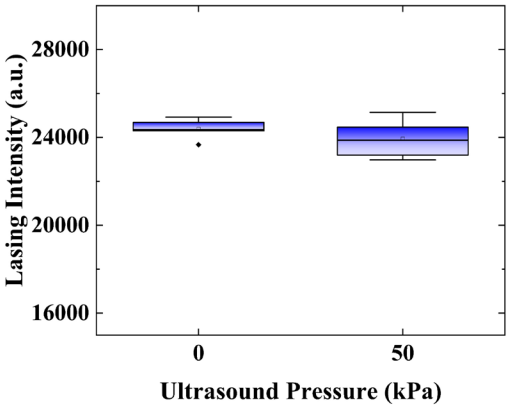

Figure 2.7 Lasing intensity of a polystyrene bead doped with FITC without and with applying ultrasound pressure (500 kHz, 50 kPa). All data were obtained under the same pump energy density of 40 μJ/mm2 with a repetition rate of 20 Hz. Error bars were obtained with 5 measurements.[41] Adapted with permission. Copyright 2019, American Chemical Society.

2.4.2 Control Droplet Laser Emission by Ultrasound

Figure 2.8(a) shows the capability to non-invasively modulate the microdroplet laser emission by changing the US intensity. In particular, a 500 kHz focused US transducer was used to produce multiple cycles of pressure (0→12 kPa→60 kPa→12 kPa→0). Every time when a strong ultrasound pressure of 60 kPa was applied, a significant lasing enhancement of 4-6-fold could be observed compared to the laser emission at ultrasound pressure of 0 and 12 kPa. In

addition to the ultrasound intensity, the laser emission can also be controlled by the ultrasound duty cycle. Figure 2.8(b) presents the laser emission intensity with 0%, 24%, and 48% duty cycle under the same ultrasound pressure (50 kPa at 500 kHz). With the increased duty cycle, the lasing intensity increases linearly. Finally, we demonstrate the laser emission enhancement by short ultrasound bursts. A series of ultrasound bursts (500 kHz, 60 kPa, 60 ms burst duration) was utilized to trigger the enhanced microdroplet laser emission with a repetition frequency of 0.5 Hz. The laser emission was collected with an exposure time of 0.5 s. From the synchronized ultrasound pressure and laser intensity curves in Figure 2.8(c), it can be seen that the lasing intensity follows the ultrasound burst at the same repetition frequency.

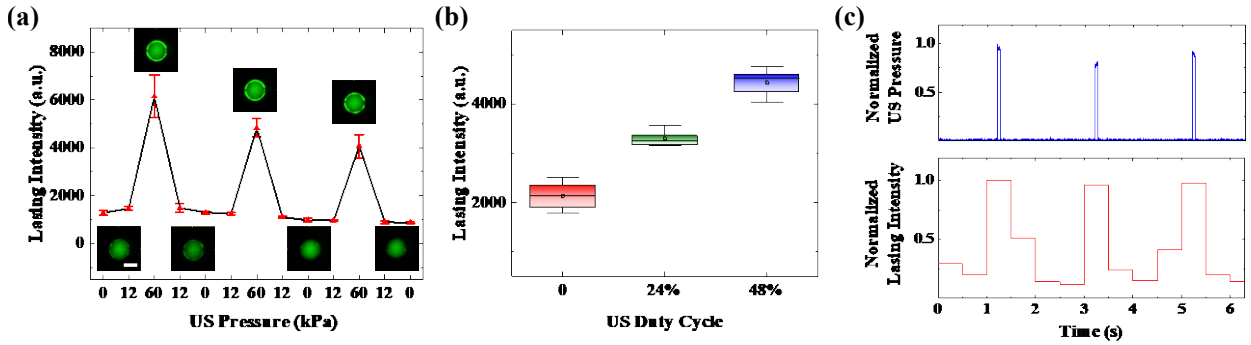

Figure 2.8 Modulating laser by ultrasound (US). (a) Observation of laser intensities over multiple 500 kHz US pressure cycles (0→12 kPa→60 kPa→12 kPa→0). Insets: CCD images of the oil droplet at ground states and lasing enhancement states. The overall downward trend of lasing intensity was caused by the photobleaching effect. Error bars were obtained with 5 measurements. Scale bar: 25 μm. (b) Lasing intensity modulated by the duty cycle of 500 kHz US at 50 kPa. When the US duty cycle increases, lasing output increases accordingly. All lasing intensities in (a) and (b) were extracted from the spectra collected under a pump energy density of 40 μJ/mm^2 and an integration time of 1 s. (c) Lasing emission enhanced by short US bursts (500 kHz, 60 kPa, 60 ms burst duration, 0.5 Hz repetition frequency). The top (blue) curve is US driving signal acquired by an oscilloscope. The bottom (red) curve is extracted from a series of spectra under a pump energy density of 40 μJ/mm^2 and an integration time of 0.5 s. The repetition rate of the pump is 20 Hz, which ensures that there is at least one pump during the US burst.[41] Adapted with permission. Copyright 2019, American Chemical Society.

2.4.3 Temporal Modulation of Droplet Laser Emission by Ultrasound

The ability to temporally modulate the laser emission is the key to significantly improving the SNR. This becomes even more critical when applying the microdroplet laser for sensing and imaging in deep tissues. First, a series of short US bursts (500 kHz, 60 kPa, 30 ms burst duration) with a repetition frequency of 8 Hz was applied to the microdroplet laser. A CCD camera was used to continuously record the laser output intensity. The pump laser was set at 40 Hz with an energy density of 50 $\mu J/mm^2$ to match the image sampling rate of 40 fps. Figure 2.9(a) presents the raw intensity curve as a function of time extracted from the recorded images. Figure 2.9(b) shows the frequency domain analysis of the signal in Figure 2.9(a) with a bandpass (6-10 Hz) FFT digital filter. A distinct 8 Hz component in the frequency spectrum is observed corresponding to the 8 Hz ultrasound bursts. Then, a series of short ultrasound bursts (500 kHz, 60 kPa, 15 ms burst duration) with a repetition frequency of 20 Hz was applied to the microdroplet laser. Similarly, the pump laser was set at 80 Hz with an energy density of 50 $\mu J/mm^2$ to match the image sampling rate of 80 fps. Figure 2.9(c) presents the raw intensity curve as a function of time extracted from the recorded images. By applying a bandpass FFT digital filter (15-25 Hz), a 20 Hz modulated frequency component in laser output can be seen in Figure 2.9(d) with an SNR of approximately 30. Due to the limitation of our experiment instruments (OPO laser reptation rate and CCD frame per seconds), the maximum temporal modulation frequency we achieved is 20 Hz. By upgrading the experiment system, we can explore the maximum modulation frequency with the droplet lasers.

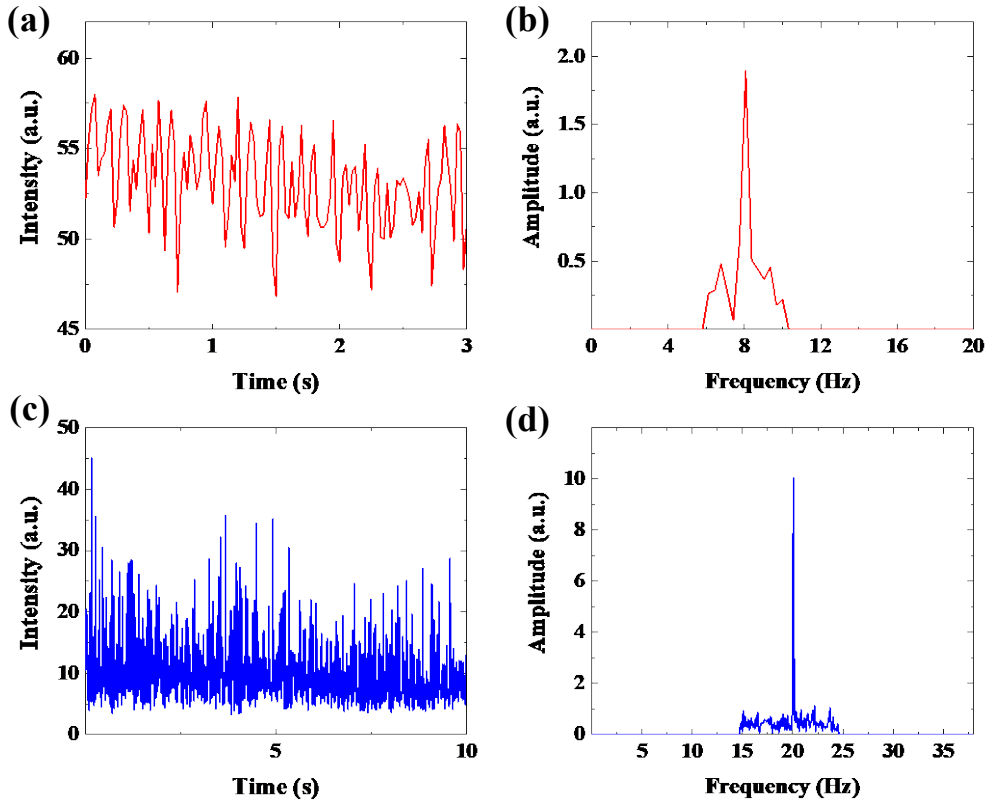

Figure 2.9 Lasing emission modulated temporally by ultrasound (US). (a) Lasing intensity recorded in the time domain modulated by US bursts (500 kHz, 60 kPa, 30 ms burst duration, 8 Hz repetition frequency). The lasing intensity under a pump energy density of 50 μJ/mm^2 with a pulse repetition rate of 40 Hz was recorded from a CCD with 40 fps. (b) Frequency spectrum when applying FFT to the lasing intensity in (a) with a bandpass filter (6-8 Hz). A peak at the 8-Hz modulation frequency can be noted. (c) Lasing intensity recorded in the time domain modulated by US bursts (500 kHz, 60 kPa, 15 ms burst duration, 20 Hz repetition frequency). The lasing intensity under a pump energy density of 50 μJ/mm^2 with a pulse repetition rate of 80 Hz was recorded from a CCD with 80 fps. (d) Frequency spectrum when applying FFT to the lasing intensity in (c) with a bandpass filter (15-25 Hz). There is a notable 20 Hz modulated component in the spectrum.[41] Adapted with permission. Copyright 2019, American Chemical Society.

2.4.4 Ultrasound Modulated Oil Droplet Lasers in Blood

human whole blood are: First, blood has a stronger absorption than water the signal could be reduced. Second, blood has a higher viscosity than water so that the deformation we have could be different from that in water. In the experiments, initially, a continuous ultrasound pressure (40 kPa at 500 kHz) was focused on the blood vessel phantom, and enhanced lasing intensity was observed. The enhancement was reversible after turning the ultrasound off (Figure 2.10 (b)). This result verifies that the ultrasound lasing enhancement persists even when the droplets are surrounded by whole blood. Next, a series of short ultrasound bursts (500 kHz, 60 kPa, 60 ms burst duration) at 4 Hz repetition frequency was used to modulate the droplet laser. The lasing emission was collected by a CCD camera with 20 fps, as the result shown in Figure 2.10(c). After applying a bandpass FFT digital filter of 2-6 Hz, the modulation component at 4 Hz can be easily extracted with a high SNR of 25, as shown in Figure 2.10(c).

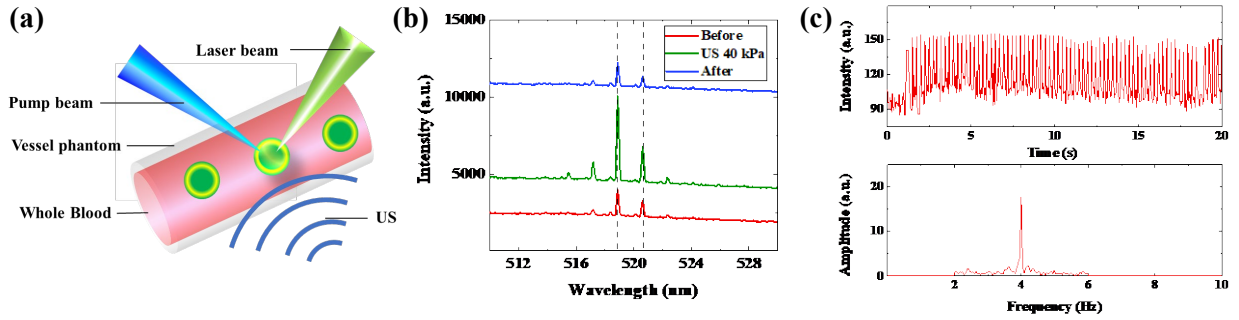

Figure 2.10 Ultrasound modulated oil droplet lasers in blood. (a) Schematic of the experiment. (b) Lasing spectra of an oil droplet laser mixed with human whole blood and loaded into a capillary before, during, and after applying US pressure (40 kPa at 500 kHz). All curves were obtained under the same pump energy density of 50 μJ/mm^2 with a pulse repetition rate of 20 Hz. Curves are vertically shifted for clarity. (c) (Top) Lasing intensity collected from the whole blood in the time domain with US bursts (500 kHz, 60 kPa, 60 ms burst duration, 4 Hz repetition frequency). The lasing intensity was recorded from a CCD with 20 fps under a pump energy density of 70 μJ/mm^2 with a pulse repetition rate of 20 Hz. (Bottom) Corresponding frequency spectrum of the lasing intensity processed with a bandpass FFT filter (2-6 Hz). There is a notable 4 Hz component in the spectrum.[41] Adapted with permission. Copyright 2019, American Chemical Society.

2.5 Summary

In this study, we demonstrated the first "ultrasound modulated droplet laser" utilizing biocompatible microdroplet lasers and low intensity focused ultrasound transducers. First of all, lasing intensity enhancement was observed and investigated under various ultrasound frequencies and continuous pressure. Besides, we explored modulating droplet laser output with ultrasound duty cycle and short bursts. Moreover, the temporal modulation of laser output was achieved with a series of ultrasound short bursts at a specific frequency and frequency domain analysis. In addition, we validated that the ultrasound modulated droplet lasers could work well in biological samples such as vessels containing human whole blood. In all the experiments, the pump energy density was orders of magnitude lower than the level that may cause damage to cells or tissues, demonstrating that the US modulated droplet lasers could be developed into non-invasive imaging and sensing technologies.

Our study provides a possible solution to break the optical diffusion limit and significantly improves the spatial resolution, sensitivity, and imaging depth, which may overcome the longstanding drawbacks of conventional fluorescence techniques. By combining the advantages of ultrasound imaging, including deep tissue penetration and high spatial resolution with the advantages of laser emission, including high SNR, imaging contrast, and sensitivity, the ultrasound modulated droplet laser presented in this work opens a door to a new generation of laser emission microscopy for imaging and sensing in deep biological tissues. Below we discuss several scenarios and possible methods to exploit ultrasound modulated droplet lasers. By conjugating the droplet lasers with targeted cells, imaging and tracking of cellular dynamics could be achieved *in vivo* in subsurface tissues. Without targeting any biological entities, the droplet lasers injected into the circulatory system such as blood vessels can also work as blood pool agents to achieve high-

resolution laser emission imaging of the vasculature, as well as flow dynamics in biological samples. Besides potential contributions to biology and medicine, the method described in this work provides a new platform to tune the cavity shape and size remotely, non-invasively, and continuously by ultrasound, which is important for fundamental research and the development of novel photonic devices.

However, there are still many potential challenges for this technique to be adapted to preclinical and clinical applications: First, currently, to maintain a resonant cavity with a good Q-factor to support lasing emission, the microcavity size is relatively large (~30 μm) That hinders this technology to be applied in cell tracking. By using other liquid material with high refractive index will help reduce the microcavity size while maintains the lasing performance. Second, the control of ultrasound modulation signal should be optimized to avoid the interference in tracking process. Potential upgrades that may help are increasing ultrasound frequency to reduce the focal spot radius and reducing the burst period while increasing ultrasound amplitude.

Chapter 3 In Vivo Single Immune Cell Tracking Using Nanowires with the Multimodality Optical Imaging System

3.1 Overview of Single Cell Tracking Technologies

In vivo and non-invasively single cell tracking is an important tool for physiological and pathological research and clinical diagnostic [81-83]. For example, understanding the migration of immune cells could facilitate the evaluation of immune therapies. By monitoring the dynamics of stem therapies, physicians could keep the treatment on the right track [82]. Therefore, researchers have focused on this field and developed many tools to tackle this technically challenging problem. Here we briefly overview some technologies of *in vivo* single cell tracking for the reader's reference.

3.1.1 CT/PET/MRI Based In Vivo Single Cell Tracking

The idea of CT/PET/MRI based *in vivo* single cell tracking is mainly about some radiology contrast agents to label cells [81]. Researchers have utilized mesoporous silica nanoparticles to concentrate radionuclide to label cancer cells and then imaged the movement of cancer cells in the animal body with a PET-CT system [32]. The movement trajectories of the labeled cancer cells can be demonstrated over time. Similar ideas have been explored in MRI by introducing magnetically visible nanoparticles into the tracked cells [81]. The advantages of the CT/PET/MRI-based *in vivo* single cell tracking technologies are: first, they could provide good imaging depth to visualize the relative spatial and temporal locations of labeled cells within the surrounding tissues and overall animal bodies. That supports the understanding of injected cells from a high-level perspective. Second, most radiology imaging modalities are very mature and developed. Here,

single cell tracking technologies usually rely on novel contrast agents. Thus, the efforts of system upgrades are minimal.

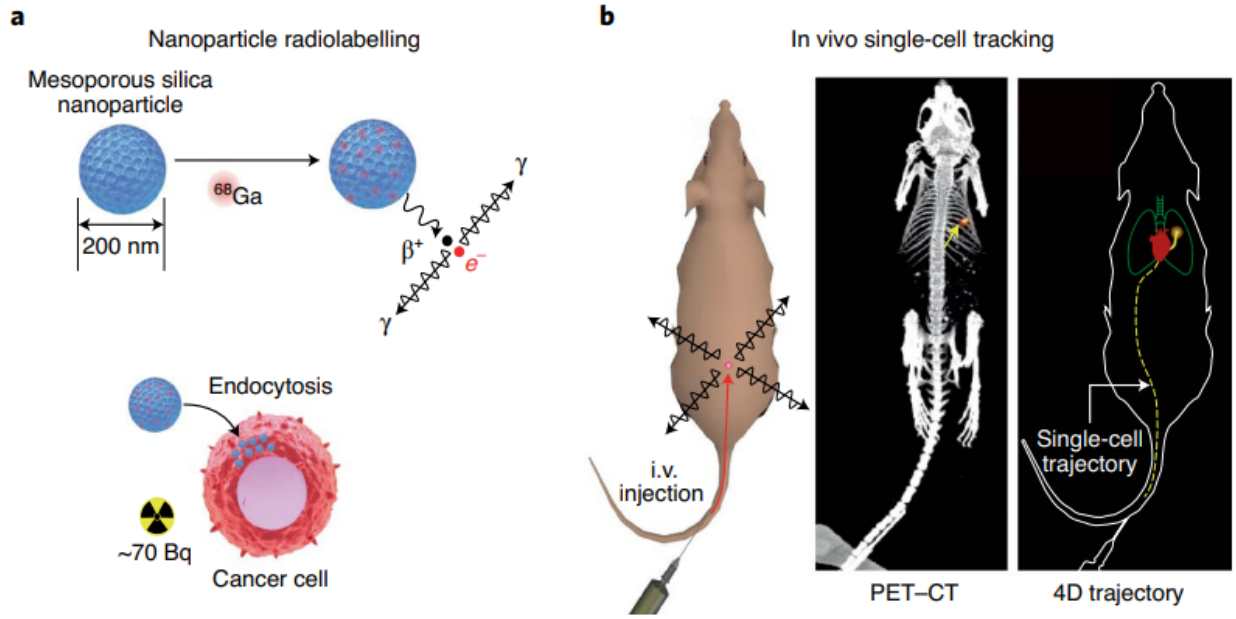

The disadvantages of these single cell tracking technologies are: first, the contrast agents used in these technologies are homogenous. It is not possible to identify different tracked cells. Thus, to achieve single cell tracking, the concentration of labeled cells should be diluted to avoid interference from other cells which could bring randomness in the study. And it is tedious to do multiple experiments to get statistical results. Second, although these modalities provide satisfying imaging depth and imaging resolution, for specific clinical situation, higher imaging resolution is needed to understand the interaction between cells and microscopic structures in tissues. Thirdly, these technologies are radiological imaging modalities. Frequently monitoring the positions of cells would bring concerns about radiation exposure when these technologies are applied to humans.

3.1.2 Optical Imaging Based In Vivo Single Cell Tracking

Optical imaging is also an ideal method to track single cells. It could provide satisfying imaging resolution while maintaining a low radiation exposure. Fluorescence labeling is the most common method applied in single cell tracking. It could provide additional contrast and multiple colors to label different groups of cells [85, 86]. Many optical contrast agents have been introduced in Section 1.3. Here in Figure 3.2, researchers have demonstrated cell tracking in animal models to understand the interaction with immune cells and cancer cells.

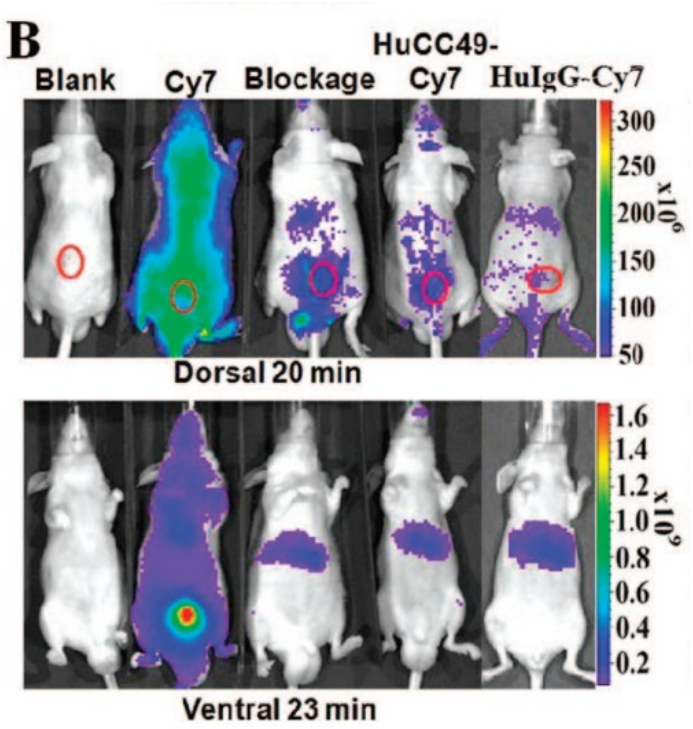

The biggest challenge for optical imaging-based cell tracking is the imaging depth. Owing to the omnipresent scattering of tissue, the signal intensity and resolution will drop significantly through the tissue layer. Therefore, optical-based tracking technologies are usually applied in some specific regions where it outperforms radiology-based images.

3.2 Motivation for *In Vivo* Single Cell Tracking Using Nanowire Lasers with Multimodality Optical Imaging System

Emerging cell-based therapies such as stem cell therapy and immunotherapy have drawn wide attention as novel therapeutics in medical research and clinical practice [88-91]. To evaluate the efficacy of the treatment, the determination of *in vivo* cell distribution, migration, and development is highly desired. However, the current assessment of therapeutics is mostly based on indirect methods [92, 93], such as evaluating the efficiency of treatment by the size change of the tumor or the recovery of the target area. Therefore, the technology to directly monitor the distribution and migration of implanted living cells *in vivo* is important for both the application of cell-based therapies and the exploration of mechanisms in basic biological research [82].

Optical coherence tomography (OCT) is a clinically available imaging technology with ultrahigh-resolution (~3.8 μm) and excellent imaging depth (~2 mm) [94-96]. This technology also has great potential for *in vivo* cellular imaging studies, especially for cell dynamic research [97-99]. Due to the minimal scattering difference between cells and surrounding tissue layers, the original OCT imaging contrast of cell dynamics is poor. Therefore, contrast agents such as gold nanoparticles [26, 100-103] and polymer microspheres [104] with strong scattering properties that can be internalized by targeted cells have been employed to improve imaging visibility. However, in most scenarios, both the contrast agent distribution and their optical properties in labeled cells are homogenous. Consequently, current OCT systems are only capable of observing the overall change in the distribution of the entire cell population [105]. Precise tracking of individual cells remains technically challenging with those conventional contrast agents.

Fluorescence labeling is a widely used technique to differentiate biological targets and monitor cell migrations [19, 106-108]. Multi-spectral fluorescence labels were also explored along

with the intensity-based grayscale OCT imaging to provide distinguishable information to simultaneously track different cell groups [108]. However, as a result of the broad emission spectra of fluorophores, the number of different labels involved in multi-spectral fluorescence imaging is limited [106, 108]. Geometrically encoded fluorescent DNA barcodes utilized the positions of the fluorophores on a DNA nanorod to provide over 200 distinct labels [19]. However, due to the scattering environment in tissue, the submicron resolution in fluorescent barcodes has significantly deteriorated. Therefore, it is difficult to employ this technique *in vivo* studies.

In contrast, laser emission-based imaging has recently emerged as a novel technology in biomedical research. Notably, the microcavity lasers have shown to be promising intracellular labels due to their small sizes, high emission intensities, rich emission spectra, and narrow linewidths [5, 10-12, 109-111]. It has been shown that those microcavity lasers can be internalized by cells to either detect microenvironmental changes inside cells [5, 10] or track individual cells [12, 111]. Nonetheless, the application of microcavity laser cell tracking is hindered from *in vivo* studies due to the following reasons. First, the lasing emission of microcavity lasers is blurred because of the omnipresent scattering tissue. Consequently, the position of the microcavity lasers cannot be precisely determined. Second, the tracking based on the lasing emission provides only 2D images, while 3D information, albeit critical to locating spatial positions of cells, is lost.

In this study, we developed an integrated OCT and fluorescence microscopy (FM) dual-modality cell tracking system utilizing cadmium sulfide (CdS) nanowire lasers to track the 3D migration of individual cells *in vivo*. We first proved that the CdS nanowire lasers can be internalized by macrophages and can enhance the OCT signal by up to 25 dB. Then, the distinct lasing emission spectra of nanowire lasers were acquired and used as unique identifiers to track the migration trajectories of cells on fibrin hydrogel surfaces. Finally, we demonstrated the 3D

tracking of those nanowire lasers and hence the migration of individual cells in the subretinal layer of living New Zealand rabbits with the dual-modal imaging system.

3.3 Experimental Setup and Methods

3.3.1 Experimental Setup

In this study, an OCT and FM dual-modality imaging system combined with the spectrometer was developed to monitor the target cells *in vivo* (Figure 3.3). In brief, the SD-OCT system was adapted from a commercially available system from Thorlabs (Ganymede-II-HR, Thorlabs, Newton, NJ) by implementing an ocular lens (OL) after the scan lens. For FM and laser excitation, an OPO (NT-242, Ekspla, Vilnius, Lithuania, tunable wavelength from 405 to 2600 nm, pulse duration 3–6 ns) was used as the illumination source. The fluorescence and laser emission were collected from the backward optical path of telescope configuration, reflected by a dichroic mirror (FF496-SDI01, Semrock, Lake Forest, IL), and separated by a fiber optic coupler (TN532R2F1, Thorlabs, Newton, NJ) after passing through a band-pass filter (MF 530-43, CWL = 530 nm, BW = 43 nm, Thorlabs, Newton, NJ) into fluorescence and laser emission channels. The fluorescence signal was detected by an avalanche photodiode (APD) (APD 110A, Thorlabs, Newton, NJ) and digitized by the DAQ card (PX1500–4, Signatec Inc, Newport Beach, CA, sampling rate 500 MHz). The laser emission spectra were collected by the spectrometer with an integration time of 0.5 s (HR4000, Ocean Optics Inc, Dunedin, FL). The OPO laser, the OCT scan header, and the DAQ card were synchronized through a delay generator and a clock switch circuit. The light from different imaging modalities was coaxially aligned to ensure the co-registration of the dual-modality images. The lateral and axial resolution of SD-OCT were previously quantified to be 3.8 μm and 4.0 μm, respectively [112]. In this study, the laser wavelength of 485 nm and the laser energy of 150 nJ before the eye were used.

Here I want to emphasize the role that FM plays in this OCT and FM dual-modality imaging system. First, FM provides cross-validation of cells' spatial locations in OCT images. Second, it helps OCT remove unwanted defects. In our data processing, we used OCT signal thresholding to extract the cell positions. Although the OCT signal is strong, some tissues of the animal exhibit strong scattering and thus appear in the OCT image as defects. The 2D information provided by FM about the nanowire locations allows us to easily filter out those defects. Third, it assists in laser emission collection. Currently, it takes approximately 2-3 seconds to collect nanowire laser spectrum from one location. It would be very time-consuming and impractical to scan the entire tissue. FM helps quickly locate the nanowires within the field of view so that the pump light can be delivered to excite the nanowire and the corresponding laser emission can subsequently be collected.

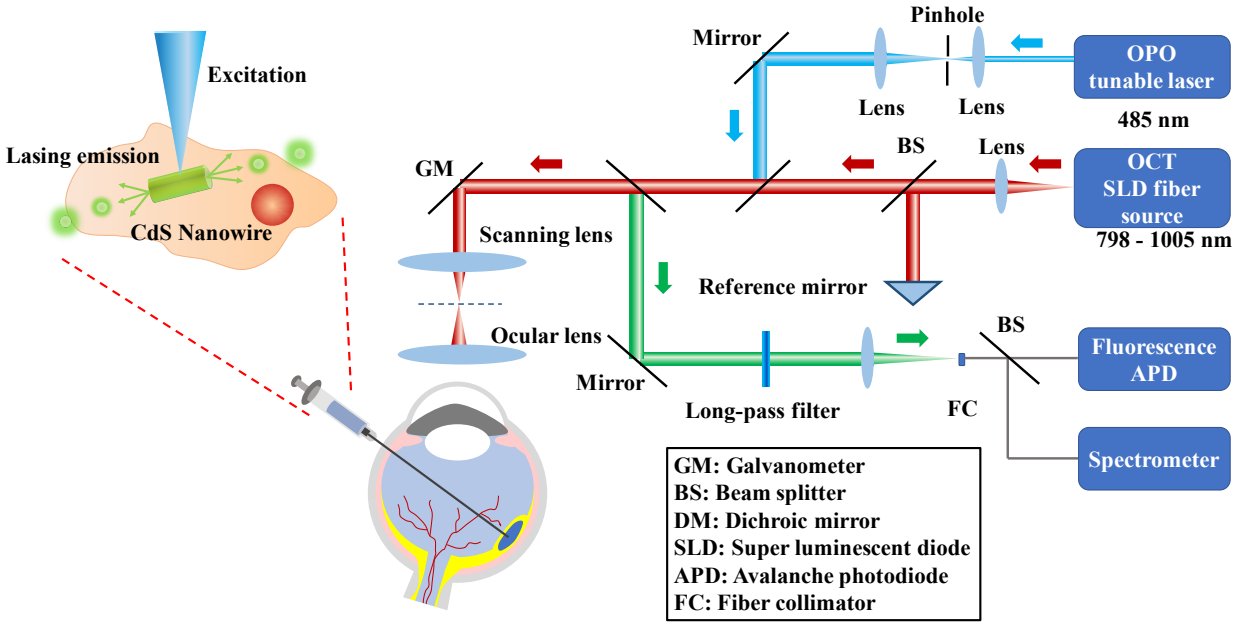

Figure 3.3 Schematic of the OCT and fluorescence/laser emission dual-modality imaging system and illustration of a CdS nanowire microlaser internalized by a cell.[42]

3.3.2 Nanowire Lasers Preparation

The method of synthesizing CdS nanowires is described in detail in the previous publications [10, 113, 114]. Briefly, the nanowires were synthesized by an Au-nanocluster catalyzed vapor-liquid-solid method. Inside a horizontal quartz tube mounted in a single zone furnace, CdS powders (Sigma Aldrich, St. Louis, MO, 99.99% purity) were placed on an alumina boat in the center of the heating zone as the source. Silicon (Si) wafers (Ql Electronics Inc., Ningbo, China) covered with a 10 nm thick Au film by sputtering were located downstream from CdS powders near the end of the heating zone. A high purity nitrogen gas flow with a flow rate of 700 SCCM was introduced into the system to purge oxygen out. After 1 hour of gas flow cleaning, the furnace was heated from room temperature to 850 °C at 500 mbar pressure and kept for an extra hour. Meanwhile, a 155 SCCM nitrogen gas flow was maintained in the whole heating process to transport the evaporated CdS vapor to the Au-catalyzed Si substrates to initialize nanowire growth. After growing for 1 hour, yellowish nanowire products could be found on the Si substrate.

3.3.3 Cell Preparation

The isolation of bone morrow-derived macrophages was conducted as previously described [115]. Mice were first sacrificed by cervical dislocation. Then, the abdomen and hind legs were sterilized with 70 % ethanol. After making an incision in the midline of the abdomen, the hind legs were exposed, and the bones were cut at both ends. Later on, the bones were crushed in a mortar with 5 mL of lymphocyte medium supplemented with 20 mM HEPES. The bone marrow cells were pipetted up and down to separate the cells into a single-cell suspension for them to pass through a cell strainer. The cells were transferred into a bone morrow macrophage medium and induced to differentiate in a humidified incubator with 5% CO_2 at 37 °C. Macrophage media consisted of DMEM containing 1% penicillin/streptomycin, L-glutamine, 10% fetal bovine serum,

and L929 murine fibroblast conditioned media (All supplies were from Thermo Fisher, Waltham, MA).

3.3.4 In Vitro Experiments

For biological use, the nanowire-carrying wafer was immersed in ethanol and sonicated in an ultrasonic cleaner for 10 min to separate the nanowires from the substrate. After removal of the Si substrate and centrifuging of the remaining solution, the nanowires were separated from ethanol, then re-dispersed in phosphate-buffered saline (PBS) solution, and finally sterilized under a UV lamp for about 1 hour in a laminar flow hood before culturing with the cells.

To mimic the *in vivo* subretinal layer environment, macrophages were seeded on a layer of fibrin hydrogel. Fibrin hydrogel coated glass coverslips were made by adding 100 µl of fibrin precursor solution (5 mg/ml fibrinogen (Sigma Aldrich, St. Louis, MO) and 10 units/ml thrombin (Sigma Aldrich) in 1X PBS) onto 18 mm diameter glass coverslips and allowed to crosslink for 30 minutes. The nanowire-carrying macrophages were then seeded onto 5 mg/ml fibrin hydrogel coated coverslips and allowed to attach and spread over 24 hours. Next, 150 µL PBS solution containing nanowires was added to overlying cell media (2 mL), and cells were allowed to internalize nanowires over 24 hours. Then samples were rinsed with media 3x to ensure that free-floating nanowires were removed prior to longitudinal imaging.

To verify that the nanowires were internalized by macrophages, confocal images were acquired on a confocal microscope (LSM800, Zeiss, Jena, Germany). Samples were first fixed with 4% paraformaldehyde. Then 4′,6-diamidino-2-phenylindole (DAPI) (1 µg/ml, Sigma Aldrich, St. Louis, MO) and Phalloidin 555 (Life Technologies, Carlsbad, CA) were used to visualize cell nuclei and F-actin, respectively.

3.3.5 Animal Preparation

All animal procedures adhered to the ARVO (The Association for Research in Vision and Ophthalmology) Statement for the Use of Animals in Ophthalmic and Vision Research and were approved by the Institutional Animal Care & Use Committee (IACUC) of the University of Michigan (Protocol PRO00008566, Photoacoustic & Molecular Imaging of the Eye, PI: Y. Paulus). Rabbits were anesthetized with a mixture of Ketamine (40 mg/kg) and Xylazine (5 mg/kg) by intramuscular injection. A vaporized isoflurane anesthetic (1 L/min oxygen and 0.75% isoflurane) (SurgiVet, MN, USA) maintained anesthesia during the *in vivo* experiments. Pupillary dilation was achieved by one drop each of 1% tropicamide and 2.5% phenylephrine hydrochloride. Topical tetracaine 0.5% was instilled before treatment for topical anesthesia. Rabbit vital signs were monitored before and throughout the procedures, including mucous membrane color, temperature, heart rate, respiratory rate, and oxygen saturation using a pulse oximeter (V8400D Capnograph & SpO2 Digital Pulse Oximetry, Smiths Medical, MN, USA).

3.3.6 In vivo Experiments

To prepare for the subretinal injection, macrophages cultured with nanowires were collected by adding Accutase for 10 min at room temperature and enriched by centrifuging at 500 rcf for 4 min. The subretinal injection was performed via a sterile technique. The conjunctiva was cleaned with 5% povidone-iodine. A 3-mm inferotemporal conjunctival peritomy was performed in the eye using Westcott scissors and micro-forceps. After a marker was used to measure a distance of 3.5 mm posterior to the corneal limbus, a 30-gauge 0.5-inch needle was inserted at about the 8:00 to 8:30 position with care to avoid the ciliary vasculature and extraocular muscles. The OCT system was used for real-time guidance and to assist in confirming the injection depth by providing the anatomy of the injected retinal layers at 11 frames per second. A blunt 30-gauge needle (Hamilton, Reno, NV) attached to a 50 μL Hamilton syringe (Hamilton, Reno, NV) was

inserted through the 30-gauge 0.5-inch needle inserted site into the vitreous cavity, then introduced into the subretinal space about 0.5–1 optic disc diameter inferior to the retinal vessels, to inject 20μL of macrophage-enriched solution. When the needle was in contact with the RPE hyper-reflective layer, it was stopped and maintained its position before the syringe was pushed. The injection resulted in a localized subretinal fluid. During experiments, eyewash (Altaire Pharmaceuticals, Inc., Aquebogue, NY) was applied to the rabbit corneal surface every 2 min to prevent corneal surface keratopathy. The rabbit fundus was first imaged using a fundus camera (TRC 50EX, Topcon Corporation, Tokyo, Japan). After finishing the fundus camera imaging, the rabbits were transferred to the platform of the system and adjusted to position one eye under the ophthalmic lens. The head and body of the rabbit were placed on two custom-made stabilization platforms, which were used to minimize breathing and other motion artifacts. A water-circulation blanket (TP-700, Stryker Corporation, Kalamazoo, MI) was used to maintain the body temperature of the rabbits. The eyelid was retracted with a pediatric Barraquer wire speculum. The integrated charge-coupled device (CCD) camera was used to visualize the region of interest, and the reference arm was adjusted to optimize the image quality. During the experiments, the 3D OCT scanning was conducted first. Then, a 2D FM image was collected. Based on the FM images, an algorithm of contour detection and weighted center calculation was used to identify the locations of nanowires internalized by the macrophages and control the OPO laser beam to re-visit those locations to excite nanowire laser emission and collect corresponding lasing spectra. In addition, to visualize the distribution of nanowire-labeled macrophages and subretinal structures, 3D image reconstruction and processing were performed using the Amira software (FEI, Hillsboro, OR).

3.3.7 Nanowire Laser Internalization and Characterization

The CdS nanowire lasers were utilized to generate both OCT and FM signal, and unique spectral identifiers to differentiate each individual cell (see more details about nanowire fabrication in Section 3.3). Since the CdS nanowire lasers have a small size with 3-7 μm in length and ~200 nm in diameter, they can be easily internalized by macrophages without surface modification. To confirm macrophage nanowire internalization, confocal microscopy was utilized to visualize the 3D cellular structure. In the confocal microscopy image (Figure 3.4(a)), the cell cytoskeleton is stained blue and the nuclei are stained red. The CdS nanowire can be visualized by its own green fluorescence under 488 nm laser excitation. From the enlarged cross-section images (the top right and the bottom-right insets in Figure 3.4(a)) of the selected macrophage, the complete internalization of nanowires with the cell body is confirmed.

The lasing mechanism of the nanowire lasers can be explained as follows. Due to the high RI (n = 2.67) of a nanowire, the reflection at its two end-facets is high. Therefore, a nanowire can be regarded as a "Fabry–Perot" (F–P) cavity with a waveguide formed by the gain medium (CdS) and sandwiched between the two end-facets. The Q-factor of the CdS nanowire is estimated to be ~50 [113]. Despite the relatively low Q-factor, CdS can provide a high gain up to ~3000/cm at a carrier density of 1–3 × 10−19 /cm^3 [116] to compensate for the cavity loss and thus achieve lasing emission at a relatively low excitation. An exemplary lasing emission spectrum of a nanowire laser internalized by macrophage is given in Figure 3.4(b). The inset that plots the lasing output vs. pump energy curve shows a lasing threshold of about 2 μJ/mm2. Meanwhile, due to the high refractive index of CdS (~2.67) and the elongated shape, the nanowire itself produces strong scattering that can significantly enhance the signal in OCT imaging. A comparison study of the FM signal from the CdS nanowires were presented in Figure 3.5.

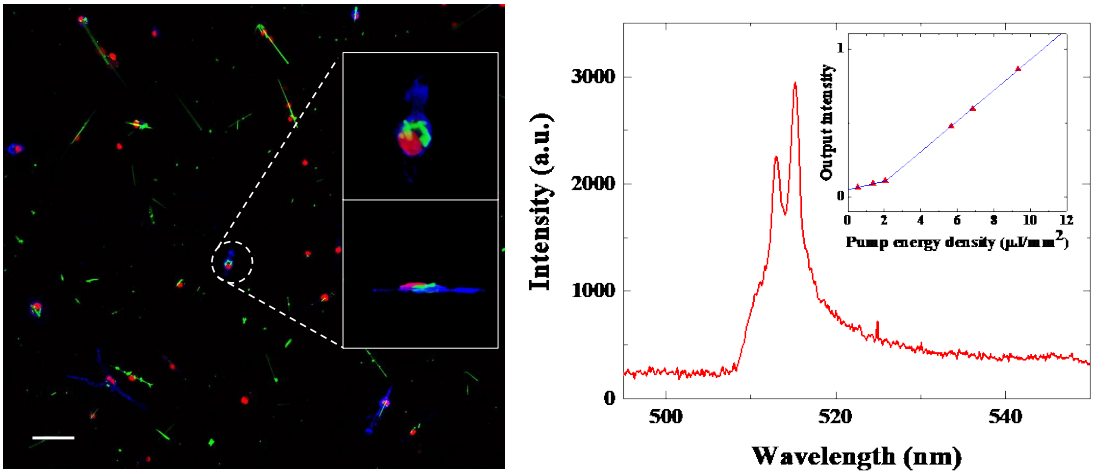

Figure 3.4 Nanowire internalized by macrophages and its lasing properties. (a) A confocal fluorescence image of nanowires internalized by macrophages. The cell cytoskeleton is stained blue and the nuclei are stained red. Upper and lower insets are enlarged top view and side view of a specific macrophage, respectively. (b) The lasing spectrum of a nanowire laser. Inset is the threshold curve. Scale bar: 50 μm. [42]

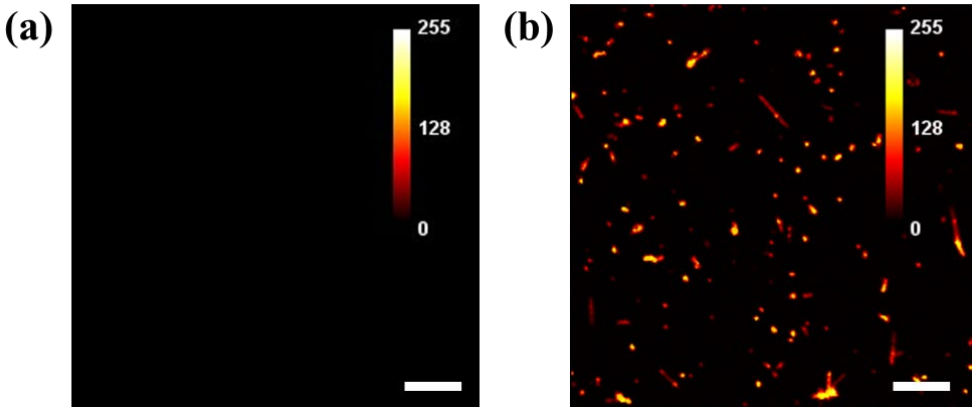

3.3.8 Estimation of the number of unique lasing spectra labels

The calculation of potential unique spectral labels from the CdS nanowire lasers. The lasing emission peaks range from 500 nm to 525 nm. Given our current spectrometer resolution of ~1 nm, the number of distinct spectral labels with 1 peak is:

$$N_1 = \binom{20}{1} = 20$$

Since there are also spectral labels with 2 lasing peaks, the number of potential distinct spectral labels are:

$$N_2 = \binom{20}{2} = 190$$

Similarly, the number of spectral labels with 3 peaks is:

$$N_1 = \binom{20}{3} = 1350$$

Because the spectral labels with more than 4 peaks rarely occur, the total number can be calculated as:

$$N_{total} = N_1 + N_2 + N_3 = 1350$$

3.4 Results and Discussions

3.4.1 In Vitro Cell Tracking with Nanowire Lasers

Cell tracking experiments were first conducted *in vitro* to verify feasibility. To mimic the *in vivo* tissue environment, macrophages were cultured on a layer of scattering hydrogel. The sterilized nanowires were added into the cell culture media of macrophages 24 hours before the experiments to ensure full internalization. Then, the macrophages were examined with our dual-modality imaging system. Figure 3.6(a) and (b) show the fluorescence image and the 2D X-Y plane OCT image from the same area, respectively. The distributions of the macrophages from the two imaging modalities match well, which confirms that the nanowires internalized by the macrophages can provide additional contrast in both OCT and FM imaging modalities. The lasing emission spectra were also collected from the nanowire lasers (Figure 3.6(c)). Four selected spectra were acquired from the four locations indicated by the yellow boxes in Figure 3.6(a) and (b). The distinct lasing emission spectra could be used as an identifier to differentiate each cell for individual cell tracking.

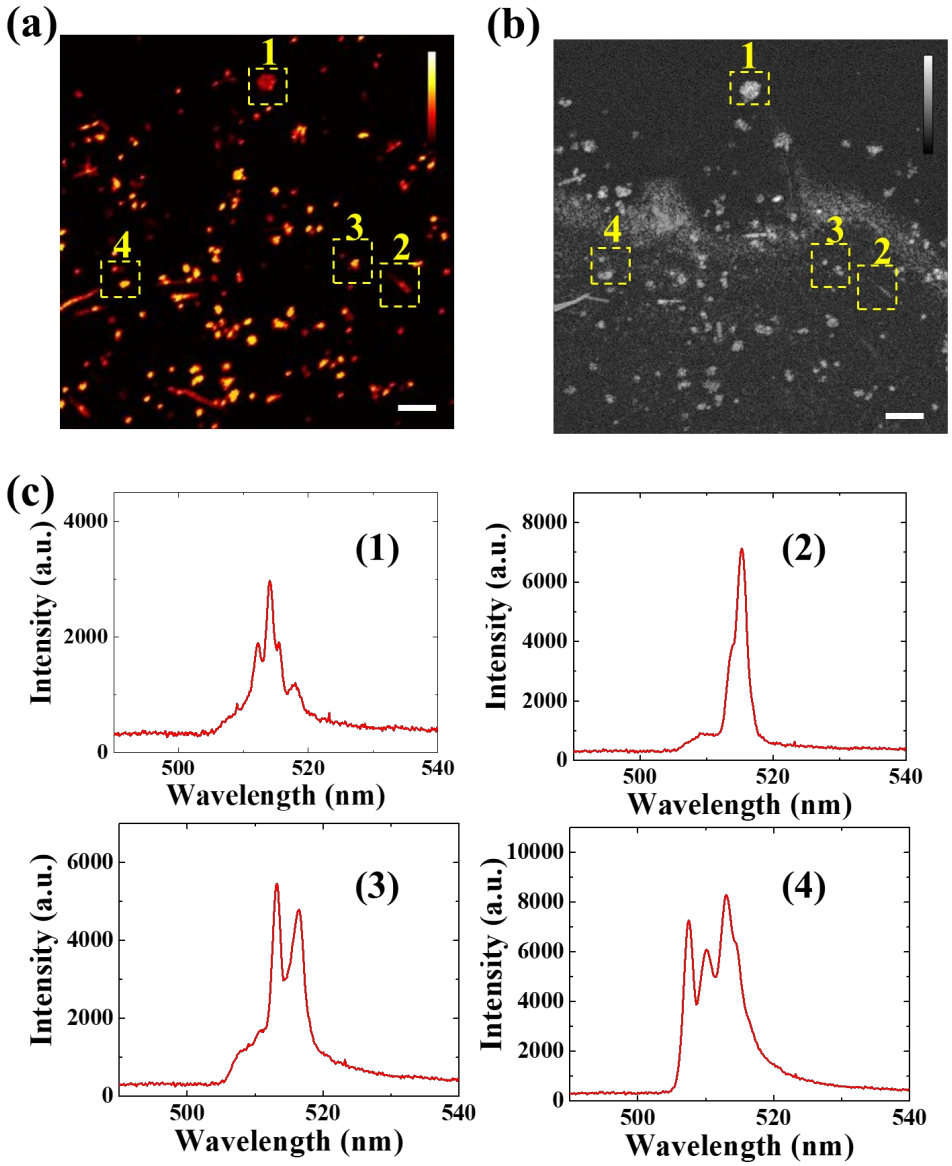

Figure 3.6 ***In vitro*** **dual-modality contrast enhancement of nanowire and lasing emission spectra.** (a) Fluorescence image of nanowire-labeled macrophages cultured on the hydrogel layer. Four macrophages are selected as tracking targets. (b) 2D X-Y plane OCT image of the same field of view in (a). The locations of the four macrophages labeled with 1-4 match well between (a) and (b). The nanowires provide additional imaging contrast in both OCT and FM. (c) Unique lasing spectra (1)-(4) were collected from the four selected macrophages in (a) and (b). Scale bar: 100 μm.[42]

After testing the imaging contrast and lasing emission inside the cells, we conducted the *in vitro* cell tracking experiments and acquired time-lapse images. Macrophages cultured on fibrin hydrogel were monitored successively every 8 hours for 24 hours in total. During imaging, we

used a marker on the fibrin hydrogel surfaces to retrieve the same field of view for each observation. Figure 3.7(a) shows the migration trajectories of three selected macrophages extracted from the FM images over time. For a clearer view, the trajectories are superimposed on top of each other. The inset on the right shows a series of enlarged views of one macrophage migrating in different time frames. The identities of tracked macrophages are verified by the lasing emission spectra of nanowire laser internalized by the macrophages. Figure 3.7(b) presents the lasing emission spectra collected from the same selected macrophages in Figure 3.7(a). Throughout the entire experiment, the lasing emission spectra from the same macrophages remained unchanged and distinguishable from each other. The OCT 3D images from multiple observations are aligned by matching the structural features of the hydrogel layer. Based on the identification information provided in Figure 3.7(b), the individual macrophage spatial location is extracted from the OCT 3D images via contrast thresholding to obtain the migration trajectories of selected macrophages in Figure 3.7(c).

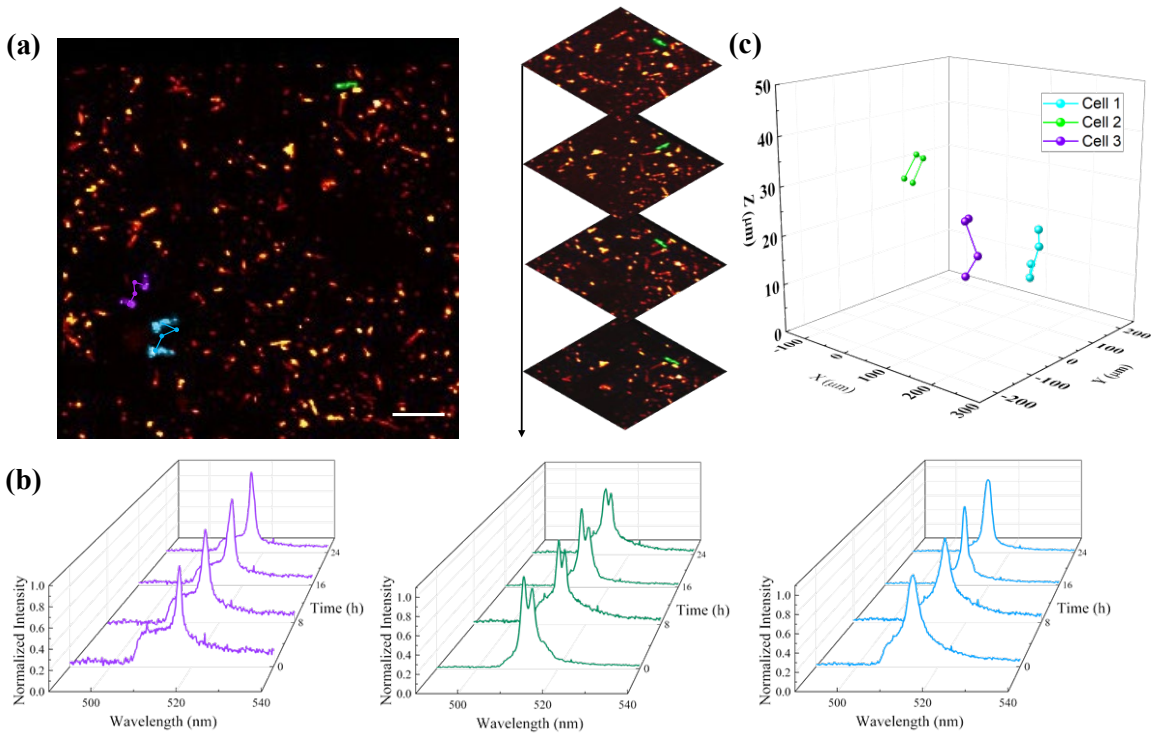

Figure 3.7 *In vitro* cell migration tracking. (a) The corresponding fluorescence 2D macrophage migration trajectory. The tracked macrophages are accordingly highlighted with purple, green and blue. The right inset is a demonstration of macrophage migration over time through multiple frames. (b) The normalized lasing spectra were collected for macrophage migration tracking over time. The purple, green, and blue waterfall spectra are corresponding to the same color-labeled macrophages in (a) and (b) respectively. (c) The *in vitro* 3D macrophage migration trajectory was extracted from multiple OCT scans over 24 hours. The tracked macrophages are highlighted with purple green and blue. Scale bar: 100 μm. [42]

3.4.2 In Vivo Subretinal Cell Tracking with Nanowire Lasers

After macrophages internalized nanowires over 24-hour culture, they were re-suspended in a cell-enriched solution. Then, a 20 μL cell-enriched solution was injected into the subretinal layer (Figure 3.8) via a Hamilton syringe.

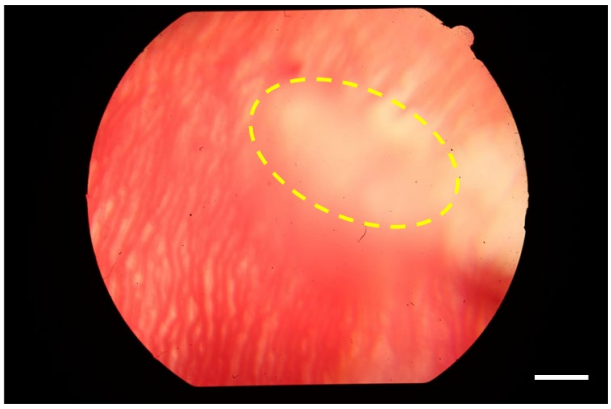

Figure 3.8 A color fundus image in albino rabbit. The region of sub-retinal injection of nanowire-labeled macrophages is highlighted.[42]

The *in vivo* cell tracking experiments were conducted 3 days later once the localized subretinal fluid had been absorbed. Figure 3.9 shows a representative cross-sectional image acquired by the OCT of the injection area. The locations of macrophages carrying nanowire lasers are indicated by the red arrows. By analyzing the signal profile along the yellow dashed line in the inset of Figure 3.9, one can see that the nanowire provides a significant 25 dB OCT signal enhancement compared to the surrounding retinal layers. Figure 3.10 provided a comparison image

of macrophages labeled with and without CdS nanowires in the subretinal layers. The CdS could provide significant signal enhancement.

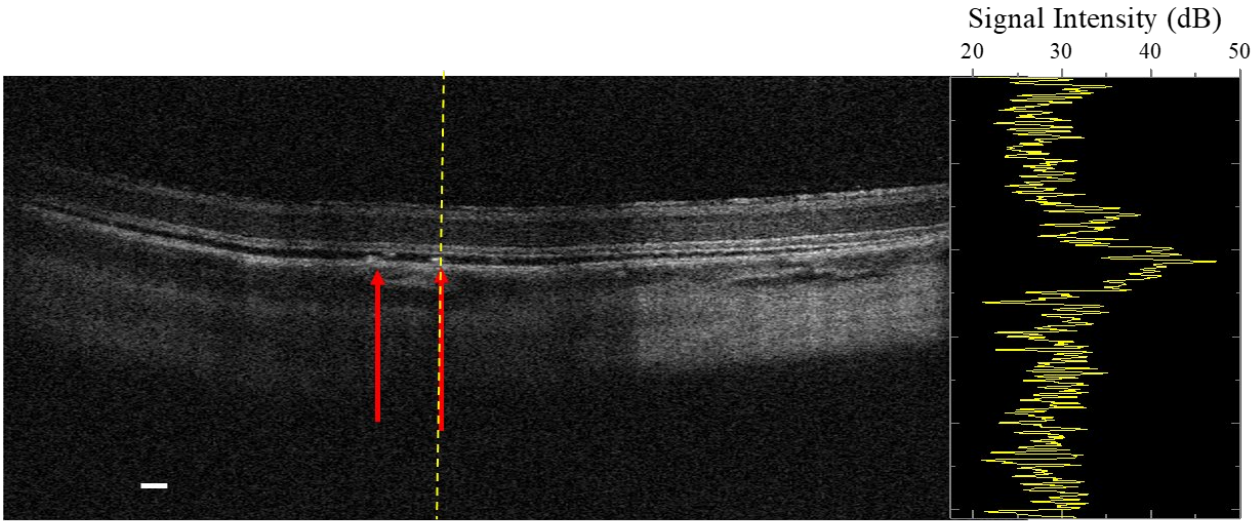

Figure 3.9 OCT B-scan image collected 2 days after the injection. The nanowire-labeled macrophages are indicated by the red arrows. The right inset is a signal intensity curve collected along the yellow dashed line, which shows that nanowires could provide up to 25 dB signal enhancement compared to the surrounding retinal layers.[42]

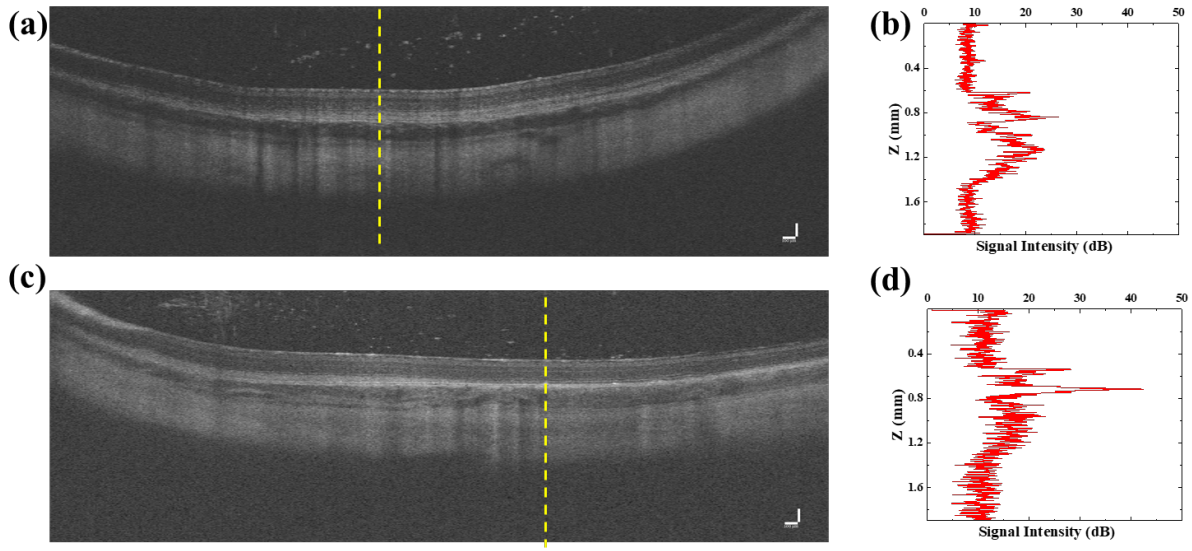

Figure 3.10 OCT contrast from CdS nanowire lasers. (a) An OCT cross-sectional image of macrophages without Cd nanowire lasers. (b) An imaging contrast profile measured along the yellow dashed line in (a). (c) An OCT cross-sectional image of macrophages in the subretinal layer with CdS nanowire lasers. (d) An imaging contrast profile measured along the yellow dashed line in (c). Scale bar: 100 μm.[42]

The X-Y plane projection of the macrophage spatial distribution and the FM image were collected from the same area (Figure 3.11(a) and (b), respectively), showing a perfect match. Based on this signal enhancement, the 3D total distribution of macrophages in the subretinal layer was extracted by signal thresholding. Figure 3.11(c) shows the two selected lasing emission spectra collected from the locations indicated in Figure 3.11(a) and (b) to prove that the distinct lasing spectra can be acquired even under the retina layer of living animals.

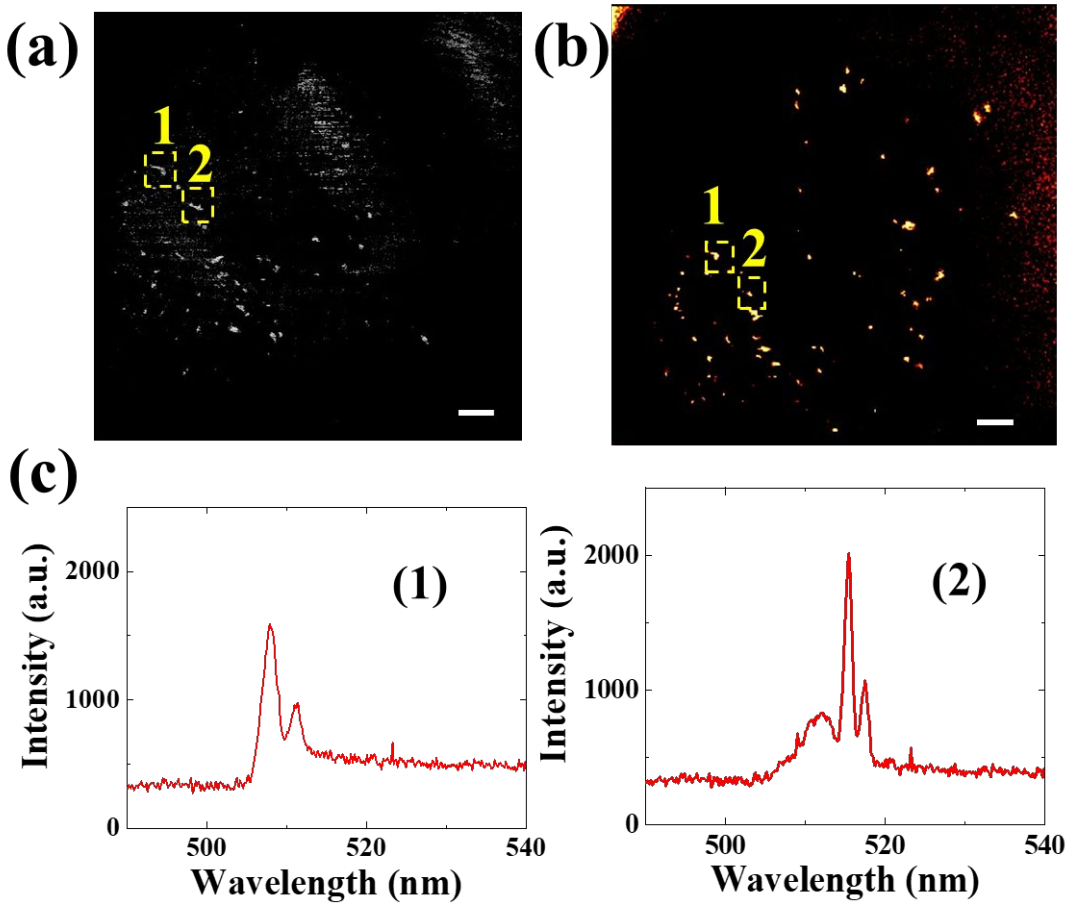

Figure 3.11 (a) 2D X-Y plane OCT image of the same field of view in (b) at the same time. (b) FM image of nanowire-labeled macrophages attached to the retinal layer that was acquired from the same field of view in (a). Two macrophages labeled with nanowires are tracked as (1) and (2). (c) Two unique lasing spectra (1)-(2) were collected from the two tracked macrophages in (a) and (b). Scale bar: 100 μm.[42]

Figure 3.12(a) and (b) show the top and side views of 3D OCT image reconstruction, respectively. The retina structure appears as a white region and the macrophage distribution is labeled in blue. Most of the macrophages were attached under the retina layer, whereas some of them were on the retina layer due to leakage during the subretinal injection. A 3D rendering video of the retina structure and macrophage distribution is presented.

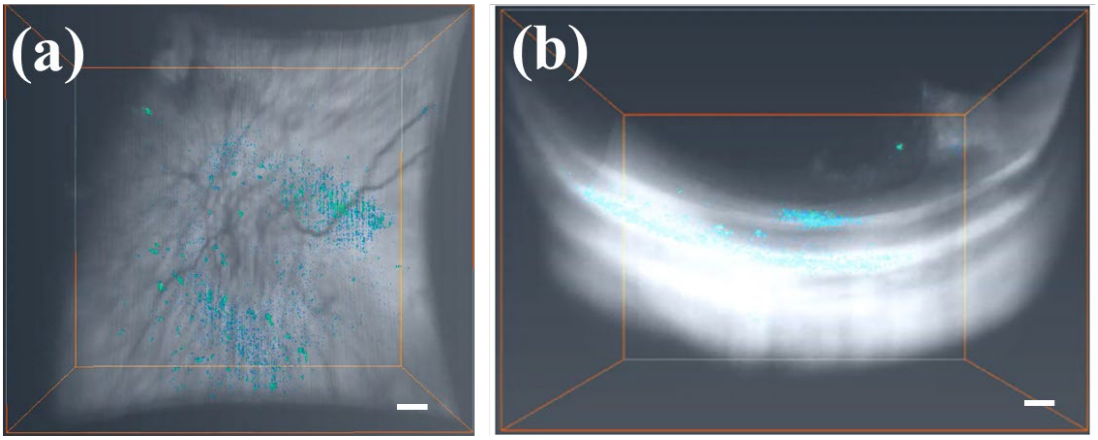

Figure 3.12 Top (a) and side (b) views of 3D OCT retinal layer reconstruction and the distribution of macrophages. The nanowire-labeled macrophages are extracted by thresholding segmentation and colored with blue. [42]

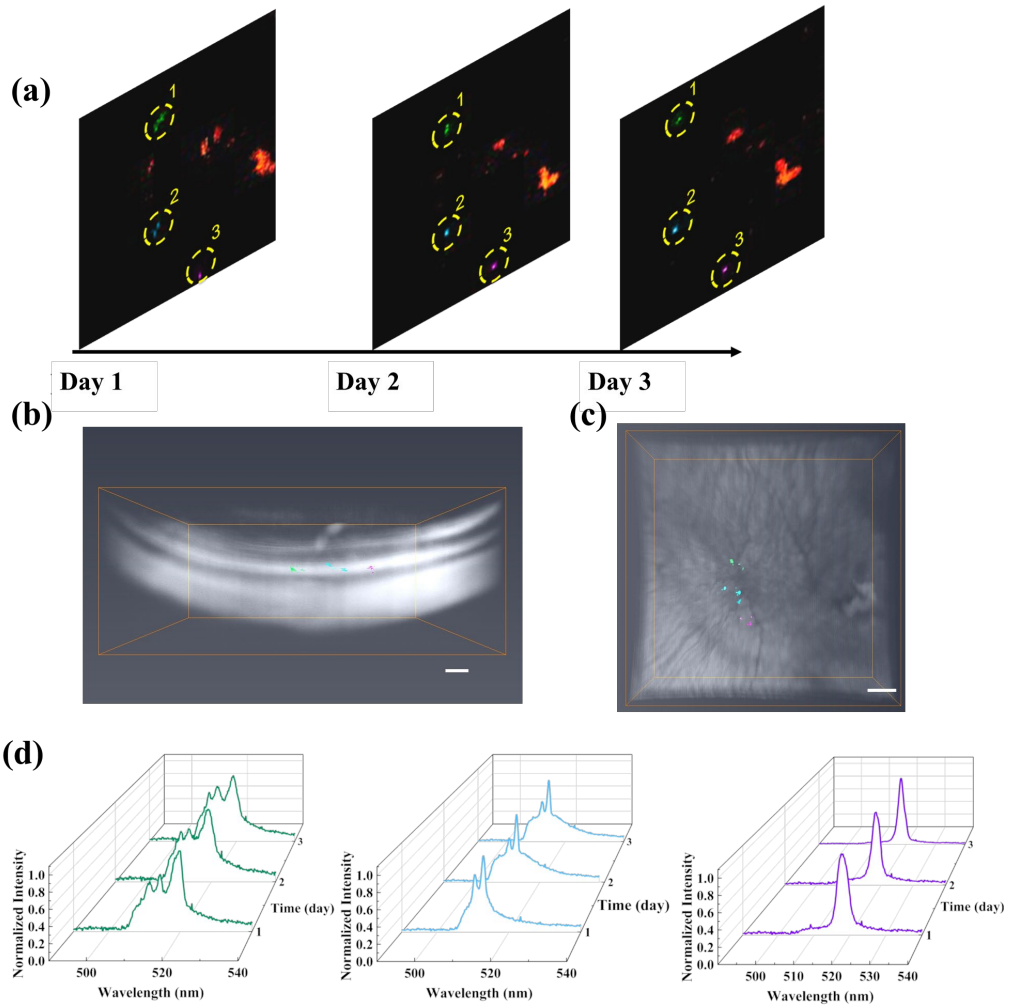

Figure 3.13 *In vivo* cell migration tracking. (a) *In vivo* fluorescence images of macrophage migration projections through multiple observations. Three of the tracked macrophages are highlighted with green, blue, and purple. (b)-(c) Side and top views of 3D OCT retinal layer reconstruction and the spatial locations of macrophages. The spatial locations of the same nanowire-labeled macrophages in (a) over 3 days are extracted by thresholding segmentation and superimposed with the retinal structure with the corresponding colors in (a). (d) Normalized lasing spectra were collected for macrophage migration tracking over time. The green, blue and purple waterfall spectra are corresponding to the same color-labeled macrophages in (a), (b), and (c). [42]

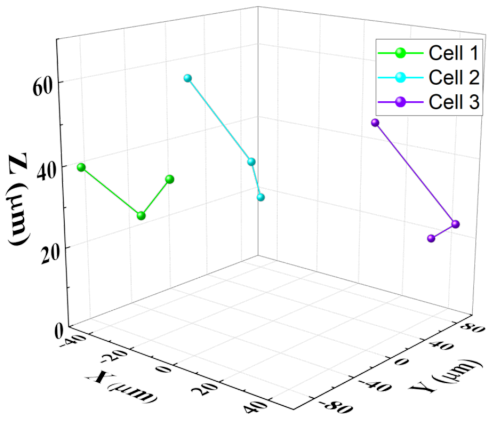

Figure 3.14 The *in vivo* 3D macrophage migration trajectory extracted from multiple OCT scans over 3 days. The tracked macrophages are highlighted with green, blue, and purple accordingly. [42]

In this study, we demonstrated CdS nanowire lasers internalized by macrophages could be utilized as *in vivo* cell tracking identifiers while offering enhanced contrast for both OCT and FM. To validate the feasibility for cell tracking, we first performed *in vitro* experiments to monitor macrophages migration on fibrin hydrogels for 24 hours, and then performed an *in vivo* study to track the macrophages delivered to the rabbit eyes via subretinal injection. The injected macrophages were monitored longitudinally *in vivo* for 3 successive days, and the 3D migration trajectories of individual cells were successfully extracted from OCT images.

Our technology provides an *in vivo* cell tracking technology combined with the advantages of OCT and lasing emission labeling. Compared to fluorescence labeling, the enhanced OCT contrast of nanowires could overcome the omnipresent scattering from tissue layers to provide precise 3D spatial information with better imaging depth. Meanwhile, the lasing emission labeling takes advantage of lasing spectral information such as lasing peaks' positions and relative intensities, rather than merely emission intensity, which provides unique identification to track the migration of individual cells.

There are also some limitations of our technology in this stage: First, the size of nanowires is still relatively large for massively cell internalization and internalization. To solve this problem, biocompatible coating of the nanowire lasers could help improve the internalization rate for further applications. Some microfabrication based microcavity lasers like microdisk with smaller size should also be considered as a potential choice to improve the labeling performance. Second, the total labeled cells are limited. The theoretical number of distinct spectral labels provided by CdS nanowire lasers is approximately 1300 (discussed in Section 3.3.8). However, now we only demonstrated tracking cells of 3. The major limitation here is the resolution of the spectrometer that may not differentiate multiple peaks precisely. A finer diffraction grating can be utilized to improve the spectral resolution of the spectrometer to identify a larger number of labels. On the other hand, by optimizing the microfabrication design of the nanowire lasers can provide richer spectral information to label a larger number of cells. Lastly, since CdS is a kind of low toxicity material, it is not ideal for *in vivo* study. In the future microcavity laser design, it is possible to utilize non-toxic materials like GaN, ZnO to build the laser particles to avoid potential biotoxicological response.

Our technique can shed new light on cell-based therapies and understanding disease models at a single-cell level. For stem cell therapy, this technique may track the migration of stem cells to evaluate treatment efficacy and safety. For research on the role of inflammatory cells in pathologic conditions such as diabetes, macrophages can be tracked when they pass through the retinal layer. Our technology could also be applied to *in vitro* cell tracking studies that require deep imaging depth, such as the studies on organoids and artificial tissues. In the next chapter, the application of this technique in retinal stem cell tracking with longer longitudinal study and larger tracked cell population is demonstrated.

Chapter 4 Single Cell Tracking for Stem Cell Therapies

4.1 Overview of Stem Cell Therapy

Stem cell therapy, also known as regenerative medicine therapies (RMTs), has attracted significant interest as potential treatment options for severe tissue damages and numerous currently incurable diseases [117-120]. The stem cells have the ability of unlimited self-reproduce with the same characteristics of the original cells. Besides, they could give rise to a specialized cell type that finally becomes part of patient body. Therefore, in many stem cell therapies, transplanted cells are administered close to the damaged tissue to migrate towards and stay within the damaged tissue, and then replicate and differentiate into multiple cell types to restore the structure and function of the targeted regions [118, 121, 122]. For instance, several clinical trials have been conducted for administering retinal pigment epithelium (RPE) cells via subretinal injections for RPE degeneration restoration in the retina in geographic atrophy of macular degeneration [122-125]. After being introduced into the subretinal space, the transplanted RPE cells can create a functional RPE layer to replace the damaged original RPE as a part of the photoreceptor restoration process.

However, the trait for stem cells is also true for the cancer cells that divide in an uncontrolled manner. Despite the great promise of stem cell-based therapeutic method, the lack of comprehensive understanding of the migration, replication, and fate of the transplanted cells remains a major obstacle in clinical application. Therefore, the safety and efficacy evaluation are critical for the development of stem cell therapy. As the traditional method to evaluate therapeutic efficacy and safety, histological analysis can only provide limited information due to its invasive

and destructive nature [126, 127]. Optical imaging technologies that can directly and precisely monitor the 3D distribution and migration of implanted cells *in vivo* and longitudinally are highly desired.

4.2 Current Imaging Technology for Tracking Stem Cell Therapies

As we have discussed in the above sections, optical imaging modalities have numerous advantages in clinical applications regarding the simplicity of use, wide wavelengths ranges, and high resolutions. Therefore, optical imaging modalities have been widely applied in monitoring stem cell therapies and evaluate the treatment effects non-invasively. Many imaging techniques, such as fluorescence microscopy (FM) and optical coherence tomography (OCT), have been applied in labeling and tracking transplanted cells [42, 107, 128, 129]. Fluorescence labeling is a widely used technique in differentiating various targets and tracking cell migration [17, 107, 128]. Multi-spectral fluorescence labels were exploited to provide distinguishable information to track different cell groups *in vivo* with various light emission spectra from different colors of fluorophores [107]. However, due to the nature of broad emission spectra of fluorophores, the total available different labels involved in multi-spectral fluorescence imaging are limited. In addition, as a result of low efficiency and photobleaching, fluorescence dyes usually cannot enable a high signal-to-noise ratio for single cell tracking or support longitudinal studies over extended periods which are necessary for cell-based regenerative therapies. More importantly, for *in vivo* applications, the FM images can only provide 2D information but not 3D information, which is crucial for studying the interaction of cells with the surrounding tissue. OCT is a clinically available 3D imaging technology with ultra-high resolution and excellent imaging depth [112, 130] and has shown great potential for *in vivo* cell tracking. Contrast agents such as gold nanoparticles [27, 131], polymer, and metal oxide nanoparticles [132, 133] with strong scattering

properties have been applied to label target cells to improve imaging visibility. However, since the optical properties of most contrast agents are homogenous, the current OCT-based technique is only capable of monitoring the overall distributions of labeled cells. 3D longitudinal tracking of individual cells *in vivo* still remains a technical challenge. However, currently, there is no single technology that could meet all the requirements for the study purpose.

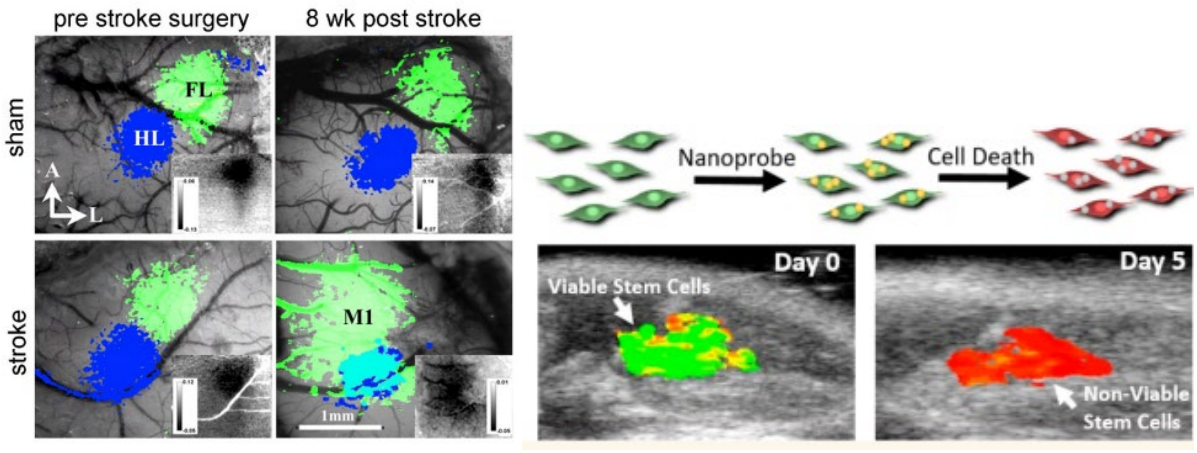

4.3 Motivation with microcavity lasers

From Section 4.2, we can notice that there is a strong need to utilize optical imaging modality to study the activities of transplanted stem cells *in vivo*, realize high 3D structural resolution and provide single cell tracking information. In this project, we were targeting to tackle this challenge. As discussed in Chapter 2-4, Microcavity laser emission-based imaging is an emerging technology in biomedical research. Owing to the small size, high emission intensities, narrow linewidth, and abundant spectral information, the microcavity lasers have shown great potential in intracellular labeling [10, 109, 135, 136] and microenvironmental sensing [10, 137-139]. The hundred-fold narrower emission linewidth and higher signal-to-noise ratio of intracellular microcavity lasers have demonstrated great advantages over the traditional

fluorescence labeling. The unique lasing spectra with multiple peaks with nanometer-level linewidth determined by the varying cavity structure could serve as "identifiers" for differentiating individual cells. Encoded with a "serial number" formed by the lasing peak positions of the microcavity lasers, a large number of cells can be individually tracked at the same time. However, similar to FM, the *in vivo* tracking based on lasing emission provides only 2D images and the critical 3D location information cannot be captured.

In this study, we demonstrated a multimodality imaging technology combining OCT, FM, and lasing emission labeling to longitudinally track the *in vivo* 3D migration trajectories of individual retinal pigment epithelium (ARPE-19) cells transplanted into the subretinal space. The rabbit model involved in this study was laser-induced retinal pigment epithelium (RPE) photocoagulation injury in the retina. The surface-modified CdS nanowire lasers, with the distinct lasing spectra generated from the subtle microcavity differences, were utilized as unique identifiers to label the transplanted ARPE-19 cells. Meanwhile, with strong optical scattering and fluorescence emission, CdS nanowires also served as OCT and FM contrast agents to indicate the spatial locations of the transplanted ARPE-19 cells. In this work, this dual-modality contrast along with the differentiable identifiers provided by the lasing spectra of CdS nanowires built the fundamental for *in vivo* single cell tracking. After the ARPE-19 cells labeled with CdS nanowires were implanted, FM could provide the overall 2D cell distribution pattern, whereas the nanowires internalized by the cells were pumped to provide unique lasing emission spectra for differentiating individual cells. At the same time, OCT en-face imaging could provide both 3D retinal structure and spatial locations of the cells, which were cross-validated with the FM images. Thus, by integrating the capabilities of FM, OCT, and lasing emission labeling, this multimodality imaging

method achieved longitudinal 3D tracking of individual cells in the subretinal space *in vivo* for the first time.

4.4 Experimental Setup and Methods

4.4.1 Experimental Setup

An OCT, FM, and lasing emission spectra multimodality imaging system was utilized for *in vivo* single cell tracking in this study. As shown in Figure 4.2(a), a spectral-domain OCT (SD-OCT) was integrated with the fluorescence detection photodiode and lasing measurement spectrometer. A broadly tunable pulsed diode-pumped solid-state laser working at 485 nm was coaxially combined with the OCT light to provide fluorescence and lasing excitation and ensure the co-registration between different imaging modalities. The OCT reflection, fluorescence, and lasing emission were collected and measured from the backward optical path of the telescope configuration. The ARPE-19 cells were labeled with CdS nanowires and introduced into the subretinal space of the rabbits with laser-induced injuries in the retina (Figure 4.2(b)). The OCT and FM images were employed for cell spatial location extraction, whereas the lasing emission spectra of the nanowires served as identifiers.

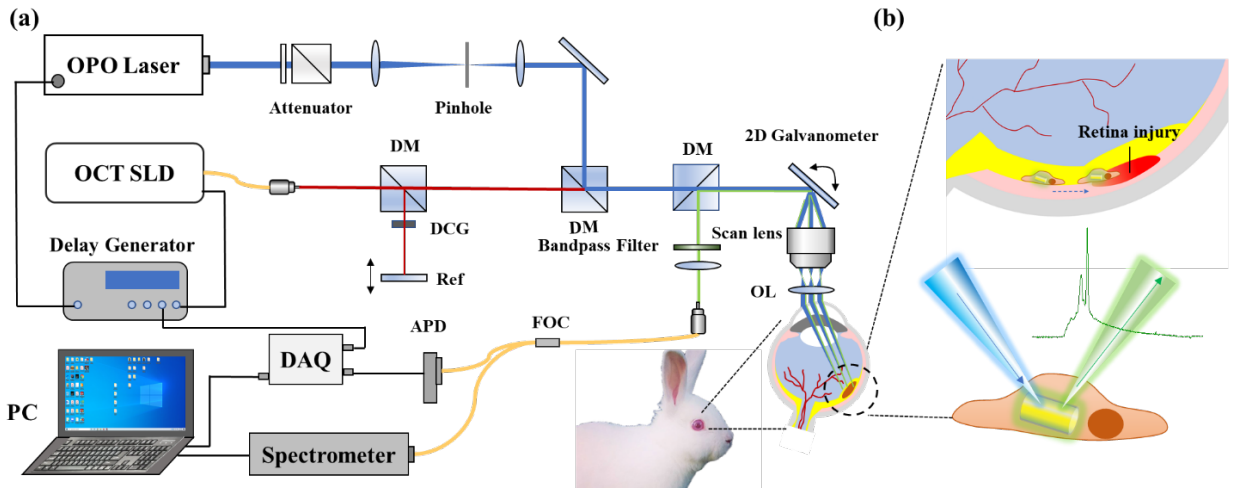

Figure 4.2 Experimental setup and schematic. (a) Schematic of the optical coherence tomography (OCT), fluorescence microscopy, (FM), and laser emission multimodality imaging system. APD: Avalanche photodiode; DAQ: Data acquisition card; DCG: Dispersion-compensation glass; FOC: Fiber optic coupler; SLD: superluminescent diode; DM: dichroic mirror; OL: ophthalmic lens; OPO: optical parametric oscillator. (b) Illustration of CdS nanowire labeled ARPE-19 cells migrating in the subretinal layer and generating lasing emission for tracking identification.

4.4.2 Preparation of Animal Model and Biocompatible Coating of CdS Nanowires

In order to simulate an authentic, clinically relevant pathological environment for cell therapy, laser-induced photocoagulation injuries of the retina and RPE were created in rabbit eyes. As shown in Figure 4.3, two arrays of laser-induced injury spots with 1-mm spacing were highlighted by arrows. The CdS nanowire lasers served as both OCT and FM contrast agents and unique identifiers.

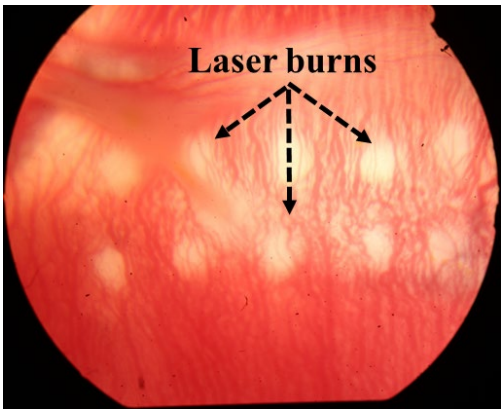

Figure 4.3 The color fundus image of an experimental rabbit. The two arrays of laser photocoagulation burn injuries are marked.

To achieve successful cell labeling, the CdS nanowires need to be internalized into the cells. Considering the relatively large size of nanowires (3-7 μm in length and 200 nm in diameter) relative to the ARPE-19 cells (~30 μm), biocompatible surface modification of CdS nanowires is necessary. A multilayer collagen coating of CdS nanowire was achieved by a layer-by-layer (LBL) assembly method to promote internalization [140, 141], as shown in Figure 4.4.

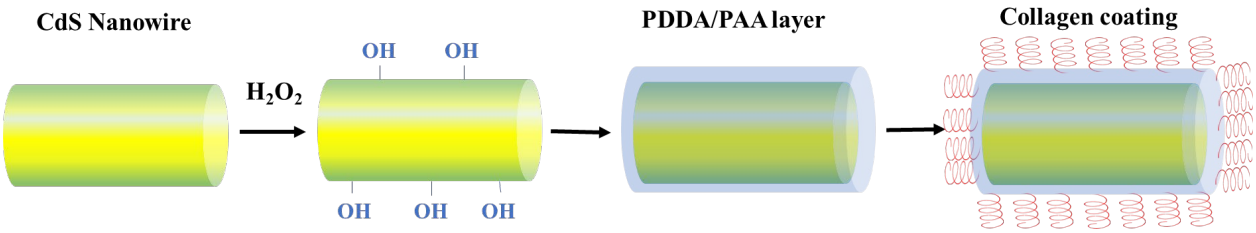

Figure 4.4 The schematic of the PDDA/PAA/collagen biocompatible coating process to promote cell internalization of CdS nanowire lasers.

To confirm the improvement in cell internalization, the ARPE-19 cells were cultured together with surface-modified nanowires and monitored by a confocal fluorescence microscope Figure 4.5. Here, the cell cytoskeleton and nuclei were stained blue and red, respectively, whereas the CdS could be visualized by its green fluorescence emission. From the top and right cross-sectional insets in Figure 4.5, complete internalization of nanowires within the cell body was confirmed. As a control experiment, ARPE-19 cells cultured with bare CdS nanowires showed few nanowire internalizations in Figure 4.6.

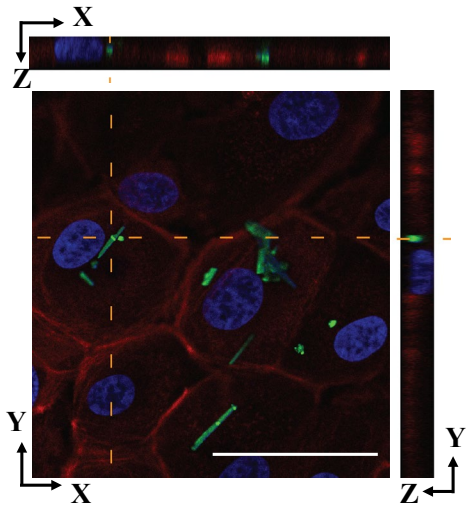

Figure 4.5 A confocal fluorescence image of the surface-modified nanowires internalized by the ARPE-19 cells. The nanowires are labeled in green, and the cell nuclei and skeleton are labeled with blue and red, respectively. The X-Z and Y-Z cross-sectional images along the dashed lines are on the top and right. Scale bar: 50 μm

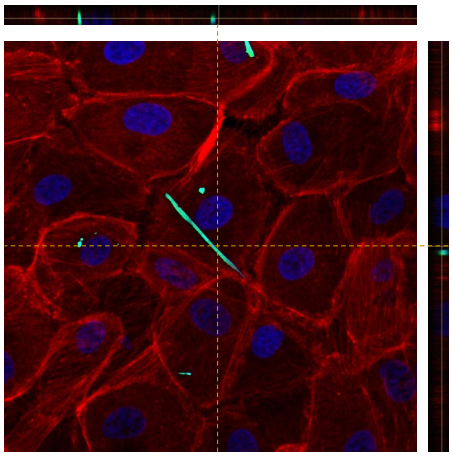

Figure 4.6 Confocal fluorescence image of the non-modified nanowires internalized by ARPE-19 cells. The nanowires are labeled in green, and the cell nuclei and skeleton are labeled with blue and red, respectively. The X-Z and Y-Z cross-sectional images along the dashed lines are on the top and right. Scale bar: 50 μm.

The lasing emission mechanism and additional FM and OCT contrast have been explained in Section 3.4.1. Here in Figure 4.7, we demonstrated a comparison of fluorescence emission (1 $\mu J/mm^2$) and lasing emission (5 $\mu J/mm^2$).

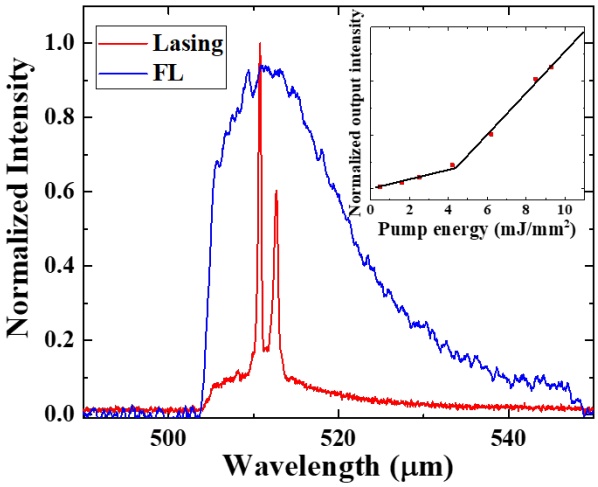

Figure 4.7 A comparison of lasing emission spectra and fluorescence emission spectra. The broad blue curve (FL) is the CdS fluorescence emission spectrum, while the red curve with multiple peaks is the CdS nanowire lasing emission spectrum. The inset in the upper right is the threshold curve of CdS nanowire lasers.

As shown in the OCT image in Figure 4.8, a CdS nanowire labeled ARPE-19 cell was indicated with the yellow arrow. By analyzing the A-scan signal profile along the yellow dashed line (Figure 4.8, right inset), the CdS nanowire was noted to provide 15 dB OCT contrast against the surrounding retina tissue *in vivo*. The capabilities of CdS nanowires to generate fluorescence emission, lasing emission, and OCT contrast form the foundation for single cell tracking *in vivo*.

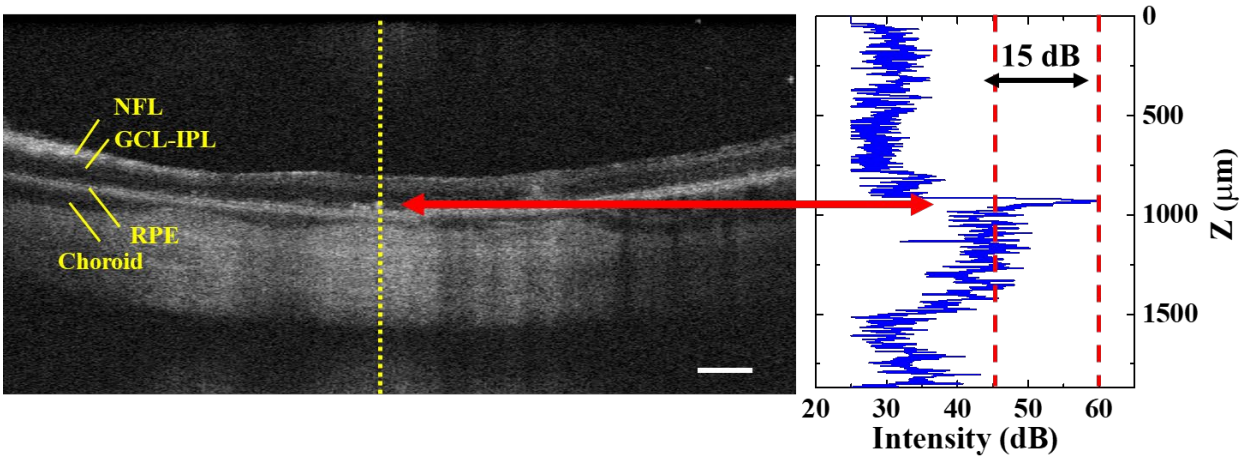

Figure 4.8 OCT B-scan image from the experimental retina region after the injected fluid was fully resolved. The nanowire labeled ARPE-19 cells are highlighted with the red arrow and have higher contrast against the surrounding layers. The right inset is a blue signal intensity curve along the yellow dashed line indicated on the left, which demonstrates that the CdS nanowires can provide a contrast enhancement at a level of 15 dB. NFL: nerve fiber layer; GCL: ganglion cell layer; IPL: inner plexiform layer; RPE: retinal pigment epithelium layer; Scale bar: 200 μm.

4.4.3 OCT, FM, and Laser Emission Spectral Multimodality Imaging System

As shown in Figure 4.2, the multimodality imaging system was developed by integrating spectral-domain OCT (SD-OCT), FM, and laser emission spectrometer. The imaging system was developed by upgrading and improving an OCT and FM dual-modality imaging system described in our previous paper [42, 142]. The SD-OCT was based on a commercially available system from Thorlabs (Ganymede-II-HR, Thorlabs, Newton, NJ). The fluorescence and laser emission were excited by a broadly tunable 42 kHz pulsed diode-pumped solid-state laser (NT-242, Ekspla,

Vilnius, Lithuania, pulse duration 3-6 ns) working at 485 nm with a pulse energy level of 150 nJ before the eye. The OPO laser beam and the broadband OCT near-infrared beam were combined and coaxial aligned together, then passed through the 2D galvanometer, scan lens, and ocular lens to be collimated and incident into the eye optics to focus on the experiment retinal region. The reflected OCT beam, fluorescent, and laser emission were collected through the backward path of a telescope configuration and split by a dichroic mirror. The OCT reflected light, after interference with the beam reflected from the reference arm, led to the A-scan after processing. The fluorescence and laser emission were filtered by a bandpass pass filter (MF 530-43, CWL = 530 nm, BW = 43 nm, Thorlabs, Newton, NJ) and separated by a fiber optic coupler (TN532R2F1, Thorlabs, Newton, NJ) into two measurement channels (energy 9:1), respectively. The major channel (90% of the energy) was coupled into the spectrometer with an integration time of 0.5 s (HR 4000, the customized detection ranges from 470-580 nm, Ocean Optics Inc, Dunedin, FL), and the minor channel (10% of the energy) was coupled into the avalanche photodiode (APD) (APD 110A, Thorlabs, Newton, NJ) and sampled by the DAQ card (PX1500–4, Signatec Inc, Newport Beach, CA, sampling rate 500 MHz). The lateral and axial resolution of SD-OCT was quantified to be 3.8 μm and 4.0 μm, respectively, and the 2D lateral resolution of FM was 4.1 μm [42, 112, 142].

4.4.4 ARPE-19 Cell Preparation and Biocompatible Surface Modification of Nanowires

The ARPE-19 cell line was originally acquired from a commercial vendor (ATCC, Manassas, VA). ARPE-19 cell culture media consisted of DMEM F-12 medium with 1% penicillin/streptomycin and 10% fetal bovine serum (FBS). The cells were cultured in a humidified incubator with 5% CO_2 at 37 °C. All supplies were purchased from Thermo Fisher, Waltham, MA.

The detailed synthesis process of CdS nanowire lasers has been reported in detail in a previous publication [42]. In brief, an Au-nanocluster catalyzed vapor-liquid-solid method was utilized to synthesize the CdS nanowires [114]. To start with, CdS powders (Sigma Aldrich, St. Louis, MO) contained in an alumina boat were placed at the center of the heating source as the source for nanowire growth. Silicon wafers (Ql Electronics Inc., Ningbo, China) covered with an Au film (10 nm thickness) were settled downstream from the CdS powders near the edge of the heating zone. High purity nitrogen gas flow was injected steadily (700 SCCM) into the setup to purge out oxygen. After gas flow cleaning, the CdS powders were heated to 850 °C at 500 mbar pressure for an hour. During the process, the CdS vapor to the Au-catalyzed silicon substrates was transported by a 155 SCCM gas flow to facilitate nanowire growth. After growing for 1 hour, the CdS nanowire product in yellow color was gathered on the silicon substrates.

To promote the biocompatibility of CdS nanowires for cell internalization, a multilayer collagen coating was introduced by a layer-by-layer (LBL) assembly method [141]. The nanowire-carrying silicon wafer was sonicated in ethanol for 10 min to split nanowires from the substrate. After centrifuging the remaining solution, the nanowires were separated from ethanol and redispersed into 30% H_2O_2 solutions (Sigma Aldrich, St. Louis, MO) for 3 min to generate a thin oxidized layer for chemical binding. After rinsing with deionized water for 1 min, the nanowires were immersed into a solution of poly(dimethyldiallylammonium) chloride (PDDA, 0.5%, Sigma Aldrich, St. Louis, MO) for 3 min. Subsequently, the nanowires were dispersed into 0.5% poly(acrylic acid) (PAA, Sigma Aldrich, St. Louis, MO) solution for 3 min. Following the rinsing procedure with deionized water, the nanowires were exposed to 0.1 collagen solutions overnight. Finally, the nanowires were centrifuged down and re-dispersed into phosphate-buffered saline (PBS) solution and ready for culturing with ARPE-19 cells.

When ARPE-19 cells were seeded into the 35 mm culture dish, 200 μL PBS solution containing nanowires was added into the cell media, and the cells were given 24 hours to internalize nanowires. Then the cell culture dish was rinsed with PBS solution 3 times to ensure free-floating nanowires were fully removed prior to *in vivo* experiments.

To confirm that the nanowires were internalized by ARPE-19 cells, confocal fluorescence images were captured on a confocal microscope (LSM 800, Zeiss, Jena, Germany). The cells were fixed with 4% paraformaldehyde solution. Afterward, 4′,6-diamidino-2-phenylindole (DAPI) (1 μg/ml, Sigma Aldrich, St. Louis, MO) and Phalloidin 555 (Life Technologies, Carlsbad, CA) were used to visualize cell nuclei and F-actin and generate blue and red fluorescence emission, respectively.

4.4.5 In Vivo Experiments

The nanowire-labeled ARPE-19 cells were enriched by adding 0.5% Trypsin solution (Thermo Fisher, Waltham, MA) for 5 min at 37 ° C and centrifuging at 500 rcf for 5 min. The detailed procedure of subretinal injection of labeled cells was described in our previous paper [143]. A 3-mm inferotemporal conjunctival peritomy was performed on the eye using Westcott scissors and Castroviejo Forceps 0.12mm. After measuring a distance 3.5 mm posterior to the corneal limbus by a marker, a needle was inserted carefully to keep away from the ciliary vasculature and extraocular muscles. Then, a blunt 30-gauge needle attached to a 50 μL Hamilton syringe (Hamilton, Reno, NV) was inserted through the previous needle inserted site into the vitreous cavity and introduced into the subretinal space about 0.5–1 optic disc diameter inferior to the retinal vessels around the laser burn injury sites to inject 20μL of enriched ARPE-19 solution. A localized pocket of subretinal fluid was administered via injection which covered all of the laser burn injuries. The whole injection procedure was guided by the OCT real-time B-scan imaging to

confirm the injection depth with anatomic retina layers as reference. It typically took 3 days after administration of the subretinal fluid when the injected fluid was fully resolved so that the imaging experiments could commence.

During the imaging experiments, to prevent corneal surface keratopathy, eye wash (Altaire Pharmaceuticals, Inc., Aquebogue, NY) was applied regularly. The experiment rabbit fundus was first imaged by a color fundus camera (TRC 50EX, Topcon Corporation, Tokyo, Japan) to monitor the overall condition of the retina. Subsequently, the rabbits were placed on the stabilization platform of the multimodality imaging system and imaged one eye under the ophthalmic lens. The eyelid was retracted with a pediatric Barraquer wire speculum. Through the integrated charge-coupled device (CCD) camera and the adjustable holding platform, the rabbits could be observed at focus and with stability. During the multimodality imaging and cell tracking experiments, the 3D OCT en-face imaging was conducted first. Following that, the 2D FM scan image was acquired at the same region of interest. According to the FM images, an algorithm of contour detection and weighted center calculation was applied to extract potential locations of nanowires lasers internalized by ARPE-19 cells. The galvanometer was controlled to guide the OPO laser to revisit the extracted locations and excite and collect lasing emission spectra for cell identification confirmation. The acquired OCT en-face image was processed and rendered by the Amira software (FEI, Hillsboro, OR).

4.5 Results

4.5.1 In Vivo Subretinal Single Stem Cell Tracking

First, laser-induced injuries were created in the retina of experimental rabbits to generate a clinically relevant therapy microenvironment. Subsequently, after being cultured with surface-modified CdS nanowires for 24 hours, the ARPE-19 cells were collected and resuspended in the

cell-enriched solution. 20 µL of the cell-enriched solution was injected into the subretinal space through a subretinal injection operation. Localized subretinal fluid including in the region of laser-induced injuries was observed (D1 in Figure 4.9(a)). The imaging experiment for *in vivo* single cell tracking started after the fluid was fully resolved at D4 and was repeated at different time points over a period of 28 days. At each observation time, color fundus images, fluorescence microscopy, OCT en-face imaging, and lasing emission spectra were collected for retinal structure monitoring and single cell tracking. Figure 4.9(a) shows the color fundus images of an experimental rabbit through the period of 28 days to depict the retinal anatomy and appearance. A series of fluorescence microscopy images collected during each observation time are presented in Figure 4.9(b). The black circles and blue circles in Figures 4.9(a) and (b) indicate the laser-induced injury spots on the retina. As time went on after injection, an increasing number of nanowire labeled cells clustered around the injury spots which is consistent with the biological function of ARPE-19 cells.

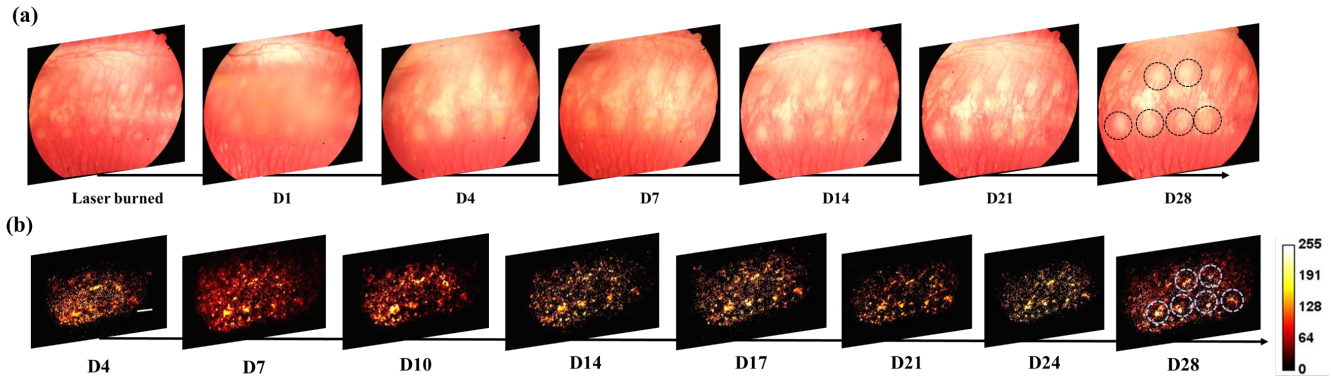

Figure 4.9 Color fundus and FM images for the experimental region. (a) A series of color fundus images of the experimental retina region with laser-induced injuries. The images were acquired at different time points over 28 days. CdS nanowire labeled ARPE-19 cells were injected on Day 1 and were periodically observed starting from Day 4 after the injected fluid was fully resorbed. (b) A series of FM images collected from the same experimental retinal region as in (a) at different time points after the retina region was clear to observe (from Day 4). Scale bar: 200 µm. The black circles and blue circles in (a) and (b), respectively, highlight the locations of laser-induced injury spots.

The FM played an important role in the following aspects. First, FM images depicted the overall 2D distribution of the nanowire labeled ARPE-19 cells. This information was cross-validated with the spatial locations of the cells collected from the 3D OCT scanning. In our data post-processing, the precise spatial distributions of the cells were extracted from OCT en-face images by thresholding, which could be influenced by some strong scattering noise and defects in the animal tissue. The 2D cell distribution information provided by FM could filter out these noises and defects. Second, since it took 1-2 seconds to finish a lasing emission spectra collection, it would be time-consuming and impractical to scan over all the pixels. FM images after thresholding (e.g., Figure 4.10) along with a contour and center extraction algorithm were able to locate the nanowires within the field of view quickly such that the pump light could be delivered directly to the nanowires and their laser emission spectra could be collected subsequently.

A total of 13 cells were tracked through the experiment for Figure 4.9, and their instantaneous 2D locations on D4 were marked in the thresholded FM image (Figure 4.10) as an example. The identities of the 13 tracked ARPE-19 cells were verified by the lasing emission spectra of the carried nanowires. The lasing peak wavelengths are extracted and recorded as a sequence of "barcodes" for cell identity. Therefore, by comparing the barcodes of peak wavelengths as a sequence of numbers from the acquired lasing spectra at various time frames, we can verify whether the cell is the same one or not. Figure 4.11 presents the normalized lasing emission spectra acquired from the same 13 ARPE-cells as in Figure 4.10 over time. The waveforms of lasing emission spectra from these ARPE-19 cells remained stable and distinguishable throughout the experiments for 28 days.

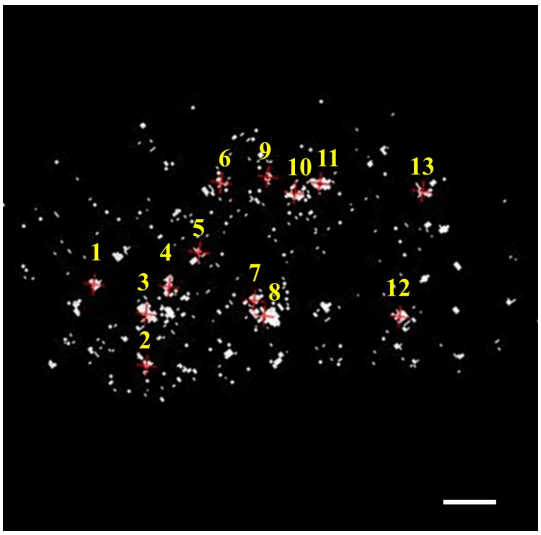

Figure 4.10 The instantaneous 2D locations of CdS nanowire labeled ARPE-19 cells were extracted from the FM image on D4. In total, 13 cells were tracked in this result.

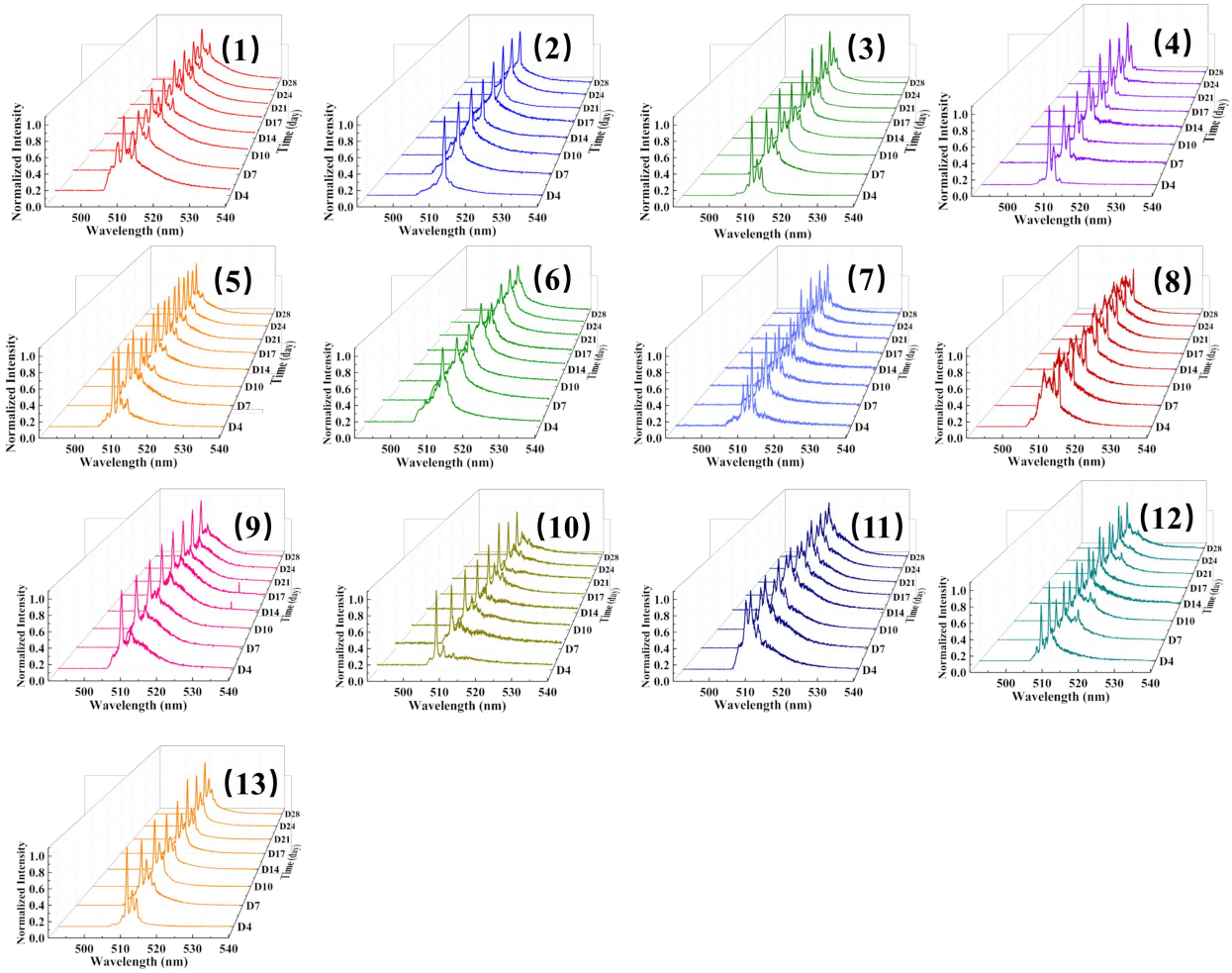

Figure 4.11 Lasing emission spectra collected from tracked cells. Normalized lasing spectra from the 13 identified ARPE-19 cells acquired at different time points during 28 days. Each cell identity was presented by a unique lasing spectral waveform which was stable over the entire observation period.

Measuring the lasing emission spectra of CdS labeled ARPE-19 cells enabled the identification of individual cells, while the relative 3D locations of the ARPE-19 cells within the retina were acquired by OCT volume scanning. Facilitated by the strong optical scattering of CdS nanowires, the distributions of cells in an OCT image could be extracted via signal thresholding. Figure 4.12(a) shows a series of OCT maximum intensity projection (MIP) images in the XY plane of the same field of view. The overall retina structure was rendered in grayscale whereas the thresholded signals were labeled in yellow. The laser-induced retinal injury areas were highlighted by the red circles. Figure 4.12(b) demonstrates the side view of the OCT 3D rendering; the distribution of extracted labeled cells is mainly in the subretinal space, which is consistent with the original injection location. Extracting the locations of individual cells by solely thresholding OCT signals could lead to artifacts caused by the strong scattering noise and defects in the tissue. By leveraging the FM and OCT dual contrast of CdS nanowires, the FM images acquired from the same region of interest worked as cross-validation. By comparing the FM images and OCT XY plane projection, only the extracted signals which appeared in both FM and OCT images were considered as valid cells. With the overall distribution pattern provided by FM (Figure 4.12(c)), the tracked cells in Figure 4.10 were easily extracted in the OCT volume rendering. The top view and side view of the spatial locations of tracked cells after cross-validation with FM images are highlighted in Figures 4.12(d) and (e). The red circles in Figure 4.12(d) are corresponding to the laser-induced regions in Figure 4.11(a) and (c).

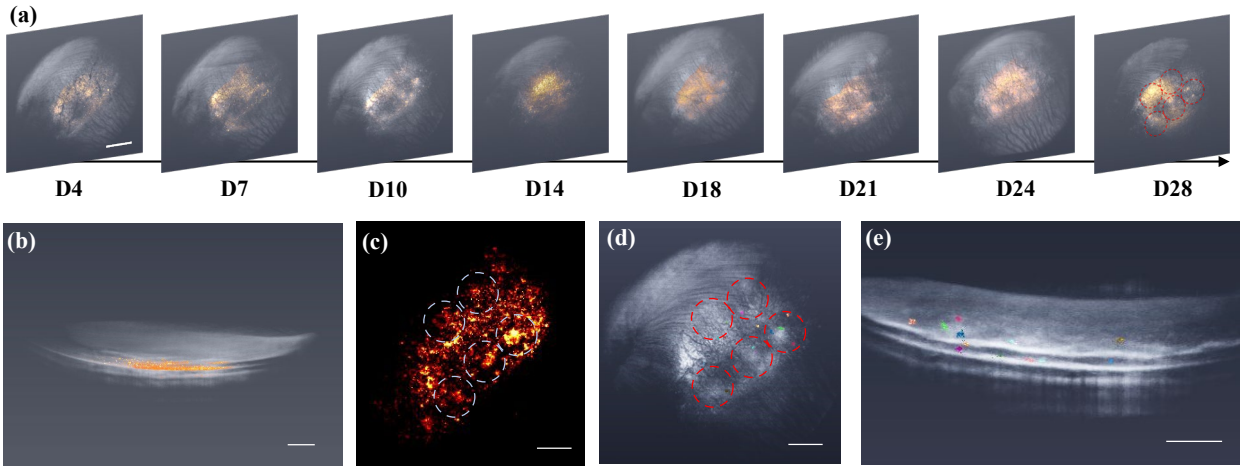

Figure 4.12 OCT stem cell tracking images. (a) A series of OCT X-Y plane projection images of the same region as in Figure 4.9 for 28 days. The overall retinal structure is rendered in grayscale and nanowire labeled ARPE-19 cells after thresholding are highlighted in yellow. (b) The side view of the 3D rendering of D21 shows that the extracted cells are mostly distributed in the subretinal space. Scale bar: 800 μm. (c) The corresponding FM image of the same region. The distribution pattern of the fluorescence signal was used to cross-validate the extracted OCT pattern in (a), which confirmed the existence of CdS nanowire lasers and excluded noise. Scale bar: 800 μm. (d) The labeled cells corresponded to Figure 4.10 were highlighted with various colors in the OCT 3D volume rendering. The exact spatial coordinates were extracted from OCT. Scale bar: 800 μm. The gray and red circles in (a), (c), and (d), respectively, highlighted the corresponding laser-induced retina injury spots. (e) A side view of the 3D rendering of the same cells in (c). Scale bar: 500 μm.

Figure 4.13(a) provides a cross-sectional B-scan image from OCT scanning to demonstrate the relative positions of nanowire labeled cells and the retina structure. This B-scan image also confirmed that more ARPE-19 cells were clustered near the laser-induced injury spots. As for the spatial location extraction, the Z-axis coordinates of the cells were measured as the distance from the cell to the RPE layer of the retina. With the identity of ARPE-19 verified and 3D location precisely measured, the 3D cell migration trajectories were acquired and shown in Figure 4.13(b).

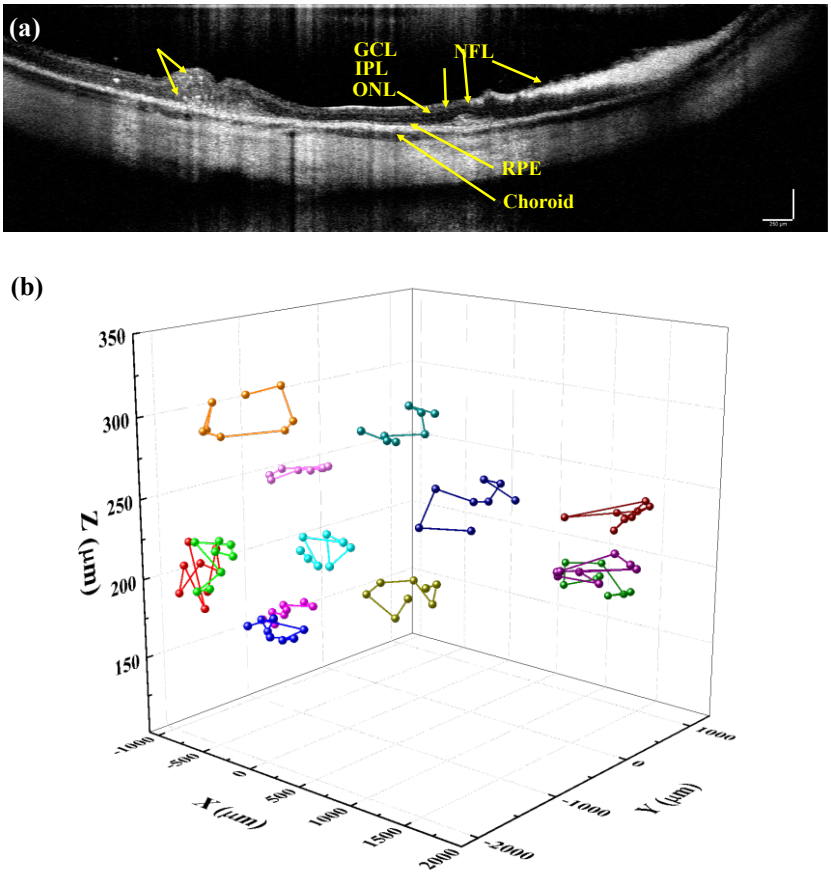

Figure 4.13 Stem cell migration trajectories over time. (a) An OCT cross-sectional B-scan of the experimental retina region. The locations of two tracked ARPE-19 cells labeled with nanowire lasers were indicated with arrows. The retinal layer structures were presented as well. Scale bar: 250 μm. (b) The *in vivo* 3D ARPE-19 cell migration trajectories (13 cells in total) extracted from OCT volume scans acquired at different time points over the 28-day observation period. The z-axis coordinates of the tracked cells were measured by the distance between the cells and the RPE layer of the retina.

To examine the repeatability of the presented imaging technology, the same study was repeated on two additional rabbits (R2 and R3), as shown in Figures 4.14-4.17.

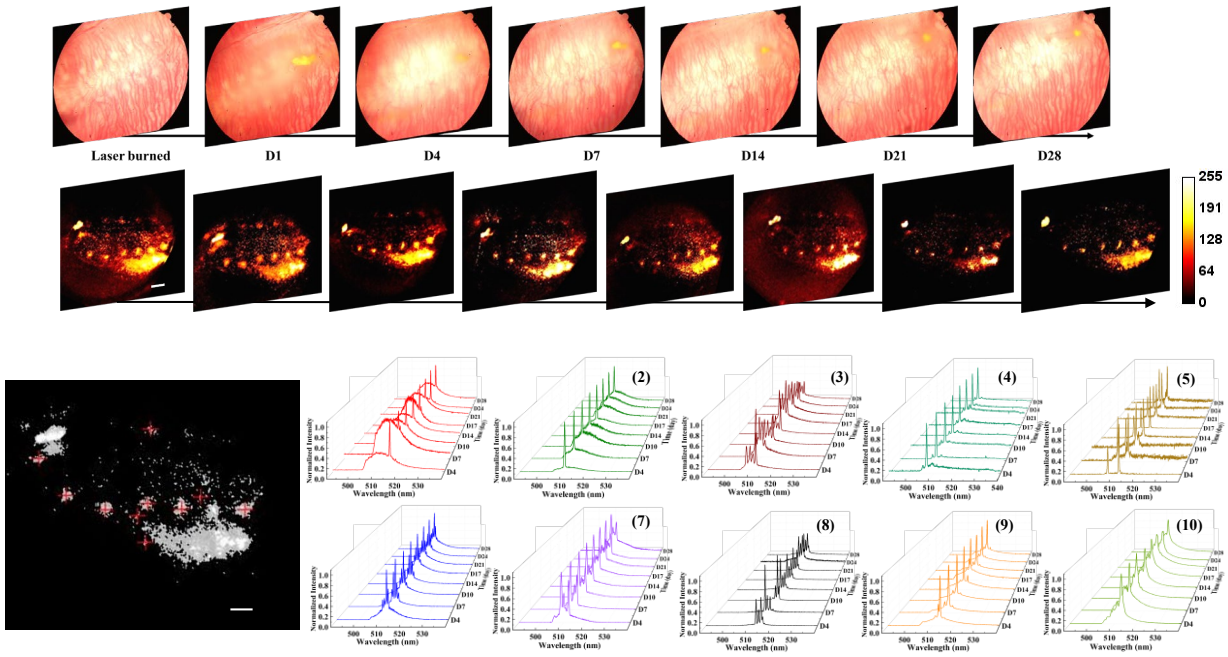

Figure 4.14 Imaging results from an additional rabbit (R2). (a) A series of color fundus images of the experimental retina region with laser-burn injuries. The images were acquired at different time points for 28 days. CdS nanowire labeled ARPE-19 cells were injected on Day 1 and were periodically observed starting from Day 4 after the injected subretinal fluid was fully resorbed. (b) A series of FM images collected from the same experimental retinal region as in (a) at different time points after the retina region was clear to observe (from Day 4). Scale bar: 200 μm. (c) The 2D locations of CdS nanowire labeled ARPE-19 cells extracted from the FM image of D4. In total, 10 cells were tracked in this experiment. (d) Normalized lasing spectra collected from the 10 identified ARPE-19 cells with the same numbers in (c). Each cell identity was presented by the unique lasing spectral waveform which was stable over the entire observation period of 28 days.

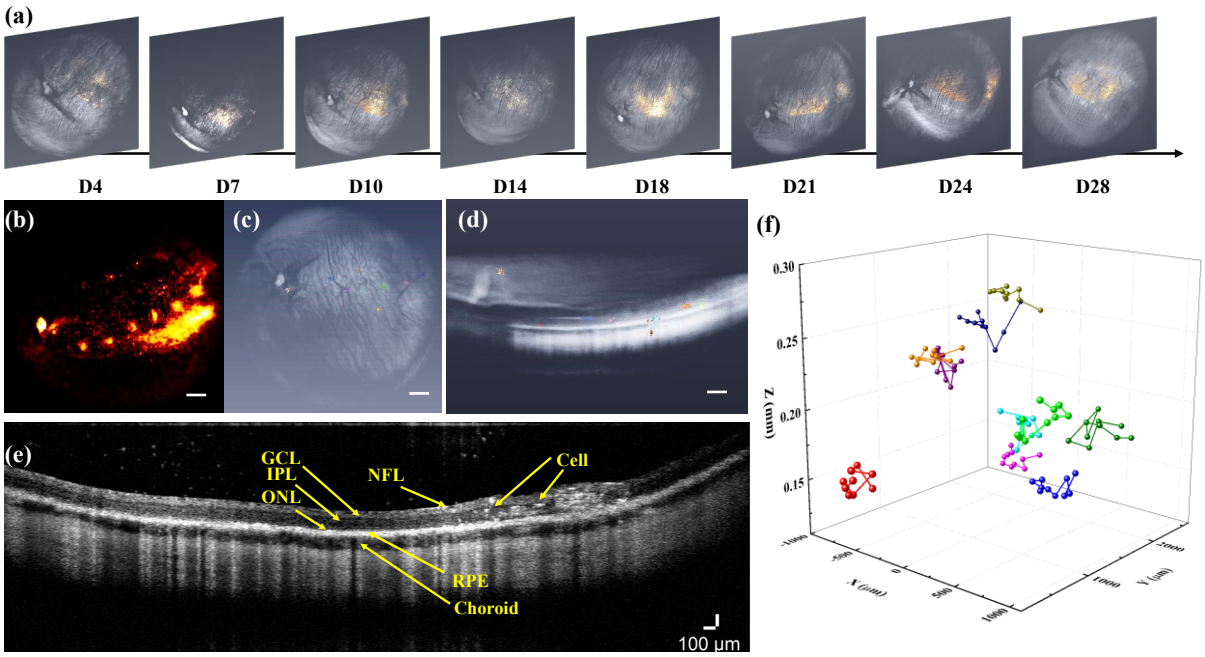

Figure 4.15 Additional animal experiment results from the rabbit (R2). (a) A series of OCT X-Y plane projection images of the same region as in Figures 4.14(a) and (b) over the observation period of 28 days. The overall retina structure is rendered in grayscale and nanowire labeled ARPE-19 cells after thresholding are highlighted in yellow. (b) The corresponding FM image of the same region. The distribution pattern of the fluorescence signal is cross-validated with the extracted OCT pattern in (a), which confirmed the existence of CdS nanowire lasers and excluded noise. Scale bar: 800 μm. (c) The labeled cells corresponded to Figure 4.15(c) were highlighted with various colors in the OCT 3D rendering. The exact spatial coordinates were extracted from OCT. Scale bar: 800 μm. (d) A side view of the 3D rendering of the same cells in (c). Scale bar: 500 μm. (e) An OCT cross-sectional B-scan of the same retina region. The locations of two tracked ARPE-19 cells labeled with nanowire lasers were indicated with arrows. The retinal layer anatomic structures are presented and labeled as well. Scale bar: 250 μm. (f) The *in vivo* 3D ARPE-19 cell migration trajectories (10 cells in total) extracted from OCT volume scans acquired at different time points over the 28-day observation period. The z-axis coordinates of the cells were measured by the distance between the cells and the RPE layer of the retina.

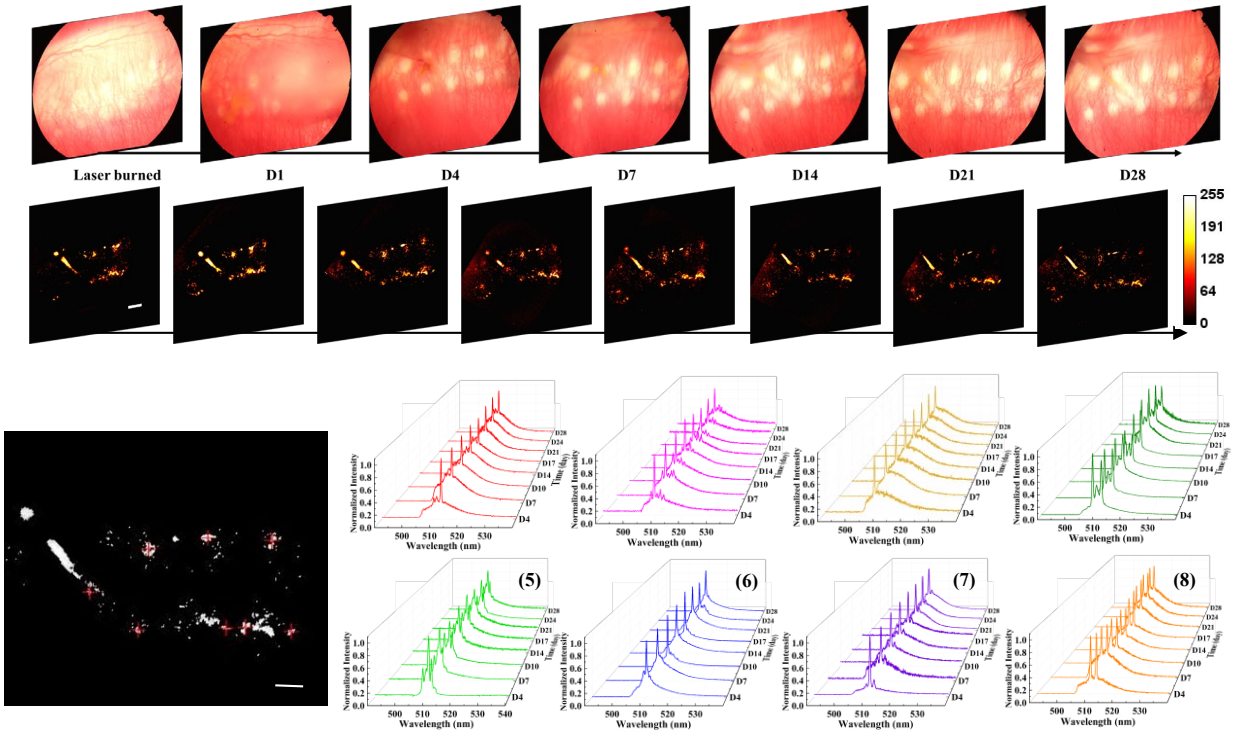

Figure 4.16 Imaging results from Rabbit (R3). (a) A series of color fundus images of the experimental retina region with laser-burn injuries. The images were acquired at different time points for 28 days. CdS nanowire labeled ARPE-19 cells were injected on Day 1 and were periodically observed starting from Day 4 after the injected fluid was fully resorbed. (b) A series of FM images collected from the same experimental retinal region as in (a) at different time points after the retina region was clear to observe (from Day 4). Scale bar: 200 μm. (c) The 2D locations of CdS nanowire labeled ARPE-19 cells extracted from the FM image of D4. In total, 8 cells were tracked in this experiment. (d) Normalized lasing spectra collected from the 8 identified RPE cells with the same numbers in (c). Each cell identity was presented by the unique lasing spectral waveform which was stable over the entire observation period of 28 days.

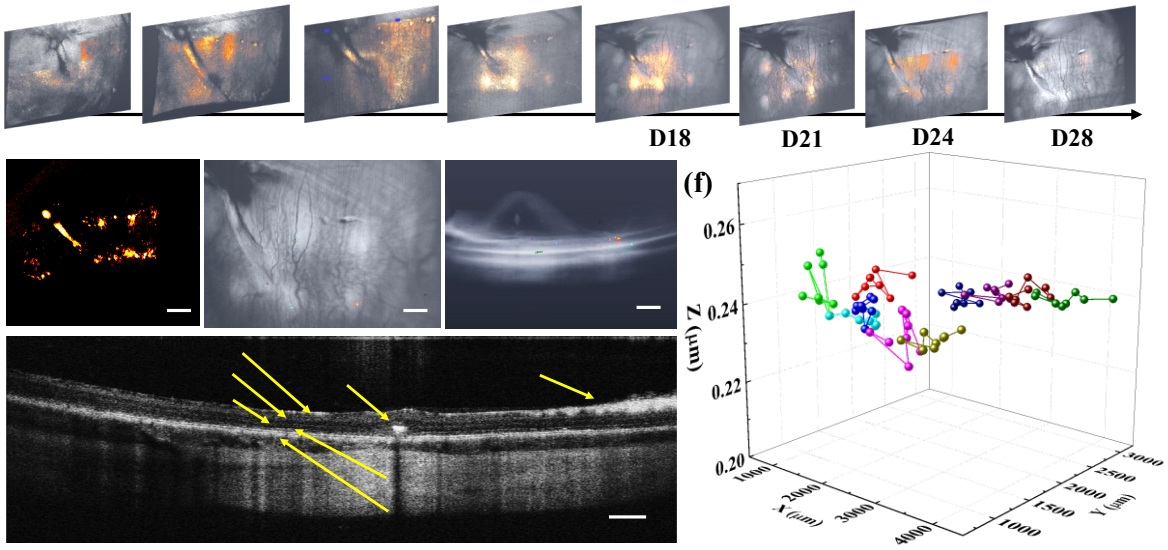

Figure 4.17 Additional animal experiment results from Rabbit (R3). (a) A series of OCT X-Y plane projection images of the same region as in Figures 4.16(a) and (b) over the observation period of 28 days. The overall retina structure is rendered in grayscale and nanowire labeled ARPE-19 cells after thresholding are highlighted in yellow. (b) The corresponding FM image of the same region. The distribution pattern of the fluorescence signal cross-validated with the extracted OCT pattern in (a), which confirmed the existence of CdS nanowire lasers and excluded noise. Scale bar: 800 μm. (c) The labeled cells corresponded to Figure 4.17(c) were highlighted with various colors in the OCT 3D rendering. The exact spatial coordinates were extracted from OCT. Scale bar: 800 μm. (d) A side view of the 3D rendering of the same cells in (c). Scale bar: 500 μm. (e) An OCT cross-sectional B-scan of the same retina region. The locations of a tracked ARPE-19 cells labeled with nanowire lasers were indicated with arrows. The retinal layer structures were presented as well. Scale bar: 250 μm. (f) The *in vivo* 3D ARPE-19 cell migration trajectories (8 cells in total) extracted from OCT volume scans acquired at different time points over the 28-day observation period. The z-axis coordinates of cells were measured by the distance between the cells and the RPE layer of the retina.

In addition, to confirm that the nanowire lasers tracked *in vivo* were indeed carried by the ARPE-19 cells, a control experiment was conducted by injecting the nanowire solution into the subretinal space. The laser-induced injury spots were highlighted by the black circles in Figure 7(a), and also in the FM images in Figure 4.18(b) and the OCT MIP image in Figure 4.18(c). In the OCT MIP and B-scan images in Figures 4.18(c) and (d), the extracted nanowires were labeled with yellow. By looking at the OCT MIP image in Figure 4.18(c) in combination with the FM

images in Figure 4.18(b), we can see that the nanowires were not clustered around the injury spots, and no significant migration of the CdS nanowires was observed during this control experiment.

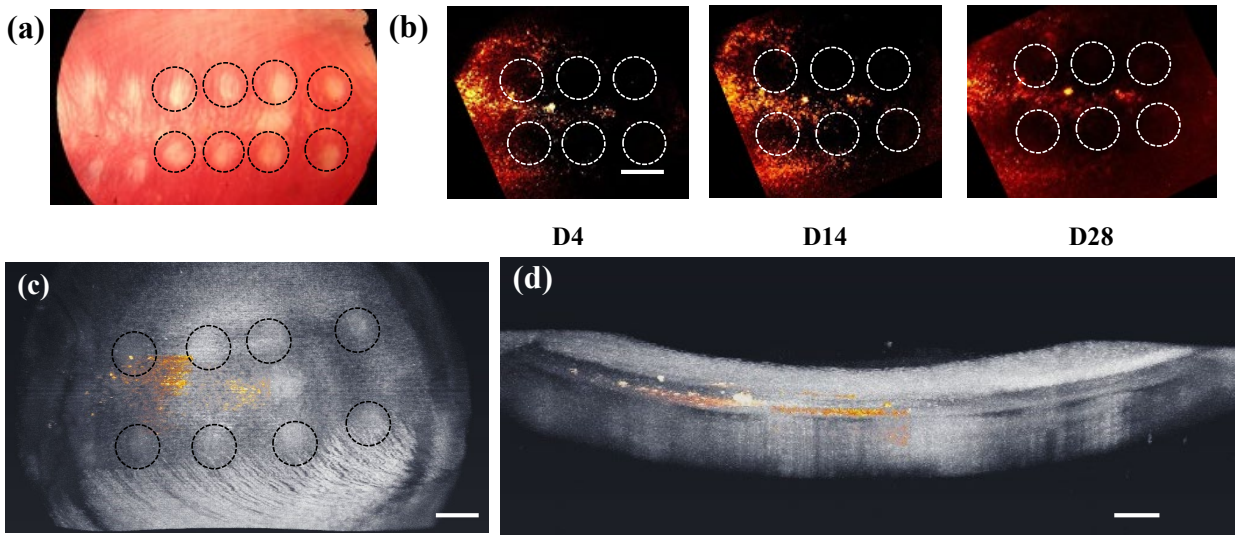

Figure 4.18 Control group imaging results. (a) A color fundus image of the experimental retina. The laser photocoagulation injuries were highlighted with black dashed circles. (b) A series of FM images of the subretinal region acquired at several observation time points after injection of CdS nanowire solution (not internalized by the ARPE-19 cells). The laser-induced injury spots are highlighted by the white circles. Scale bar: 800 μm. (c) The X-Y plane projection of the OCT 3D rendering. The overall retina structure is rendered in gray and the extracted nanowires are labeled in yellow. The laser burn injuries are highlighted with black circles. (d) The XZ side view of the 3D OCT rendering as in (c). Scale bar: 250 μm.

After the *in vivo* experiments were finished, hematoxylin and eosin (H&E) stain histology analysis was conducted to validate the results from multimodality imaging. The H&E histological analysis of a cross-sectional slice including an area of laser-induced retinal photocoagulation injury was shown in Figures 4.19(a). Meanwhile, the fluorescence microscopy image of the same region was collected under blue excitation light. The bright green dots in Figure 4.19(b) were the CdS nanowires. The fluorescence microscopy image overlapped on the histology result is presented in Figure 4.19(c), which verified the clustering of the nanowire labeled ARPE-19 cells in the laser-induced injury region.

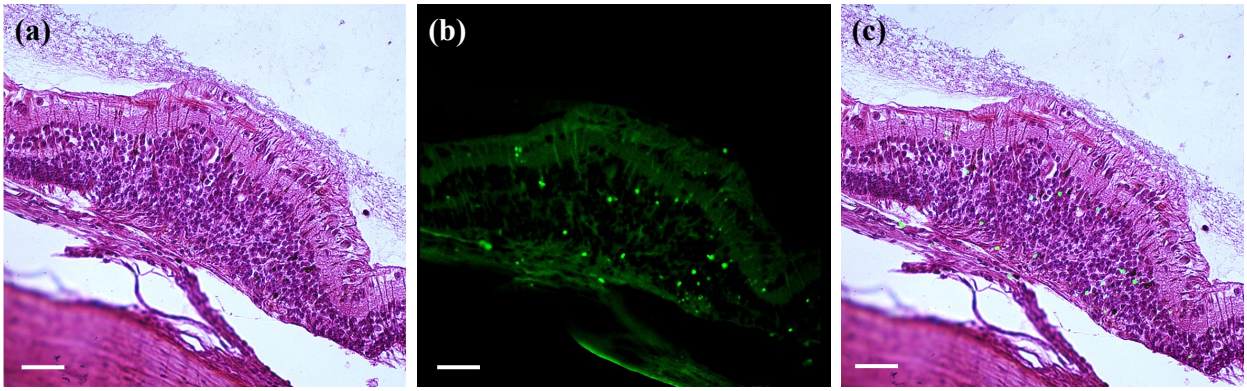

Figure 4.19 Histology analysis of experimental regions. (a) H&E stain histology photo of a retina slice containing a laser-induced injury region. Scale bar: 50 μm. (b) The fluorescence microscopy image of the same region as in (a). The bright green spots are CdS nanowires. Scale bar: 50 μm. (c) The fluorescence microscopy image overlapped on the H&E stain photo, indicating the CdS nanowires clustering in the laser-induced injury region.

4.6 Conclusion and Discussions

In this study, we demonstrated 3D longitudinal tracking of individual ARPE-19 cells *in vivo* with a multimodality imaging system integrating OCT, FM, and lasing emission. The surface-modified CdS nanowires were internalized by ARPE-19 cells and provided both OCT and FM contrast enhancement for precise spatial location extraction and unique lasing emission spectra for cell identification. The nanowire labeled ARPE-19 cells were injected into the subretinal space where laser-induced injuries were created to generate a pathological environment for cell therapy. By integrating 2D and 3D spatial information and the spectral identifying information from each imaging modality, over 10 transplanted cells were monitored individually and tracked longitudinally for 28 days. The overall cell distribution and 3D migration trajectories of individual cells carrying the CdS nanowires were acquired successfully from the FM images and OCT images. The imaging results validated the clustering of the therapeutic ARPE-19 cells within the laser-induced injury areas in the retina as a result of cell migration after subretinal injection. This imaging finding was later confirmed by histology analysis of the retinal tissue slices.

Compared to our previous study [42], we pushed this single cell tracking technology by several important steps towards real-world clinical applications. First, in this study, the ARPE-19 cells were tracked in the damaged retina region, which is a clinically meaningful situation to further prove the feasibility of this technology. Second, the longitudinal study was extended from 3 days to 28 days to capture more meaningful information. Third, by improving the resolution of our spectrometer from 0.3 nm to 0.07 nm, more lasing peaks could be identified clearly in this study. Thus, more "identifier digits" could help improve the number of distinct labels. Compared to three cells tracked last time, in this study, 10+ cells were tracked in 3 rabbits to confirm the improvement in cell tracking. Fourth, the previous study used macrophages, which are very large cells that are adept at phagocytosing material, whereas this study utilized smaller ARPE-19 cells which are being used for regenerative medicine therapies and clinical utilization of cell imaging technologies. It is important to highlight the differences between CdS nanowire lasers and semiconductor quantum dots. Semiconductor quantum dots are also light-emitting particles that are widely applied in labeling biomedical targets. Compared to nanowire lasers, quantum dots have a much smaller size (10-20 nm) and, hence, cannot form lasing resonant cavities. Therefore, the emission linewidth of quantum dots is much bigger than that of CdS nanowires. In most cases, quantum dots have only one peak in the spectra coming from the material band energy gap, while CdS nanowires have multiple peaks coming from the numerous lasing modes. This means quantum dots are not able to provide differentiable identifiers for a large number of individual cells. On the other hand, due to the small size of quantum dots, the optical scattering property is extremely weak for providing OCT contrast so that 3D information of the labeled cells is also not acquirable.

There are several aspects of this technology which could be further improved. First, the repetition rate of our excitation laser was only 1 kHz. As a result, it took minutes to finish the FM

scan, which is time-consuming and introduces unnecessary noise and artifacts. The system could be upgraded by using a laser with a high repetition rate to improve the imaging speed significantly. Second, in our current study, the unique lasing spectrum of CdS nanowire came from the random distribution of the nanowire structures. The size of CdS nanowires is still relatively large for many clinical applications. In order to obtain more unique labels, better control of the lasing emission spectral distribution and better cell labeling capability, improvement in microfabrication and design of microcavity lasers are necessary to reduce the size while increasing the available lasing modes. Third, even though the spectrometer in this study has been upgraded to have better spectral resolution compared to our previous study [42], the temperature noise during the spectrum collection impaired the overall signal-to-noise ratio. To address this problem, a cooled spectrometer may be used for future studies.

Pharmacodynamics (PD) and pharmacokinetics (PK) of transplanted cells are one of the major concerns in state-of-the-art cell-based regenerative medicine and translational applications. The capability to precisely and non-invasively track single cell migration *in vivo* can contribute to the understanding of the PD and PK of cell-based therapies for a comprehensive evaluation of both safety and efficacy. Our technology, by leveraging the advantages of OCT, FM, and lasing emission from surface-modified CdS nanowire lasers, showed the feasibility for 3D tracking the migrations of transplanted progenitor cells accurately and longitudinally in the large-animal subretinal space *in vivo*. The single-cell tracking capability presented in this work could serve as a platform technology to shed new light on understanding the PD and PK of cell-based therapies in ophthalmology and other medical fields. In addition, our technology also holds potential in supporting basic research on biological mechanisms *in vivo* and *in vitro*, such as longitudinal tracking of cell migrations and interactions in organoids and artificial tissues.

Chapter 5 Summary and Future Work

5.1 Summary

In this dissertation, we have successfully demonstrated several applications of microcavity lasers with the multimodality imaging system. First, we investigated utilizing ultrasound to modulate the lasing intensity of microdroplet lasers. Deformed by the acoustic radiation force, the droplet emission intensity and direction can be controlled by the input ultrasound signal synchronously. Therefore, by introducing a frequency domain modulation in ultrasound, we can achieve a lock-in-amplifier style signal-to-noise ratio improvement for deep tissue contrast improvement. Furthermore, we demonstrated the capabilities of nanowire lasers working as a novel probe to track the migration trajectories *in vivo* with OCT and FM multimodality imaging system. Since the emission spectra are unique for nanowire lasers with various cavity lengths, nanowires lasers could serve as a distinct label for differentiating different cells. That's a major advantage of microcavity lasers compared to other traditional homogenous contrast agents such as quantum dots or fluorophores. We demonstrated two important application situations for *in vivo* single cell tracking: immune cell migration trajectory analysis and stem cell tracking in stem cell therapies. These two applications proofed the concept of single cell tracking with a multimodality imaging system using microcavity lasers and provided a great platform for other *in vivo* cell studies.

Our work represents a critical milestone to implement microcavity lasers in high signal-to-noise ratio deep tissue contrast agents, acoustic signal sensing, single cell tracking, and therapy evaluation. In the future, these technologies have the potential to support both biological studies

for fundamental science research and clinical situation for therapy safety evaluation to push our understanding towards single cell activity level. Based on these technologies, other diseases such as a tumor could also be investigated thoroughly and clearly.

5.2 Next Steps and Future Work

For ultrasound modulated droplet laser projects:

We have demonstrated the frequency domain modulation of the droplet lasing emission. There are several tasks that need to be finished to push it from a physics phenomenon towards real-world applications.

- Currently, the size of the droplet laser is ~20 μm which is relatively large for a contrast agent purpose. One of the key factors that influence droplet size is the refractive index of the droplet liquids. A higher refractive index resonant cavity can maintain a good Q-factor with a smaller cavity size. One of our solutions is to utilize high refractive index oil (RI=1.78) to replace the corn oil (RI=1.46) and we can achieve lasing droplet cavity with 4-5 μm which can significantly shrink the size of the lasing resonant cavity to performing as contrast agents.
- In this study, the droplet lasers were confined into a microwell or a tube and we used an optical microscope to focus the excitation laser beam onto the droplet laser. For a real-world application, it is not practical to see the droplet lasers in deep tissue. Thus, for the next step, we need to develop a scanning system to move the sample while keeping the excitation laser beam and ultrasound transducer focused on the same spot. By analyzing the temporal recording of the photodetector, we can reconstruct a distribution of the droplet laser where the modulated frequency has a strong intensity. This could be the first step towards a practical ultrasound modulated laser microscopy.

- In addition, to modulate the lasing intensity for a liquid droplet resonant cavity, our study provided a potential method to modulate a solid resonant cavity remotely. In the future, we can explore utilizing ultrasound to tune the output of solid microcavity lasers or exploiting microcavity lasers to sense the ultrasound signal. More research and experiments are needed to be done to further validate this idea.

For in vivo single cell tracking with multimodality imaging projects:

In my Ph.D. study, we have finished two important steps in *in vivo* single cell tracking with nanowire lasers and a multimodality imaging system. First, we proofed the concept of nanowire lasers as multi-modal contrast agents to provide additional OCT, FM contrast to indicate the spatial locations of the tracked cells in 2D/3D. Meanwhile, the various cavity structures of the nanowires could provide different lasing emission spectra serving as a unique "identifier" to differentiate each individual cells. Second, we tracked 10+ stem cells in a damaged subretinal stem therapy situation longitudinally for a longer period. The biocompatibility of the nanowires and the spectral resolution have been improved to support stem cell-related researches. For the next step, there are still several perspectives of this topic to explore and improve:

- The nanowires can be replaced by other novel microcavity lasers, for example, microdisk whispering gallery mode (WGM) lasers [7]. Compared to randomly distributed CdS nanowire lasers, microdisk WGM lasers could have a smaller size (~ 500 nm diameter), non-toxic inorganic material (e.g. GaN), richer spectral information, and better control of the emission wavelength due to the microfabrication process. All these benefits make microdisk WGM a good replacement nanowire in *in vivo* single cell tracking projects. However, one major problem of microdisk WGM laser is the fabrication difficulty and cost. Currently, the microdisk is fabricated in a complicated multiple-step process. It

influences the yield and the average cost of a microdisk to be a couple of dollars, which is not practical for real-world applications.

- Currently, the CdS nanowires were pumped with a 479 nm laser which is determined by the absorption of CdS. This visible wavelength generates more concerns on the safety of pump laser energy density used and limit the cell tracking depth. Therefore, in the future, we can plan to change the material of microcavity lasers from CdS to smaller bandgap material like GaAs and InGaP to use near infrared laser beam to pump the microcavity laser with less scattering loss and damages towards the surrounding tissues.
- The toxicity of heavy metal ions is also a big concern on the safety of cell tracking technology with nanowire lasers. There are several ways we can try to reduce the influence on the toxicity from the nanowires. First, we can design some packaging layers like the biocompatible coating mentioned in the Chapter 4. That will help prevent nanowire lasers to dissolve into the tissue solution. Second, non-toxic material like GaN and AlGaP could be potential choices for replacement of the materials for microcavity lasers to avoid introducing heavy metal ions. On the other hand, the biological toxicity of microcavity lasers for cells and tissues can be conducted by single cell sequencing, cell survival analysis and histology analysis.
- From the system point of view, we can add another imaging modality: photoacoustic microscopy (PA) into our system. The major advantage of photoacoustic microscopy is that it can provide functional information based on absorption coefficient differences. For example, with an excitation laser at 532 nm, we can visualize the vasculature change in the retina to evaluate the pathological changes interacted with stem cell therapy. Adding an additional PA modality into our system is not quite complicated. Briefly, another laser

needs to be coaxially aligned with the OCT and FM laser beams. And an ultrasound needs to be placed at the sample to collect the acoustic signal for imaging reconstruction.

- Besides applying our single cell tracking technologies in ophthalmology, this technology could also be applied in the study of other diseases with some additional setup. For example, we are currently working on a project utilizing a multimodality imaging system to study the activities of circular tumor cells with a skin dorsal chamber to avoid the influence of scattering. The dorsal skin chamber is a glass window that replaces part of the animal skin by surgery. It can help our optical multimodality imaging system directly image the tumor beneath the window and tracked the cell activities with designed contrast agents. This can be a great complementary study for the application field of our technology.

Bibliography

1. Azadgoli, B. and R.Y. Baker, *Laser applications in surgery.* Annals of translational medicine, 2016. **4**(23).
2. Bagger, C. and F.O. Olsen, *Review of laser hybrid welding.* Journal of laser applications, 2005. **17**(1): p. 2-14.
3. Daido, H., M. Nishiuchi, and A.S. Pirozhkov, *Review of laser-driven ion sources and their applications.* Reports on progress in physics, 2012. **75**(5): p. 056401.
4. Wu, X., et al., *Optofluidic laser for dual-mode sensitive biomolecular detection with a large dynamic range.* Nature communications, 2014. **5**(1): p. 1-7.
5. Schubert, M., et al., *Monitoring contractility in single cardiomyocytes and whole hearts with bio-integrated microlasers.* bioRxiv, 2019: p. 605444.
6. Zhao, J., et al., *Full-color laser displays based on organic printed microlaser arrays.* Nature communications, 2019. **10**(1): p. 1-7.
7. Tang, S.-J., et al., *Laser particles with omnidirectional emission for cell tracking.* Light: Science & Applications, 2021. **10**(1): p. 1-11.
8. Lv, Z., et al., *Intracellular near-infrared microlaser probes based on organic microsphere–SiO2 core–shell structures for cell tagging and tracking.* ACS applied materials & interfaces, 2018. **10**(39): p. 32981-32987.
9. Wu, X., et al., *Optofluidic laser for dual-mode sensitive biomolecular detection with a large dynamic range.* Nat. Commun, 2014. **5**: p. 1-7.
10. Wu, X., et al., *Nanowire lasers as intracellular probes.* Nanoscale, 2018. **10**(20): p. 9729-9735.
11. Humar, M. and S.H. Yun, *Intracellular microlasers.* Nat. Photonics, 2015. **9**(9): p. 572-576.
12. Schubert, M., et al., *Lasing within live cells containing intracellular optical microresonators for barcode-type cell tagging and tracking.* Nano Lett., 2015. **15**(8): p. 5647-52.
13. Chen, Y.C., et al., *Laser-emission imaging of nuclear biomarkers for high-contrast cancer screening and immunodiagnosis.* Nat Biomed Eng, 2017. **1**: p. 724-735.
14. Andersson-Engels, S., et al., *In vivo fluorescence imaging for tissue diagnostics.* Phys. Med. Biol., 1997. **42**: p. 815-824.
15. Ntziachristos, V., C. Bremer, and R. Weissleder, *Fluorescence imaging with near-infrared light: new technological advances that enable in vivo molecular imaging.* Eur. Radiol., 2003. **13**: p. 195-208.
16. Udenfriend, S., *Fluorescence assay in biology and medicine*. Vol. 2. 2014: Academic Press.
17. Grimm, J.B., et al., *A general method to fine-tune fluorophores for live-cell and in vivo imaging.* Nat Methods, 2017. **14**(10): p. 987-994.

18. Leblond, F., et al., *Pre-clinical whole-body fluorescence imaging: Review of instruments, methods and applications.* Journal of photochemistry and photobiology B: Biology, 2010. **98**(1): p. 77-94.
19. Lin, C., et al., *Submicrometre geometrically encoded fluorescent barcodes self-assembled from DNA.* Nat. Chem., 2012. **4**(10): p. 832.
20. Ghaderi, S., B. Ramesh, and A.M. Seifalian, *Fluorescence nanoparticles "quantum dots" as drug delivery system and their toxicity: a review.* Journal of drug targeting, 2011. **19**(7): p. 475-486.
21. Tavares, A.J., et al., *Quantum dots as contrast agents for in vivo tumor imaging: progress and issues.* Analytical and bioanalytical chemistry, 2011. **399**(7): p. 2331-2342.
22. Park, J., et al., *CuInSe/ZnS core/shell NIR quantum dots for biomedical imaging.* Small, 2011. **7**(22): p. 3148-3152.
23. Gao, X., et al., *In vivo cancer targeting and imaging with semiconductor quantum dots.* Nature biotechnology, 2004. **22**(8): p. 969-976.
24. Aswathy, R.G., et al., *Near-infrared quantum dots for deep tissue imaging.* Analytical and bioanalytical chemistry, 2010. **397**(4): p. 1417-1435.
25. Cang, H., et al., *Gold nanocages as contrast agents for spectroscopic optical coherence tomography.* Optics letters, 2005. **30**(22): p. 3048-3050.
26. Troutman, T.S., J.K. Barton, and M. Romanowski, *Optical coherence tomography with plasmon resonant nanorods of gold.* Opt. Lett., 2007. **32**(11): p. 1438-1440.
27. Nguyen, V.P., et al., *Chain-like gold nanoparticle clusters for multimodal photoacoustic microscopy and optical coherence tomography enhanced molecular imaging.* Nat Commun, 2021. **12**(1): p. 34.
28. Si, P., et al., *Gold nanobipyramids as second near infrared optical coherence tomography contrast agents for in vivo multiplexing studies.* Nano letters, 2019. **20**(1): p. 101-108.
29. Jaffer, F.A., P. Libby, and R. Weissleder, *Optical and multimodality molecular imaging: insights into atherosclerosis.* Arteriosclerosis, thrombosis, and vascular biology, 2009. **29**(7): p. 1017-1024.
30. Vandenberghe, S. and P.K. Marsden, *PET-MRI: a review of challenges and solutions in the development of integrated multimodality imaging.* Physics in Medicine & Biology, 2015. **60**(4): p. R115.
31. Li, X., et al., *Multimodality imaging in nanomedicine and nanotheranostics.* Cancer biology & medicine, 2016. **13**(3): p. 339.
32. Vansteenkiste, J.F., et al., *FDG-PET scan in potentially operable non-small cell lung cancer: do anatometabolic PET-CT fusion images improve the localisation of regional lymph node metastases?* European journal of nuclear medicine, 1998. **25**(11): p. 1495-1501.
33. Luker, G.D. and K.E. Luker, *Optical imaging: current applications and future directions.* Journal of Nuclear Medicine, 2008. **49**(1): p. 1-4.
34. Taruttis, A. and V. Ntziachristos, *Translational optical imaging.* American Journal of Roentgenology, 2012. **199**(2): p. 263-271.
35. Ruan, G., et al., *Fluorescent–magnetic nanoparticles for imaging and cell manipulation.* Proceedings of the Institution of Mechanical Engineers, Part N: Journal of Nanoengineering and Nanosystems, 2009. **223**(3-4): p. 81-86.

36. Liu, Z., et al., *Long-circulating Er3+-doped Yb2O3 up-conversion nanoparticle as an in vivo X-Ray CT imaging contrast agent.* Biomaterials, 2012. **33**(28): p. 6748-6757.
37. Guo, R., et al., *Ultrasound imaging technologies for breast cancer detection and management: a review.* Ultrasound in medicine & biology, 2018. **44**(1): p. 37-70.
38. Yuan, B., *Ultrasound-modulated fluorescence based on a fluorophore-quencher-labeled microbubble system.* J. Biomed. Opt, 2009. **14**: p. 024043.
39. Cosgrove, D., *Ultrasound contrast agents: an overview.* European journal of radiology, 2006. **60**(3): p. 324-330.
40. Liu, Y., et al., *Ultrasound-modulated fluorescence based on fluorescent microbubbles.* Journal of biomedical optics, 2014. **19**(8): p. 085005.
41. Li, X., et al., *Ultrasound modulated droplet lasers.* ACS Photonics, 2019. **6**(2): p. 531-537.
42. Li, X., et al., *Optical coherence tomography and fluorescence microscopy dual-modality imaging for in vivo single-cell tracking with nanowire lasers.* Biomed. Opt. Express, 2020. **11**(7): p. 3659-3672.
43. Bashkatov, A.N., et al., *Optical properties of human skin, subcutaneous and mucous tissues in the wavelength range from 400 to 2000 nm.* J. Phys. D, 2005. **38**: p. 2543-2555.
44. Clendenon, S.G., et al., *Deep tissue fluorescent imaging in scattering specimens using confocal microscopy.* Microsc Microanal, 2011. **17**: p. 614-617.
45. Kimmey, M.B., et al., *Histologic correlates of gastrointestinal ultrasound images.* Gastroenterology, 1989. **96**: p. 433-441.
46. Tranquart, F., et al., *Clinical use of ultrasound tissue harmonic imaging.* Ultrasound Med. Biol., 1999. **25**: p. 889-894.
47. Errico, C., et al., *Ultrafast ultrasound localization microscopy for deep super-resolution vascular imaging.* Nature, 2015. **527**: p. 499-502.
48. Orsi, F., et al., *High-intensity focused ultrasound ablation: Effective and safe therapy for solid tumors in difficult locations.* Am. J. Roentgenol., 2010. **195**: p. 245-252.
49. Zhou, Y.F., *High intensity focused ultrasound in clinical tumor ablation.* World J. Clin. Oncol., 2011. **2**: p. 8-27.
50. Al-Bataineh, O., J. Jenne, and P. Huber, *Clinical and future applications of high intensity focused ultrasound in cancer.* Canc. Treat. Rev., 2012. **38**: p. 346-353.
51. Marin, A., et al., *Drug delivery in pluronic micelles: Effect of high-frequency ultrasound on drug release from micelles and intracellular uptake.* J. Control. Release, 2002. **84**: p. 39-47.
52. Rwei, A.Y., et al., *Ultrasound-triggered local anaesthesia.* Nat Biomed Eng, 2017. **1**: p. 644-653.
53. Tyler, W.J., et al., *Remote excitation of neuronal circuits using low-intensity, low-frequency ultrasound.* PLOS ONE, 2008. **3**: p. e3511.
54. Kim, H., et al., *Focused ultrasound-mediated non-invasive brain stimulation: Examination of sonication parameters.* Brain Stimul., 2014. **7**: p. 748-756.
55. Szablowski, J.O., et al., *Acoustically targeted chemogenetics for the non-invasive control of neural circuits.* Nat Biomed Eng, 2018. **2**: p. 475-484.
56. Kobayashi, M., et al., *Fluorescence tomography in turbid media based on acousto-optic modulation imaging.* Appl. Phys. Lett, 2006. **89**: p. 181102.
57. Wang, Y.M., et al., *Deep-tissue focal fluorescence imaging with digitally time-reversed ultrasound-encoded light.* Nat. Commun, 2012. **3**: p. 928.

58. Yuan, B., et al., *Microbubble-enhanced ultrasound-modulated fluorescence in a turbid medium.* Appl. Phys. Lett, 2009. **95**: p. 18-21.
59. Fan, X. and S.H. Yun, *The potential of optofluidic biolasers.* Nat. Methods, 2014. **11**: p. 141-147.
60. Yang, S., Y. Wang, and H.D. Sun, *Advances and Prospects for Whispering Gallery Mode Microcavities.* Adv. Opt. Mater, 2015. **3**: p. 1136-1162.
61. Cho, S., et al., *Laser particle stimulated emission microscopy.* Phys. Rev. Lett, 2016. **117**: p. 1-5.
62. Chen, Q., et al., *Highly sensitive fluorescent protein FRET detection using optofluidic lasers.* Lab Chip, 2013. **13**: p. 2679-2681.
63. Chen, Q., et al., *Optofluidic lasers with a single molecular layer of gain.* Lab Chip, 2014. **14**: p. 4590-4595.
64. Polson, R.C. and Z.V. Vardeny, *Cancerous tissue mapping from random lasing emission spectra.* J. Opt., 2010. **12**: p. 024010.
65. Wang, Y., et al., *Random lasing in human tissues embedded with organic dyes for cancer diagnosis.* Sci. Rep, 2017. **7**: p. 1-7.
66. Chen, Y.C., et al., *A robust tissue laser platform for analysis of formalin-fixed paraffin-embedded biopsies.* Lab Chip, 2018. **18**: p. 1057-1065.
67. Humar, M. and S.H. Yun, *Intracellular microlasers.* Nat. Photonics, 2015. **9**: p. 572-576.
68. Schubert, M., et al., *Lasing within Live Cells Containing Intracellular Optical Microresonators for Barcode-Type Cell Tagging and Tracking.* Nano Lett., 2015. **15**: p. 5647-5652.
69. Galanzha, E.I., et al., *Spaser as a biological probe.* Nat. Commun, 2017. **8**: p. 15528.
70. Wu, X., et al., *Nanowire lasers as intracellular probes.* Nanoscale, 2018. **10**: p. 9729-9735.
71. Fingas, M., et al., *The physics and chemistry of emulsions*, in *Workshop on Emulsions*. 1993. p. 770.
72. Wu, J. and G. Du, *Acoustic radiation force on a small compressible sphere in a focused beam.* J. Acoust. Soc. Am, 1990. **87**: p. 997-1003.
73. Møller, P.C.F. and L.B. Oddershede, *Quantification of droplet deformation by electromagnetic trapping.* EPL, 2009. **88**.
74. Mekis, A., et al., *Ray chaos and Q spoiling in lasing droplets.* Phys. Rev. Lett, 1995. **75**: p. 2682-2685.
75. Nockel, J.U. and A.D. Stone, *Chaotic light: a theory of asymmetric resonant cavities*, in *Optical Processes in Microcavities*. 1996. p. 389-426.
76. Nöckel, J.U. and A.D. Stone, *Ray and wave chaos in asymmertic resonant optical cavities.* Nature, 1997. **385**: p. 45.
77. Baryshnikov, Y., et al., *Whispering gallery modes inside asymmetric resonant cavities.* Phys. Rev. Lett, 2004. **93**: p. 1-4.
78. Ge, L., O. Malik, and H.E. Türeci, *Enhancement of laser power-efficiency by control of spatial hole burning interactions.* Nat. Photonics, 2014. **8**: p. 871-875.
79. Gmachl, C., et al., *High-power directional emission from microlasers with chaotic resonators.* Science, 1998. **280**: p. 1556-1564.
80. Gmachl, C., et al., *Kolmogorov–Arnold–Moser transition and laser action on scar modes in semiconductor diode lasers with deformed resonators.* Opt. Lett, 2002. **27**: p. 824-826.

81. Rogers, W.J., C.H. Meyer, and C.M. Kramer, *Technology insight: in vivo cell tracking by use of MRI.* Nature Clinical Practice Cardiovascular Medicine, 2006. **3**(10): p. 554-562.
82. Kircher, M.F., S.S. Gambhir, and J. Grimm, *Noninvasive cell-tracking methods.* Nat. Rev. Clin. Oncol., 2011. **8**(11): p. 677-88.
83. Kim, J.E., S. Kalimuthu, and B.-C. Ahn, *In vivo cell tracking with bioluminescence imaging.* Nuclear Medicine and Molecular Imaging, 2015. **49**(1): p. 3-10.
84. Jeong, H.J., et al., *Macrophage cell tracking PET imaging using mesoporous silica nanoparticles via in vivo bioorthogonal F-18 labeling.* Biomaterials, 2019. **199**: p. 32-39.
85. Horan, P.K., et al., *Fluorescent cell labeling for in vivo and in vitro cell tracking*, in *Methods in cell biology*. 1990, Elsevier. p. 469-490.
86. Krutzik, P.O. and G.P. Nolan, *Fluorescent cell barcoding in flow cytometry allows high-throughput drug screening and signaling profiling.* Nat. Methods, 2006. **3**(5): p. 361-8.
87. Zou, P., et al., *Near-infrared fluorescence labeled anti-TAG-72 monoclonal antibodies for tumor imaging in colorectal cancer xenograft mice.* Molecular pharmaceutics, 2009. **6**(2): p. 428-440.
88. Trounson, A., et al., *Clinical trials for stem cell therapies.* BMC Med., 2011. **9**(1): p. 52.
89. Kang, J., S. Demaria, and S. Formenti, *Current clinical trials testing the combination of immunotherapy with radiotherapy.* J. Immunother. Cancer, 2016. **4**(1): p. 51.
90. Tang, J., et al., *Therapeutic microparticles functionalized with biomimetic cardiac stem cell membranes and secretome.* Nat. Commun., 2017. **8**(1): p. 1-9.
91. Sharma, R., et al., *Clinical-grade stem cell–derived retinal pigment epithelium patch rescues retinal degeneration in rodents and pigs.* Sci. Transl. Med., 2019. **11**(475): p. eaat5580.
92. Wang, L., et al., *Human umbilical cord mesenchymal stem cell therapy for patients with active rheumatoid arthritis: safety and efficacy.* Stem Cells Dev., 2013. **22**(24): p. 3192-3202.
93. Panés, J., et al., *Long-term efficacy and safety of stem cell therapy (Cx601) for complex perianal fistulas in patients with Crohn's disease.* Gastroenterology, 2018. **154**(5): p. 1334-1342. e4.
94. Huang, D., et al., *Optical coherence tomography.* Science, 1991. **254**(5035): p. 1178-81.
95. Puliafito, C.A., et al., *Imaging of macular diseases with optical coherence tomography.* Ophthalmology, 1995. **102**(2): p. 217-229.
96. Drexler, W., et al., *In vivo ultrahigh-resolution optical coherence tomography.* Opt. Lett., 1999. **24**(17): p. 1221-1223.
97. Boppart, S.A., et al., *In vivo cellular optical coherence tomography imaging.* Nat. Med., 1998. **4**(7): p. 861-5.
98. Fernandez, E.J., et al., *Ultrahigh resolution optical coherence tomography and pancorrection for cellular imaging of the living human retina.* Opt. Express, 2008. **16**(15): p. 11083-11094.
99. Rey, S.M., et al., *Three- and four-dimensional visualization of cell migration using optical coherence tomography.* J. Biophotonics, 2009. **2**(6-7): p. 370-9.
100. Lee, T.M., et al., *Engineered microsphere contrast agents for optical coherence tomography.* Opt. Lett., 2003. **28**(17): p. 1546-8.
101. Agrawal, A., et al., *Quantitative evaluation of optical coherence tomography signal enhancement with gold nanoshells.* J. Biomed. Opt., 2006. **11**(4): p. 041121.

102. Ponce de León, Y., et al., *Contrast enhancement of optical coherence tomography images using branched gold nanoparticles.* J. Nanomater., 2012. **2012**: p. 1-9.
103. Gao, A., et al., *Controllable Fabrication of Au Nanocups by Confined-Space Thermal Dewetting for OCT Imaging.* Adv. Mater., 2017. **29**(26).
104. Au, K.M., et al., *Polypyrrole nanoparticles: a potential optical coherence tomography contrast agent for cancer imaging.* Adv. Mater., 2011. **23**(48): p. 5792-5.
105. Kurokawa, K., et al. *Method to investigate temporal dynamics of ganglion and other retinal cells in the living human eye*. in *Ophthalmic Technologies XXVIII*. 2018. International Society for Optics and Photonics.
106. Voura, E.B., et al., *Tracking metastatic tumor cell extravasation with quantum dot nanocrystals and fluorescence emission-scanning microscopy.* Nat. Med., 2004. **10**(9): p. 993-8.
107. Kuo, C.T., et al., *Optically Encoded Semiconducting Polymer Dots with Single-Wavelength Excitation for Barcoding and Tracking of Single Cells.* Anal. Chem., 2017. **89**(11): p. 6232-6238.
108. Li, W., et al., *Superparamagnetic graphene quantum dot as a dual-modality contrast agent for confocal fluorescence microscopy and magnetomotive optical coherence tomography.* J. Biophotonics, 2019. **12**(2): p. e201800219.
109. Fikouras, A.H., et al., *Non-obstructive intracellular nanolasers.* Nat. Commun., 2018. **9**(1): p. 1-7.
110. Lv, Z., et al., *Intracellular near-infrared microlaser probes based on organic microsphere-SiO2 core-shell structures for cell tagging and tracking.* ACS Appl. Mater. Interfaces, 2018. **10**(39): p. 32981-32987.
111. Martino, N., et al., *Wavelength-encoded laser particles for massively multiplexed cell tagging.* Nat. Photonics, 2019. **13**(10): p. 720-727.
112. Tian, C., et al., *Novel photoacoustic microscopy and optical coherence tomography dual-modality chorioretinal imaging in living rabbit eyes.* J. Vis. Exp., 2018(132): p. e57135.
113. Wu, X., et al., *Refractive index sensing based on semiconductor nanowire lasers.* Appl. Phys. Lett., 2017. **111**(3): p. 031112.
114. Ma, C. and Z.L. Wang, *Road map for the controlled synthesis of CdSe nanowires, nanobelts, and nanosaws—a step towards nanomanufacturing.* Adv. Mater., 2005. **17**(21): p. 2635-2639.
115. Weischenfeldt, J. and B. Porse, *Bone marrow-derived macrophages (BMM): isolation and applications.* Cold Spring Harb. Protoc., 2008. **2008**(12): p. pdb. prot5080.
116. Maslov, A.V. and C.Z. Ning, *Modal gain in a semiconductor nanowire laser with anisotropic bandstructure.* IEEE J. Quantum Electron., 2004. **40**(10): p. 1389-1397.
117. Segers, V.F. and R.T. Lee, *Stem-cell therapy for cardiac disease.* Nature, 2008. **451**(7181): p. 937-42.
118. Koch, T.G., L.C. Berg, and D.H. Betts, *Current and future regenerative medicine—principles, concepts, and therapeutic use of stem cell therapy and tissue engineering in equine medicine.* Can. Vet. J., 2009. **50**(2): p. 155.
119. Bailey, A.M., M. Mendicino, and P. Au, *An FDA perspective on preclinical development of cell-based regenerative medicine products.* Nat. Biotechnol., 2014. **32**(8): p. 721-3.
120. Liu, Z., et al., *Looking into the Future: Toward Advanced 3D Biomaterials for Stem-Cell-Based Regenerative Medicine.* Adv. Mater., 2018. **30**(17): p. e1705388.

121. Chichagova, V., et al., *Cellular regeneration strategies for macular degeneration: past, present and future.* Eye 2018. **32**(5): p. 946-971.
122. Li, Q.Y., et al., *Functional assessment of cryopreserved clinical grade hESC-RPE cells as a qualified cell source for stem cell therapy of retinal degenerative diseases.* Exp. Eye Res., 2021. **202**: p. 108305.
123. Ablonczy, Z., et al., *Human retinal pigment epithelium cells as functional models for the RPE in vivo.* Investig. Ophthalmol. Vis. Sci., 2011. **52**(12): p. 8614-8620.
124. Hellinen, L., et al., *Retinal Pigment Epithelial Cell Line with Fast Differentiation and Improved Barrier Properties.* Pharmaceutics, 2019. **11**(8).
125. Zarbin, M., I. Sugino, and E. Townes-Anderson, *Concise Review: Update on Retinal Pigment Epithelium Transplantation for Age-Related Macular Degeneration.* Stem Cells Transl. Med., 2019. **8**(5): p. 466-477.
126. Timmers, A.M., et al., *Subretinal injections in rodent eyes: effects on electrophysiology and histology of rat retina.* Mol. Vis., 2001. **7**: p. 131-137.
127. Trieschmann, M., et al., *Macular pigment in the human retina: histological evaluation of localization and distribution.* Eye, 2008. **22**(1): p. 132-137.
128. Schneider, A.F.L. and C.P.R. Hackenberger, *Fluorescent labelling in living cells.* Curr. Opin. Biotechnol., 2017. **48**: p. 61-68.
129. SoRelle, E.D., et al., *Spatiotemporal Tracking of Brain-Tumor-Associated Myeloid Cells in Vivo through Optical Coherence Tomography with Plasmonic Labeling and Speckle Modulation.* ACS Nano, 2019. **13**(7): p. 7985-7995.
130. Shu, X., L.J. Beckmann, and H.F. Zhang, *Visible-light optical coherence tomography: a review.* J. Biomed. Opt, 2017. **22**(12): p. 121707.
131. Nguyen, V.P., et al., *Contrast agent enhanced multimodal photoacoustic microscopy and optical coherence tomography for imaging of rabbit choroidal and retinal vessels in vivo.* Sci. Rep., 2019. **9**(1): p. 1-17.
132. Kumar, A., et al., *TiO2 nanoparticles as exogenous contrast agent for 1 μm swept source optical coherence tomography: an in vitro study.* Laser Phys., 2018. **28**(3): p. 035601.
133. Dhar, D., M. Mohan, and R. Poddar, *Assessment of Gd2O3 nanoparticles as exogenous imaging contrast agent for swept source optical coherence tomography.* Laser Phys., 2019. **30**(1): p. 015601.
134. Dhada, K.S., D.S. Hernandez, and L.J. Suggs, *In vivo photoacoustic tracking of mesenchymal stem cell viability.* ACS nano, 2019. **13**(7): p. 7791-7799.
135. Humar, M., et al., *Biomaterial microlasers implantable in the cornea, skin, and blood.* Optica, 2017. **4**(9): p. 1080-1085.
136. Martino, N., et al., *Wavelength-encoded laser particles for massively multiplexed cell tagging.* Nat. Photonics, 2019. **13**(10): p. 720-727.
137. Wu, X., et al., *Nanowire lasers as intracellular probes.* Nanoscale, 2018. **10**(20): p. 9729-9735.
138. Roxby, D.N., et al., *Microalgae living sensor for metal ion detection with nanocavity-enhanced photoelectrochemistry.* Biosens. Bioelectron, 2020. **165**: p. 112420.
139. Yuan, Z., et al., *Distinguishing Small Molecules in Microcavity with Molecular Laser Polarization.* ACS Photonics, 2020. **7**(8): p. 1908-1914.
140. Ai, H., et al., *Biocompatibility of layer-by-layer self-assembled nanofilm on silicone rubber for neurons.* J. Neurosci. Methods, 2003. **128**(1-2): p. 1-8.

141. Sinani, V.A., et al., *Collagen coating promotes biocompatibility of semiconductor nanoparticles in stratified LBL films.* Nano Lett., 2003. **3**(9): p. 1177-1182.
142. Zhang, W., et al., *High-resolution, in vivo multimodal photoacoustic microscopy, optical coherence tomography, and fluorescence microscopy imaging of rabbit retinal neovascularization.* Light Sci. Appl., 2018. **7**(1): p. 1-12.
143. Li, Y., et al., *Real-time OCT guidance and multimodal imaging monitoring of subretinal injection induced choroidal neovascularization in rabbit eyes.* Exp. Eye Res., 2019. **186**: p. 107714.